Surface Structure Determination of Group 11 Metals Adsorbed on a Rhenium($10\bar{1}0$) Surface by Low-Energy Electron Diffraction

by

Mag. Lyria Messahel

from Algiers

A Thesis Submitted to the Free University of Berlin
for the Degree of Doctor of Philosophy
in the Faculty of Biology, Chemistry, and Pharmacy

DAAD Deutscher Akademischer Austausch Dienst
German Academic Exchange Service

31st of August 2012

This work has been conducted between February 2008 and August 2012 at the Institut für Physikalische und Theoretische Chemie der Freien Universität Berlin under the supervision of Prof. Dr. Klaus Christmann.

1st reviewer: Prof. Dr. Klaus Christmann
2nd reviewer: Prof. Dr. Thomas Risse

This thesis was defended on: 12th of November, 2012

Acknowledgements

I would like to thank Prof. Dr. Klaus Christmann of the Free University of Berlin for his inspiration, guidance and support. It has been a privilege to be a member of his department. His colleague and successor Prof. Dr. Thomas Risse has likewise been an appreciated source of support.

My grateful thanks are due to the DAAD for its financial support and, in particular, to Mrs Anke Bahrani.

My dear colleagues, Daniel Przyrembel, Inga Spreine, Viktor Scherf, and Christian Pauls helped me to develop a clearer understanding of Surface Science, readily sharing their own knowledge and experience in innumerable conversations. The expert technical support of Karin Schubert and Rudolf Cames also helped advance my understanding.

Jadranka Dokić, Anatole Kenfack, and Lamine Madjet showed the Free University of Berlin to be not only a place of science but also a community of friends and inspiring individuals from many different cultures, but with so much in common.

My respects and thanks go also to Prof. Dr. Saâd Ouichaoui and Prof. Dr. Meziane Brahimi at the University of Science and Technology Houari Boumediène, Algiers, where I completed my Magister's studies.

To my brothers, Racim and Camil, and to every member of my family and to my friends in Algeria, France, the USA, the UAE, and Germany, especially Malika Kersani and Amine Bouzar: your love and support have sustained me every day.

Finally, I dedicate this work to my beloved Mother, Mme Cherifa Messahel, Head of the Boujemâa Temmim School, Algiers, a truly inspirational pedagogue. I owe her everything.

Parce que la science nous balance sa science,
science sans conscience égale science de l'inconscience
Claude M'Barali

Publications during this work

D. Przyrembel, L. Messahel, and K. Christmann, "Interaction of Copper with the Rhenium(10$\bar{1}$0) Surface", J. Phys.: Condens. Matter, 2012, submitted

C. Pauls, V. Scherf, D. Przyrembel, L. Messahel, and K. Christmann, "Über die Wechselwirkung von Ib-Metallen mit einer Rhenium(10$\bar{1}$0)-Oberfläche", Talk. 110^{th} Bunsentagung, Berlin (2011)

Lyria Messahel, Christian Pauls, and Klaus Christmann, "Surface Phases and Structure Determination of Thin Gold Films Grown on a Re(10$\bar{1}$0) surface", Poster. DPG spring meeting, Dresden (2011)

V. Scherf, L. Messahel, C. Pauls, and K. Christmann, "Surface Structures of Thin Silver Films on the Re(10$\bar{1}$0) Surface", Poster. DPG spring meeting, Regensburg (2010)

V. Scherf, L. Messahel, C. Pauls, and K. Christmann, "Surface Structures of Thin Silver Films on the Re(10$\bar{1}$0) Surface", Poster. DPG spring meeting, Dresden (2009)

Viktor Scherf, Christian Pauls, Lyria Messahel und Klaus Christmann, "Phases with Long-Range Order Observed in the Interaction with the Re(10$\bar{1}$0) surface", Talk. DPG spring meeting, Berlin (2008)

Previous publications

L. Messahel, S. Ouichaoui, A. Belhout, M. Fouka and A. Trabelsi, "Electron Screening Factors and Stellar Rates of the $^3He(^3He,2p)^4He$ and $^3He(d,p)^4He$ Fusion Reactions", Frontiers in Nuclear Structure, Astrophysics, and Reactions (FINUSTAR), Crete (2007)

A. Trabelsi, A. Belhout, M. Fouka, L. Messahel, S. Ouichaoui, "R-Matrix Analysis of the $^{10}B(p,\alpha)^7Be$ and $^{11}B(p,\alpha)^8Be$ Reactions at Stellar Energies", FINUSTAR, Kos (2006)

L. Messahel, S. Ouichaoui, "*R*-Matrix Analysis of the $^3He(d,p)^4He$ Reaction at Stellar Energies", Poster. $10^{èmes}$ Journées Scientifiques et Pédagogiques de la Faculté de Physique, University of Science and Technology Houari Boumediène (USTHB), Algiers (2006)

L. Messahel, S. Ouichaoui, "L'effet Casimir", Poster. The National Seminar on Relativity and Quantum Mechanics, USTHB, Algiers (2005)

L. Messahel, S. Ouichaoui, "Du Big-Bang aux Etoiles", Poster. $9^{èmes}$ Journées Scientifiques et Pédagogiques de la Faculté de Physique, USTHB, Algiers (2005)

Curriculum Vitae

For information privacy reasons, my curriculum vitae is not published in the electronic version of my thesis.

Mein Lebenslauf wird aus Gründen des Datenschutzes in der elektronischen Fassung meiner Arbeit nicht veröffentlicht.

Contents

Chapter 1

Introduction

The study of adsorption on metal surfaces is of technological as well as scientific interest. The very fascinating scientific aspect of studying surfaces is that theory and experiment look at the same dimensions, and - provided the system is not too complex - reach the same level of reliability. As the tremendous amount of scientific reports demonstrate, e.g. in [3, 4, 8, 61], there is a long lasting interest in the properties of thin films for a variety of reasons. If we further narrow down the respective publications to single crystalline metallic thin layers, we may focus on problems having a more chemical background and those mainly physicists are interested in. In the first category we may list preferentially the use of thin films in heterogeneous catalysis, in particular with transition metal surfaces, whereby the relationship between structure and chemical activity/selectivity may be reckoned among the most important points of interest. In surface and solid state physics, on the other hand, people are, among other things, seeking insight into the elementary steps of nucleation and growth phenomena; they are interested in the details of epitaxy, *i.e.*, in the interaction between the deposited material and the substrate host lattice. In all of these questions the structure of the growing thin film is a decisive property, and the knowledge of both the geometrical and the electronic structure (note that both properties are intimately correlated with one another) is, in many cases, mandatory for further understanding of the physical and chemical properties of these materials.

Despite the invention of scanning tunneling microscopy (STM) in the mid-eighties by Binnig and Rohrer [6] and the various X-ray absorption techniques, EXAFS and NEXAFS [24], the "classical" tool for accurate and quantitative surface structure determination is undoubtedly still the method of low-energy electron diffraction (LEED). The reason being that LEED not only provides a superior absolute accuracy of $< 0.1\,\text{Å}$,

but provides in addition quantitative information about interlayer spacings that are not easily accessible by surface scanning probe techniques. As with many other surface analytical techniques, also LEED has largely benefited from technological developments that were based on new techniques for data acquisition (TV-LEED developed by the Erlangen group called "AutoLEED" [51], and SPA-LEED with significantly increased spatial resolution [19], not to forget the LEED microscopy (LEEM) developed in the laboratory of E. Bauer [5]).

The surface structure, *i.e.* the spatial distribution of atoms in the surface and near surface layers, usually is the consequence of the minimisation of the surface free energy of the respective solid. Considering clean metal surfaces, the surface free energy for different surface orientations of the same metal may vary considerably. It is also possible that a reconstruction of the surface may lower the surface energy, resulting in a different lattice arrangement than that in the bulk phase. An example are the three low-index surfaces of gold, which all exhibit a surface reconstruction. Adding adsorbate atoms on such surfaces complicates the situation even more. The presence of adsorbates can and will influence the surface free energy and, hence, the ordering of the substrate surface atoms, whereby the ordering can usually be strongly dependent on the kind and number of adsorbed atoms.

Concerning the metal systems that we concentrate on in our work, namely the coinage metals and their adsorption on and interaction with the refractory metal rhenium, we first quote some experimental reasoning why investigations with these materials are especially advantageous. Usually, refractory metal surfaces are relatively easy to clean by high-temperature treatment and due to their high cohesive energy represent rigid templates to precipitate foreign metals with lower melting point such as the coinage metals Cu, Ag and Au. Simply by heating can these metals be removed from the refractory metal substrate using thermal desorption. In addition, the respective thermal desorption spectra offer a convenient possibility to directly determine the previously deposited amount of adsorbate.

The basic purpose of this thesis is the determination of the structure of different surface phases with long-range order that are formed on a rhenium single-crystal surface by vacuum-deposited noble metals Cu, Ag, and Au. The emphasis of this thesis will be on the theoretical field, as certain ideas for possible surface structures will be verified by means of quantitative LEED calculations. The experimental LEED-I,V curves, *i.e.* the characteristic dependence of the scattered beam intensity I on the electron accelerating voltage V, which have been measured in our group at the Free University of Berlin, con-

tain the complete information about the surface structure. They must be reproduced as accurately as possible by the "theoretical" I,V curves obtained in the electron scattering calculations that are performed using tentative atom positions. The comparison between experiment and theory is usually quantified by the so-called Pendry R-factor (reliability factor) [36], whose exact evaluation requires a mathematical analysis of the I,V curves in terms of energy positions of maxima and minima as well as their shape and intensity in a comparison with the experimental I,V data.

The present thesis is organised as follows: In the beginning, some basic remarks about metal-on-metal epitaxy will be presented in Chapter 2, along with some information about some important physical-chemical properties of the metals of interest (Re, Cu, Ag, and Au). Chapter 3 is dedicated to the description of the experimental techniques, LEED, medium-energy electron diffraction (MEED), and temperature-programmed desorption (TPD), that were used to gather the required information about existing surface phases and their structural symmetry and surface homogeneity, but also about surface concentrations (coverages Θ) and atomic binding energies to the surface and their Θ-dependencies. Concerning the LEED computational part, we have dedicated Chapter 4 to some descriptive aspects of LEED kinematic theory, and focused on the Tensor-LEED approximation developed in the Erlangen Tensor LEED package, which was used for all calculations, including some remarks on how the Pendry R-factor is defined. Chapter 5 is subdivided into four parts. The first part summarises the results found for the clean Re($10\bar{1}0$) surface. The following three sections present the LEED-results obtained for each system in the order Cu/Re, Ag/Re, and Au/Re, based on the order of occurrence in the periodic table of elements. Finally, the results will be summarised and discussed aiming at some general conclusions and possible future perspectives.

Chapter 2

Epitaxy of Metals on Metals

2.1 Epitaxy

One of the central points of the present thesis concerns the structure of thin metallic films grown epitaxially on a substrate of a refractory metal, and it is deemed useful to expand somewhat on the term “epitaxy” and the various growth modes of thin films that can lead to well-oriented single crystalline surface films.

The deposition of crystalline over-layers on a crystalline substrate is referred to as “epitaxy”[1] in case where the deposited substance adopts the substrate’s shape. Epitaxial growth is one of the most important techniques to fabricate various electronic and optical devices. Modern devices require very sophisticated structures, which consist in thin layers with various compositions. Quality, performance and lifetime of these devices are determined by the purity, structural perfection and homogeneity of the epitaxial layers. Recently, these have also been used for fabrication of semiconductor quantum structures, for example quantum dots, in order to produce highly perfect structures with high density. Epitaxial crystal growth resulting in layer perfection, surface flatness and interface abruptness depends on a number of factors like: the epitaxial layer growth method, the interfacial energy between substrate and epitaxial film, as well as on various growth parameters – temperature and deposition rate in particular, but also on structural properties such as substrate and layer misfit, or substrate misorientation (defect concentration). We distinguish two major types of epitaxy:

- homoepitaxy, performed with only one material, where a crystalline film is grown

[1] The term epitaxy comes from the Greek roots é epi ($\grave{\varepsilon}\pi\grave{\imath}$), meaning "above", and taxis ($\tau\grave{\alpha}\xi\iota\varsigma$), meaning "in ordered manner".

on a substrate of the same material. This technology is used to grow a film with higher purity than the substrate and to fabricate layers having different doping levels.

- heteroepitaxy, performed with materials that are different from each other. In heteroepitaxy, a crystalline film grows on a crystalline substrate of different chemical kind.

Epitaxial Growth Modes

The occurrence and extent of epitaxial growth depend on various parameters, the most important one being the misfit between the host substrate and the overlayer of the guest material, given by the quantity f [in %] that relates the atomic radii r as:

$$f = \frac{r_{host} - r_{guest}}{r_{host}} \times 100$$

The growth mode characterises the nucleation and growth process. There is a direct correspondence between the growth mode and the film morphology, which are responsible for structural properties such as perfection, flatness and interface abruptness of the layers. Essential is here the kinetics of the transport and diffusion processes at and to the surface. Different atomistic processes may occur on the surface during film growth: deposition, diffusion on terraces, nucleation on islands, nucleation on second-layer islands, diffusion to a lower terrace, attachment to an island, diffusion along a step edge, detachment from an island, diffusion of dimers or oligomers. Experimentally, the distinction between three classical growth modes[2] is well known: Frank-van der Merwe (FM), Volmer-Weber (VW) and Stranski-Krastanov (SK), see Figure 2.1. The quantity which determines the growth mode in the thermodynamic limit may be written in simplified form as:

$$\triangle = \sigma_f + \sigma_i - \sigma_s$$

where σ_f and σ_s are the specific free energies of film and substrate, respectively, and σ_i the specific free interfacial energy [3].

[2] In addition to these three well-known epitaxial growth modes there are four distinct growth modes: step flow mode, columnar growth, step bunching, and screw-island growth (see Crystal Growth Technology, by H. J. Scheel and T. Fukuda, 2003).

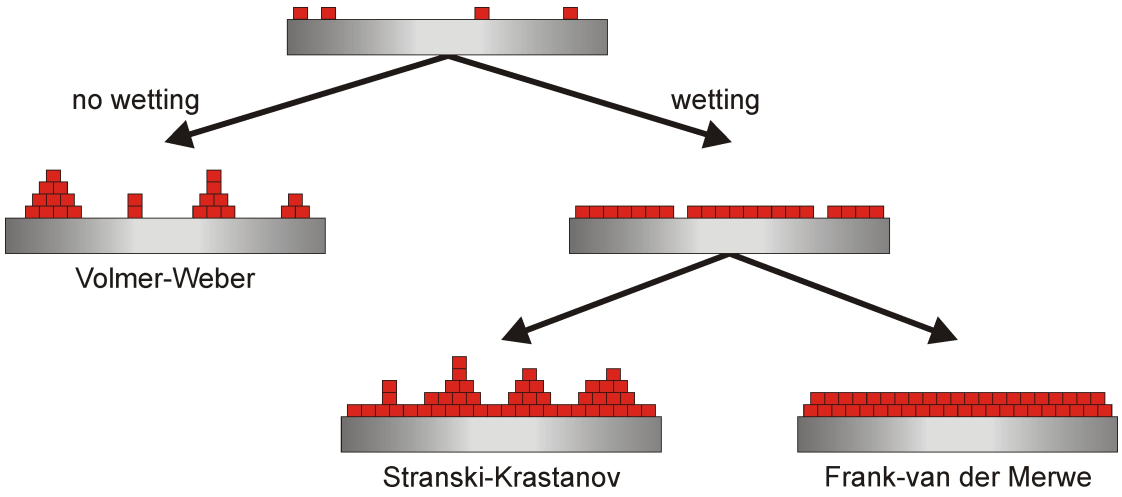

Figure 2.1: Different film growth modes.

Volmer-Weber (VW) Growth Mode

A VW growth mode is characterised by three-dimensional nucleation and growth, when $\triangle > 0$ (Metal growth on oxides usually occurs in this fashion). It is characterised by a large number of surface nuclei in a first phase and by their spreading in a second phase. Growth of these clusters, along with coarsening, will cause rough multilayer films to grow on the substrate surface.

Frank-van der Merwe (FM) Growth Mode

In case of FM or layer-by-layer growth, a new layer is nucleated only after completion of the layer below, for each layer l, $\triangle_l \leqslant 0$, this growth occurs over many layers in ideal case. However crystals are not perfect and contain defects like dislocations that can act as a "sink" for the growing species. Normally there are permanent step sources like screw dislocations or other defects, so FM growth mode works continuously and it can spread growth steps over macroscopic distances.

Stranski-Krastanov (SK) Growth Mode

SK mode is considered as intermediate between the FM and VW growth modes, also known as "layer-plus-island growth", it requires that $\triangle \leqslant 0$ for at least the first layer, and it is caused by significant lattice misfit between film and substrate.

A lattice mismatch between the substrate and the film can cause a build-in strain as a consequence of the increasing elastic energy with increasing layer thickness. the SK mode follows a two step process: initially, complete films of adsorbates, up to several monolayers thick, grow in a layer-by-layer fashion on a crystal substrate. Beyond a critical layer thickness, which depends on strain and the chemical potential of the deposited film, growth continues through the nucleation and coalescence of adsorbate "islands".

2.2 Systems

2.2.1 Rhenium Substrate

Rhenium, $_{75}$Re: [Xe] $4f^{14}$ $5d^5$ $6s^2$, is the third-row transition metal in group 7 of the periodic table and belongs to the extended group of refractory metals[3]. Rhenium is a silvery-white gleaming metal, hard as well as stable in air. With an abundance of only $4 \times 10^{-4}\, ppm$ in earth's crust and $1 \times 10^{-6}\, ppm$ in ocean's water, it is one of the rarest elements.

Due to its high thermal and mechanical stability and the fact that it can be cleaned relatively easily, Re as a substrate presents many interesting advantages. Re is inert to the coinage metals (gold, silver, copper), while it can form alloys, *e.g.*, with palladium and various other transition metals.

Rhenium was discovered in 1925, in Berlin, by German chemists Ida Tacke and Walter Noddack while investigating Columbite (Fe, Mn)$[NbO_3]_2$ and Tantalite (Fe, Mn) $[TaO_3]_2$ minerals by means of X-ray spectroscopy[4]. It was the last naturally stable element to be discovered[5].

The free element has the third-highest melting point of any element ($3180°C$), exceeded only by tungsten and carbon. Chemically, rhenium resembles manganese and is obtained as a by-product of molybdenum[6] and copper refinement [20].

[3]The elements rhenium, osmium, rhodium and iridium belong to the refractory metals additionally to the classical refractory metals of the 4^{th}, 5^{th} and 6^{th} groups in the periodic system.

[4]The name "Rhenium" originates from Latin word "Rhenus", and refers to the couple's native region "Rheinland".

[5]Francium was the last naturally occurring element identified, however it is unstable.

[6]Molybdenum ores like MoS_2 are relatively rich of rhenium.

The Rhenium$(10\bar{1}0)$ Surface

Rhenium crystallises in one of the closest arrangements of spheres, *i.e.,* in the hexagonal close-packed (hcp) lattice, in which each second layer repeats itself (ABAB), as illustrated in Figure 2.2. The dimensions of the volume unit cell are $a_1 = a_2 = a_3 = 2.761\,\text{Å}$ with $\gamma = 120°$ and perpendicular to $c = 4.456\text{Å}$. The unit cell volume is $29.428 \times 10^{-30}\,m^3$, therefore the rhenium atomic radius is $1.375\,\text{Å}$.

Among the various low-index hcp surface orientations, one of particular interest is the $(10\bar{1}0)$, loosely analogous to the fcc (110) surface. The structure of this surface is rather open, featuring parallel $[1\bar{2}10]$ rows of surface atoms separated by shallow trenches, leading to a rich environment for adsorption.

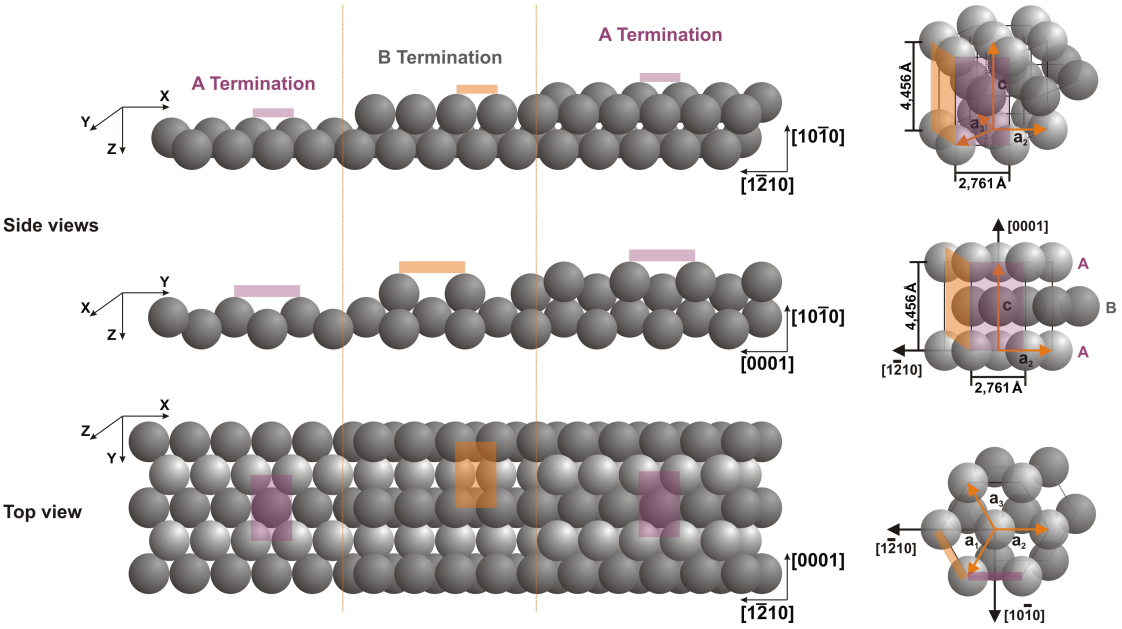

Figure 2.2: The rhenium crystal and the $(10\bar{1}0)$ surface.

That is to say that a wider variety of different adsorption geometries are plausible on this rather "open" surface than on other more "closed" facets. The hcp $(10\bar{1}0)$ surface[7] can exist in two crystallographic terminations "A" and "B", which differ in surface free energy: The coordination number of the surface atoms is 8 for the favoured "A"-termination, but only 6 for the "B"-termination, see section 5.1. Such a stacking

[7]The substrate surface is marked by the disappearance of the periodicity normal to the surface (in the z direction [62].

sequence also tends, for energetic reasons, to favour homoepitaxial growth via bilayers in the hcp lattice.

Concerning surface coverages, we define this quantity (as commonly done) as the ratio between the number of the deposited atoms and the number of topmost Re substrate atoms. With the above-mentioned dimensions of the surface unit mesh of the Re($10\bar{1}0$) surface being $12.303\,\text{Å}^2$ we then arrive at a number of $8.125 \times 10^{18}\, Re\,atoms/m^2$ for this quantity. Accordingly, deposition of the respective number of atoms leads to a coverage $\Theta = 1\,ML$ (one monolayer).

2.2.2 Copper

Copper[8],$_{29}$Cu, with the electronic configuration: [Ar] $3d^{10}\ 4s^1$, is a ductile metal with very high thermal and electrical conductivity. Pure copper is soft and malleable. It is used as a conductor of heat and electricity, a building material, and a constituent of various metal alloys. The low hardness of copper partly explains its high electrical and thus also high thermal conductivity, which are the second highest among pure metals at room temperature. This is because the resistivity to electron transport in metals at room temperature mostly originates from scattering of electrons on thermal vibrations of the lattice, which are relatively weak for a soft metal. Pure copper is orange-red and acquires a reddish tarnish when exposed to air [20]. It has an abundance of $68\,ppm$ in earth's crust and of $3 \times 10^{-3}\,ppm$ in ocean's water. Copper crystallises in a face-centred cubic arrangement like all group 11 metals. The atomic radius of copper is $r = 1.278\,\text{Å}$, and the Cu lattice parameter is $a = 3.615\,\text{Å}$.

2.2.3 Silver

Silver[9], $_{47}$Ag, with electronic configuration: [Kr] $4d^{10}\ 5s^1$ is a very ductile, malleable metal (slightly harder than gold). Though having the highest electrical conductivity of all metals ($6.289 \times 10^7\,\Omega\text{m}^{-1}$), copper remains the metal widely used for electrical purposes because of its lower cost [20]. Silver also crystallises in the fcc lattice; the atomic radius is $r = 1.445\,\text{Å}$ and the lattice parameter $a = 4.085\,\text{Å}$.

[8]Copper comes from Latin: Cuprum. But in the Roman era, copper was principally mined on Cyprus, hence the origin of the name of the metal as cyprium (metal of Cyprus), later shortened to Cuprum.

[9]The word "silver" appears in Anglo-Saxon in various spellings such as seolfor and siolfor. A similar form is seen throughout the Germanic languages (silbir). The chemical symbol Ag is from Latin for "silver", argentum.

Silver is relatively rare with a proportion of $0.08\,ppm$ in earth's crust. It is commonly used as a monovalent coinage metal, with a brilliant white metallic luster that can take a high degree of polish. Among metals, pure silver has the highest thermal conductivity and one of the highest optical reflectivities.

2.2.4 Gold

Gold, $_{79}$Au: [Xe] $5d^{10}\ 6s^1$, is the most malleable and ductile of all metals; a single gram can be beaten into a sheet of $1\,m^2$, thin enough to become translucent. The transmitted light appears greenish blue, because gold strongly reflects yellow and red. Such semi-transparent sheets also strongly reflect infrared light, making them useful as infrared (radiant heat) shields in visors of heat-resistant suits, and in sun-visors for spacesuits. Gold is a good conductor of heat and electricity. Chemically, it is unaffected by air, moisture and most corrosive reagents, and is therefore well suited for use in coins and jewelry and as a protective coating on other, more reactive, metals. However, it is not chemically inert. In addition, gold is very dense, a cubic meter weighing $19.300\,kg$. By comparison, the density of the densest element, osmium, is $22.610\,kg/m^3$. Like Cu and Ag, gold crystallises in the fcc lattice, the Au atomic radius being quite similar to that of Ag, namely $r = 1.442\,\text{Å}$, and the lattice parameter $a = 4.078\,\text{Å}$ [20].

Unlike Cu and Ag, even the low-index Au surfaces tend to reconstruct in the clean state. In this way, the Au(100) surface exhibits a complicated LEED pattern that can be explained by a (5×20) structure where a hexagonal overlayer is built up on the (1×1) fcc bulk phase [21]. The (110) surface reconstruct via the missing-row mechanism forming a (1×2) periodicity, and even the (111) surface shows a (complicated) reconstruction to a $(23\times\sqrt{3})$ phase.

Chapter 3

Experimental Techniques

In this chapter we will give a brief description of the experimental setup with which all measurements were carried out, followed by a short description of the experimental techniques of interest: LEED, MEED, and TPD.

3.1 Experimental Setup

All experiments were carried out in a μ-metal coated stainless steel UHV machine, schematically illustrated in Figure 3.1, equipped with a water-cooled EFM3 evaporator (Omicron) for controlled deposition of Cu, Ag, and Au, a four-grid reverse-view LEED optics (Omicron SpectaLEED) supplemented by a digital camera (Photonic Science) setup to monitor LEED intensities, a quadrupole mass spectrometer (Balzers Prisma) in line-of-sight geometry for TPD and an Ar^+ ion sputter gun (Leybold, IQ 35) for sample cleaning. The chamber additionally contained a $5\,keV$ electron gun (VSW EG5) in grazing-incidence geometry with respect to the sample and a home-made transparent phosphorous screen to display the direct reflected (0,0) electron beam. The electron incidence and reflection angle was $\backsimeq 88°$ with respect to the surface normal; the azimuthal direction of the MEED electron beam was perpendicular to the troughs of the $(10\bar{1}0)$ surface, *i.e.*, perpendicular to the $[1\bar{2}10]$ direction. In our setup, the MEED intensity could be measured (and recorded by a digital camera device as used for LEED) *in situ*, *i.e.,* while the element in question was deposited. MEED (off the Bragg diffraction conditions) is known to precisely and sensitively monitor the surface roughness and, hence, the type of growth simply by following the surface electron reflectivity: An atomically rough surface reflects electrons less efficiently than a smooth, shiny surface.

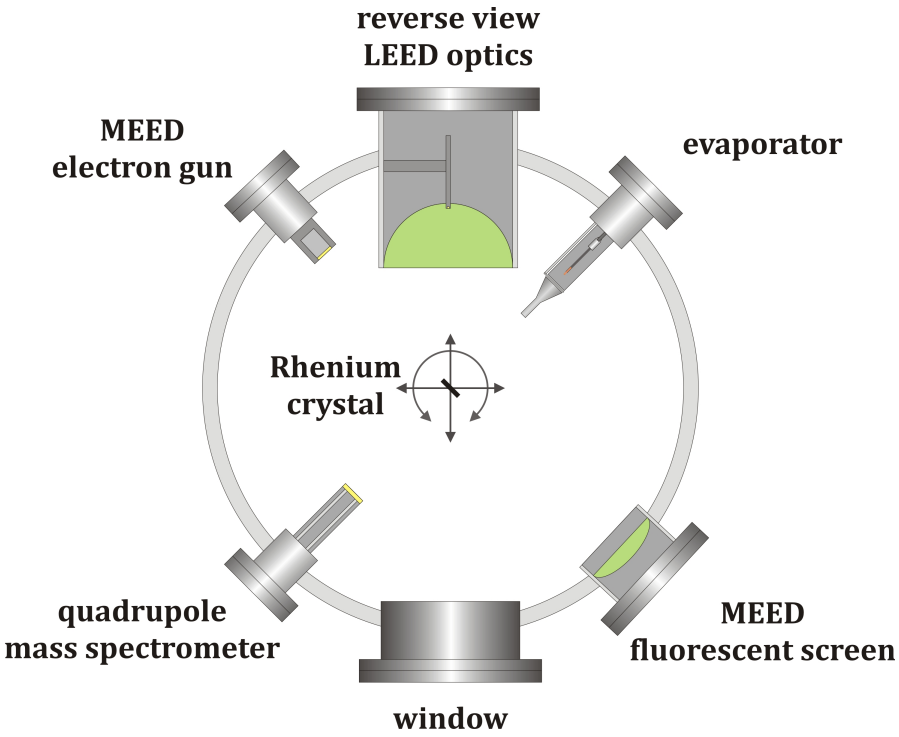

Figure 3.1: Schematic illustration of the experimental setup.

The ultra-pure Re sample (5*N*, MaTeck) was X-ray oriented to the $(10\bar{1}0)$ direction, cut and polished to within a mismatch of 0.2° to obtain a mirror-like finish. It was mounted to a 4*D* manipulator (x,y,z,φ) between two parallel-running $0.5\,mm$ Re wires and could be heated either by means of computer-controlled resistive heating ($T_{max} = 1600\,K$) or by electron bombardment ($T_{max} = 2300\,K$), the temperature being measured with a $W5\%Re/W26\%Re$ thermocouple spot-welded directly to the rim of the Re crystal. The chamber was evacuated by a combined turbomolecular and titanium-sublimation pumping system. After appropriate bake-out an ultimate pressure as low as $\sim 1 \times 10^{-10}\,mbar$ could be achieved; during thin film deposition, the pressure did not rise to more than $6 \times 10^{-10}\,mbar$, for it must be stressed that these pressure conditions are crucial in order to avoid spurious coadsorption of reactive gases, carbon monoxide or water vapour in particular. Note that even traces of these gases can drastically affect the morphology of the deposited metal films and their growth properties, as has been shown recently by Pauls [33] for Au on $Re(10\bar{1}0)$.

High-purity research-grade gases (argon, oxygen) were taken from “Minican” gas cylinders and admitted to the chamber via bakeable leak valves (Varian). Cleaning of

our Re sample was either achieved by several gentle O_2 oxidation/annealing cycles with final flashing to $1800\,K$ or prior to this by controlled gentle Ar ion sputtering, followed by short heating to $1800\,K$ to restore the appropriate surface crystallography. During the experiments, the surface cleanliness and crystallographic order was routinely controlled by AES (Auger Electron Spectroscopy) and LEED.

The EFM3 evaporator mentioned above allowed adjustments of very reproducible deposition rates; usually, relatively low rates of a few Cu, Ag, Au monolayers per hour were chosen. Careful positioning of the sample with respect to the evaporator provided very homogeneous films across the sample surface.

The LEED-I,V data were usually taken above room temperature (unless otherwise stated) by means of a computer-controlled video technique. Careful sample mounting allowed a precise normal electron beam incidence that was repeatedly checked by crosschecking the I,V-curves of symmetry-equivalent beams. The measured LEED images were stored and analysed using the photometry software package IRAF[1] distributed by the NOAO[2]. All intensity data were normalised with respect to the electron current of the incident primary beam.

3.2 Low-Energy Electron Diffraction

Low-energy electron diffraction (LEED), in which electrons are elastically scattered off a surface, has been a very successful technique among those for surface crystallography [48]. Due to the oscillatory nature of their wavefunctions, when a beam of electrons impinges on a surface with a periodic two-dimensional structure, a diffraction pattern appears in the same way as when electromagnetic radiation is used[3]. This effect was first observed in 1927 by Davisson and Germer [13]. In the energy range $10-1000\,eV$, the electrons interact strongly with the substrate atoms and lose energy rapidly after penetrating the crystal. Therefore, filtering out all scattered electrons but those with kinetic energies equal to that of the primary beam ("elastic") yields information only on the uppermost surface atomic layers [16].

[1] Image Reduction and Analysis Facility.

[2] National Optical Astronomy Observatory.

[3] The basis for the interference of electrons at crystal surfaces is the de Broglie equation $\lambda_e = \frac{h}{m_e v_e}$, with h being the Planck constant, m_e the electron mass, and v_e the electron speed.

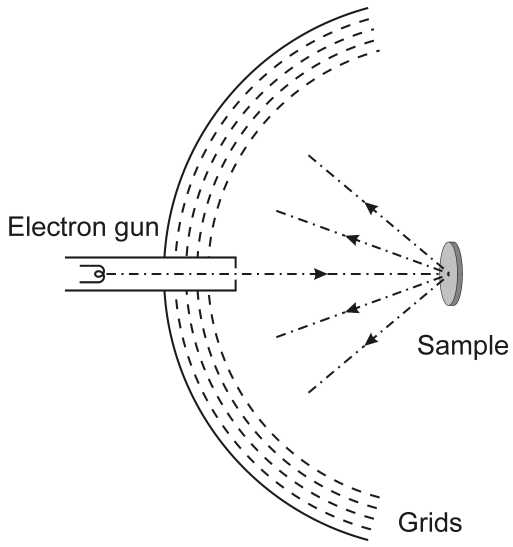

Figure 3.2: Schematic illustration of our LEED display system.
An electron gun (integrated within the LEED optics system) produces a monochromatic beam with an energy up to $1000\,eV$; this beam impinges onto the sample surface, usually at normal incidence. In order to remove all diffracted electrons that have lost energy through inelastic scattering events with the sample atoms, a retarding field with spherical symmetry is created by applying voltages equal to the primary beam energy to the grids situated in front of the screen. The electrons that overcome this retarding field are accelerated toward the fluorescent screen, where they produce bright spots whose intensity is proportional to the number of electrons in the corresponding diffracted beams [16].

A two-dimensional structure, by analogy to a three-dimensional, may be arranged in rows classified by indices (hk).

An arrangement of net points which is periodic in two dimensions may be considered as an ensemble of parallel rows of scatterers with directions $[hk]$ and mutual distances[4] d_{hk}. In this case interference maxima are to be expected in directions given by:

$$n\lambda = d_{hk}(\sin\varphi - \sin\varphi_0)$$

where φ_0 is the incident angle of the impinging electrons, and φ that of the back-scattered electrons.

The LEED pattern is an image of the reciprocal lattice. Intensity maxima appear at those points in reciprocal space that fulfil the two-dimensional Laue conditions [13].

[4]The distance d_{hk} is given by $\frac{1}{d_{hk}^2} = (\frac{h}{a_1})^2 + (\frac{k}{a_2})^2$ in the case of a rectangular unit cell. a_1, a_2 are the unit vectors of the surface net.

These can be illustrated in a graphical way by means of the Ewald construction (see Figure 3.3): the radius of the Ewald sphere represents the wave vector of the incident electron beam, and diffracted beams appear wherever a reciprocal lattice rod intersects the Ewald sphere. The diffracted pattern thus reflects the symmetry of the surface unit mesh, and the separation between the reflexes is inversely proportional to the interatomic distance.

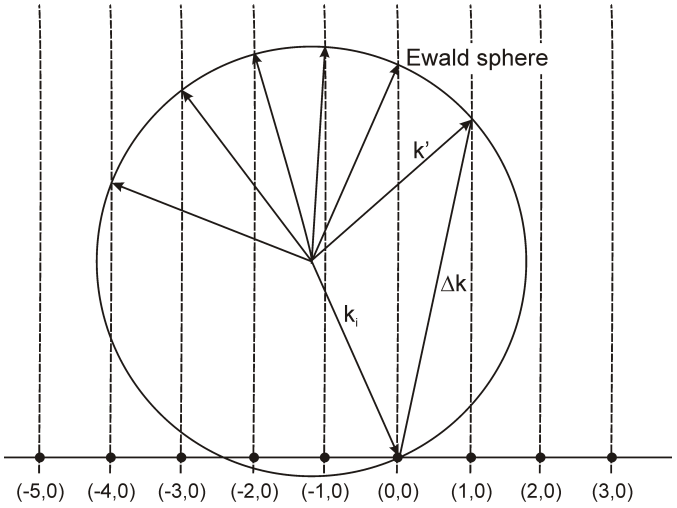

Figure 3.3: The Ewald construction for diffraction at a surface.

Within the kinematic approximation, the elastic interaction of electrons with a surface is treated as the scattering of waves at a two-dimensional net, which means that the finite thickness of the surface region and penetration of the electrons to deeper layers is neglected. This two-dimensional lattice represents the simplest arrangement of points with a periodicity equal to that of the atoms in the surface layer. The unit mesh with the basis vectors a_1, a_2 is the smallest parallelogram from which the lattice may be constructed by translation operations, see Figure 3.4. The reciprocal lattice is defined by the basis vectors a_1^*, a_2^* satisfying the equation:

$$a_i \cdot a_j^* = \delta_{ij} \, (i, j = 1, 2) \tag{3.1}$$

$$\begin{cases} \delta_{ij} = 0 \, , & if \; i \neq j \\ \delta_{ij} = 1 \, , & if \; i = j \end{cases}$$

This is equivalent to the statement that $a_1^* \perp a_2$ and $a_2^* \perp a_1$.

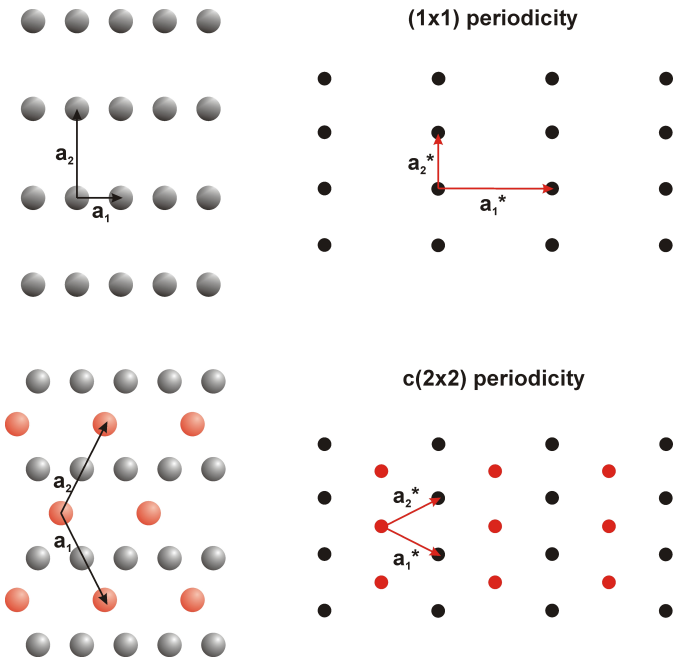

Figure 3.4: Two-dimensional representations of real and reciprocal nets.
(1×1) and c(2×2) net periodicities in the hcp $(10\bar{1}0)$ surface are shown. The real net is described by a_1, a_2 (grey and red spheres), and its reciprocal net by a_1^*, a_2^* (black and red dots). The respective reciprocal nets are magnified by $\times 10^3$. The reciprocal unit vectors are built such that $a_1^* \perp a_2$ and $a_2^* \perp a_1$.

Various processes occur in the surface region of the solid resulting in back-scattering of electrons with energies covering the complete spectrum from zero to the primary energy E_p. Only those which have been elastically scattered (*i.e.* are of energy E_p) carry diffraction information, however, all others must be filtered out since they would produce a background intensity in the diffraction pattern which would tend to obscure the diffraction spots [41].

In order to determine the structure factor, *i.e.* the number and positions of atoms within the unit mesh, spot *intensities* must be analysed. It is experimentally simple to change the incident electron energy in LEED by changing the electron accelerating voltage V, and so to obtain a record of the intensity of a particular spot as a function of voltage V. In this way, for any particular LEED spot, an *intensity-voltage* profile is conveniently obtained, the so-called LEED-I,V spectrum.

3.3 Medium-Energy Electron Diffraction

During the *in-situ* investigation by electron diffraction of systems displaying a layer-by-layer growth mode, oscillations of the reflected intensity are observed. These are periodical with the completion of individual layers. This effect was first reported in 1981 by Harris et al. in RHEED (Reflection high energy electron diffraction) investigations on GaAs homoepitaxy [18]. It is also observed with other experimental techniques, *e.g.,* LEED, MEED and TEAS (thermal energy atom scattering) [17, 14, 46]. According to a strongly simplified kinematic model, the intensity is a measure of the density of scattering centres or simply of the surface roughness [31, 49]. If the experimental setup, *i.e.* beam energy and angle of incidence, is chosen such that for the observed reflex the Bragg condition with respect to the surface normal is never fulfilled, then, only a clean, well-ordered, and therefore relatively smooth crystal surface corresponds to a high reflex intensity. The deposition of an adsorbate on the surface at first increases the number of incoherent scattering centres and thus reduces the coherent scattering intensity. As soon as with growing coverage the adsorbate starts forming again ordered smooth domains, the reflex intensity increases subsequently and reaches a local maximum when a closed adlayer is formed. This allows a direct and reliable determination of the number of deposited layers during film growth, at least in the case when layer-by-layer growth occurs. The three growth modes thereby feature characteristic MEED intensity dependencies on the adsorbate coverage:

- In the case of a strict layer-by-layer growth (Frank-van der Merwe), one obtains periodical maxima every time a layer is closed,

- The Stranski-Krastanov growth mode leads to the appearance of a single maximum, namely on the completion of the first layer and thereafter decreases monotonously,

- For a genuine $3D$ growth (Volmer-Weber), the MEED intensity exhibits only a monotonous decrease.

An illustration of MEED as a probe for surface roughness is shown in Figure 3.5.

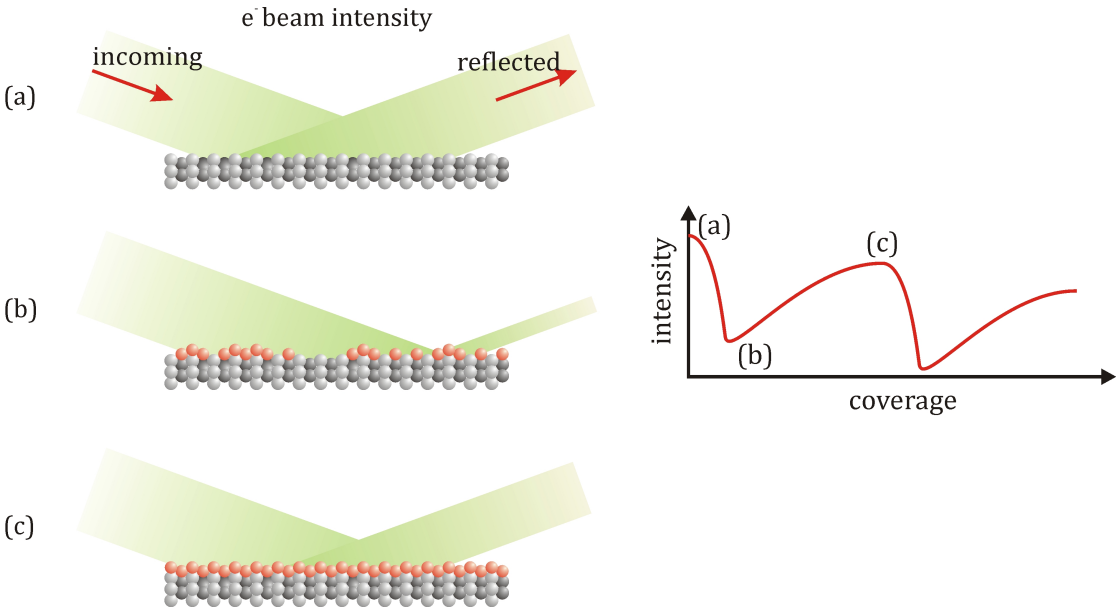

Figure 3.5: Schematic illustration of the MEED process.
In case of layer-by-layer growth, MEED curves are characterised by a succession of maxima and minima of diffracted electron intensity. Maximum (a) reflects the highest intensity reflected by the clean surface. Upon substance deposition, the intensity decreases to reach minimum (b). The intensity increases again as soon as a certain order is recovered on the surface yielding intensity maximum (c).

The formation of closed layers can also be detected in Auger electron spectra but especially for higher coverages MEED measurements are more precise [14]. Another advantage of using MEED rather than AES lies in the fact that due to the lower electron energy employed ($2-5\,keV$), the sample is much less likely to be altered. This makes MEED an excellent method for the determination of ultra-thin film growth modes.

3.4 Temperature-Programmed Desorption

Temperature-programmed desorption (TPD) is an experimental method to investigate kinetics and energetics of adsorbate desorption but also to determine surface coverages. It is usually performed by heating the sample with a constant rate, β, and monitoring the desorbing species by means of a mass-spectrometer until the adsorbate has completely left the surface. In a system with "infinite" pumping speed, the rate of desorption, r_{des}, is directly proportional to the mass-spectrometer's intensity signal. With increasing temperature, T, the rate of desorption also increases until the adsorbate is depleted.

That is why TPD spectra always exhibit a maximum.

In one-component systems with discrete desorption states, the rate of desorption can be described by the Polanyi-Wigner equation:

$$r_{des} = -\frac{d\Theta}{dt} = \nu_n \Theta^n \exp\left(-\frac{E_{des}}{RT}\right), \tag{3.2}$$

where Θ is the coverage at time t, ν is the frequency factor, n the desorption order, R is the gas constant, and E_{des} is the desorption energy. A wider theoretical description of the thermal desorption technique can be found with much more details, *e.g.,* in references [11, 48]. Here, it suffices to say that the position of a TD maximum can be used, according to Equation 3.2, to determine the adsorbate's binding energy to the surface[5], E_{des}, and its dependence on the initial coverage to determine its order of desorption.

The other relevant information that can be gained from a TD spectrum is its peak areas, which are proportional to the amount of material present on the surface prior to the application of the TD program. If the absolute partial pressure of the desorbing species were known the absolute coverage could be determined. However, it is much easier to conclude on the *relative* coverages. These can be converted into absolute coverages, if a given TD spectrum can be calibrated, *e.g.*, by means of a unique surface structure (LEED!) or a MEED intensity. Note that just the knowledge of the absolute coverage of a deposited film confines the number of guesses for certain surface structures and, hence, greatly facilitates a LEED structure analysis as will be demonstrated later in this work.

[5] Strictly only in case of first order desorption.

Chapter 4

LEED Theoretical and Computational Basics

The quantitative analysis of intensity spectra from low-energy electron diffraction is a very powerful technique for the extraction of detailed surface crystallographic information [7]. A lot about the surface structure can be learnt simply by the inspection of the LEED pattern - symmetry and periodicity - without considering the quantitative I,V behaviour of the individual spots. Basically, we observe on the screen the reciprocal lattice of the surface, from which we can construct models for the real lattice. There are, however, several effects complicating this analysis [36]. Surfaces contain lots of imperfections, the electrons do not scatter from a perfect periodic structure but from a "real" surface at finite temperature, with steps, point defects and "dirt" in form of adventitious adsorbates. These imperfections cause an intensity loss and a broadening of the diffraction spots and an increase of the background inbetween the spots. One can turn this problem into an advantage and use the spot profile of the diffraction maxima in order to learn something about the surface imperfections. This technique is called spot profile analysis LEED (SPA-LEED).

4.1 LEED Kinematics

The kinematic theory of scattered intensities is based on the assumption that the incident radiation interacts with matter weakly enough so that only single scattering processes can be considered as a good approximation. This assumption is justified for the scattering of X-rays and fast electrons, but does not hold for that of low-energy electrons with

solids. This theory provides a rather good approximation for the analysis of partially disordered structures on the basis of intensity information at a fixed electron energy. In addition, it represents the background for the more "rigorous" theories.

Based on the plane wave representation of the incident electron beam, ψ_0, the scattered wave at an atom i , at the position r_i has the following amplitude:

$$\psi = \left(\psi_0 \cdot \frac{\exp^{ikr}}{r} \right) \cdot f_i(k_0,k) \exp^{i(k-k_0)\cdot r_i} . \tag{4.1}$$

The first term describes a spherical wave, and f_i is the atomic scattering factor, which for a given kind of atom depends on wave vectors[1] k_0 and k. The last term denotes the phase shift between a wave scattered at r_i and the origin of the coordinate system caused by the path difference. For a two-dimensional periodic lattice, the atomic factors f_i can be replaced by the scattering factor, or structure factor, F, of the unit cell.

The total intensity scattered by a crystal surface is proportional to the square of the amplitude, ψ, obtained from a superposition of the waves originating from the single atoms with the corresponding phase shifts:

$$I(k_0,k) \propto \left| \sum_{i=1}^{N} f_i(k_0,k) \exp^{i(k-k_0)\cdot r_i} \right|^2 . \tag{4.2}$$

4.2 LEED Dynamic Theory

In contrast to the kinematic theory, where the effective scattered wave only depends on the difference $k-k_0$ *(i.e.* on the angle between the incident and the scattered beam), the scattering factor $f(k_0,k)$, due to multiple scattering, explicitly depends on the wave vectors k_0 and k. Each atom does not only "see" the incident wave but also those scattered by its neighbours. Each atom in the unit cell has thus a different cross-section, even for identical atoms. A full dynamical theory aims to determine the effective scattered wave on the basis of the following three major points:

- The muffin-tin approximation (see below).
- Consideration of inelastic processes through the imaginary part of the scattering potential, V_{0i}, consistently with the experimental findings, in that the full widths at half maximum of the single peaks in the I,V curves are very similar.

[1] k_0 and k are defined as $k_0 - k = g = ha_1^* + ka_2^*$, where a_i^* are the reciprocal unit vectors, g is the scattering vector, and h and k are integers.

- Consideration of thermal effects by taking into account the isotropic[2] atomic vibrations.

4.2.1 The Muffin-Tin Approximation

The basis for all theories is the "static potential model", in which it is assumed that the atoms are rigidly located in a lattice (as used for all band structure calculations). Lattice vibrations may be included by making the positions of the nuclei time-dependent. The Hamiltonian describing the problem may be formulated as follows:

$$H_0 = -\frac{\hbar^2}{2m} \triangle + V_p + V_0. \tag{4.3}$$

$V_p = -\sum_n V_n(r - R_n)$, where V_n is the static potential of an atom n with its nucleus positioned at R_n. The term $V_n(r - R_n)$ represents the potential of an ion core in a sea of mobile electrons which should be considered non local and should in principle contain exchange and correlation effects in a selfconsistent manner.

V_0 is called the inner potential and corresponds to the constant part of the potential (the "muffin-tin zero", V_{MTZ}) in Figure 4.1.

The muffin-tin approximation is a shape approximation of the potential field in an atomistic environment[3]. It is commonly employed in quantum mechanical simulations of electronic band structure in solids. The approximation was proposed by John C. Slater [47] and is employed in many modern electronic structure methods[4]. One application is found in the variational theory developed by Korringa (1947) and by Kohn and Rostocker (1954) referred to as the KKR method. This method has been adapted to treat random materials as well, where it is called the KKR coherent potential approximation.

According to the Mattheiss prescription [30], the crystal is built up by placing the spherically averaged potentials of the individual atoms at the lattice positions of the atoms. In order to give definition to the crystal potential, the range of affect of each potential is defined by the muffin-tin radius of the respective atom.

[2]The muffin-tin approximation is only adequate within an isotropic treatment.

[3]The choice of the muffin-tin radius for an atom is largely governed by chemical intuition. There are tabulated values of atomic, Pauling, and ionic radii available. These can be correlated with knowledge of bond lengths in the crystal lattice to determine a working radius of affect for an atom - the muffin-tin radius of its potential.

[4]Among these methods are the augmented plane wave (APW), the linear muffin-tin orbital (LMTO) and various Green's function methods.

In this viewpoint, the atoms are treated as "hard" spheres of potential packed together in a lattice, see Figure 4.1, which is a surprisingly good approximation. It describes the fact that the potential energy for electrons in a crystal is lower than in a vacuum - an effect which leads to refraction at the boundary and to a variation of the electrons' wavelength.

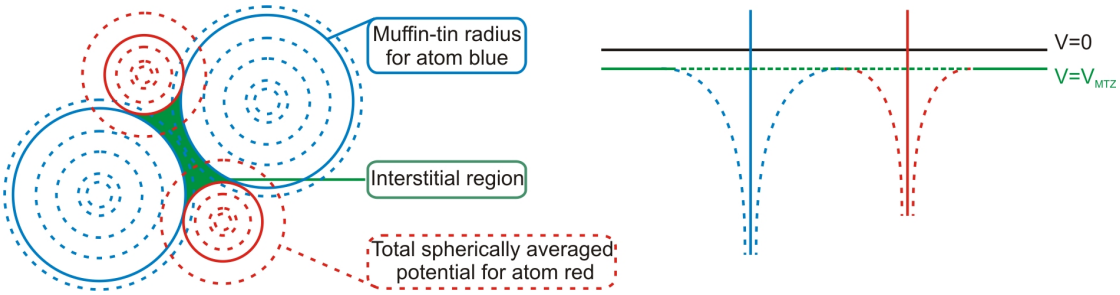

Figure 4.1: Schematic representation of the muffin-tin approximation.
Within spheres around the individual ion cores (which usually touch each other) a spherically symmetric potential is assumed, while in the region left over the potential is taken to be constant.

A direct manifestation of this effect becomes apparent from observed displacements on the energy scale of the "primary" Bragg peaks. V_0 is usually treated as an adjustable parameter. An average value of the net total spherically averaged potential in the interstitial region (taken from the overlap of neighbouring atom potentials) is found and taken to be the defined muffin-tin zero value of the crystal potential. This shifts the energy zero of the entire crystal to the average potential of the interstitial regions. The muffin-tin potential is then:

$$V(r) = \begin{cases} V_T(r) - V_{MTZ} & for \quad r < r_{MT} \\ 0 & for \quad r \geq r_{MT} \end{cases} . \tag{4.4}$$

4.2.2 The Inner Potential

An electron in a crystal can:

- be scattered by the strong potentials inside the surface, either with a scattering angle of $< 90°$ (forward scattering), or back-scattered, *i.e.* the momentum normal to the surface is reversed. LEED depends particularly on the latter process, because experimentally the back-scattered electrons are detected.

- undergo a loss of energy. If the energy-selecting grids are in position such an energy loss is tantamount to absorption of the electron because it will never subsequently have enough energy to make an appearance on the fluorescent screen.

- undergo a uniform lowering of its energy as it enters the potential well of the crystal (the same well is responsible for keeping the conduction electrons in the crystal).

The strength of each of these three processes can be gauged by a matrix element. Electrons are scattered at a rate determined by forward and backward scattering matrix elements T_f and T_b, respectively, due to each of the atoms comprising the crystal. T is a continuous function of scattering angle and the division into T_f and T_b is made for conceptual convenience. T is also a function of the incident energy.

Inelastic scattering events of all sorts are treated together in terms of the lifetime of an electron, τ. An electron with energy E would normally have a temporal variation in its wave function amplitude of $\exp(-iEt)$. By giving the energy an imaginary component of $+iV_{0i}$, the intensity of the wave function can be made to decay away in time as $\exp(+2V_{0i}t)$ and we can equate:

$$V_{0i} = -\frac{1}{2\tau}. \tag{4.5}$$

Attenuation of elastically scattered beams can be simulated by an imaginary component of the energy, *i.e.,* by adding a constant imaginary potential, iV_{0i}, to the Schrödinger equation (4.3 on page 37).

A simple theory of peak formation runs as follows: although the electrons do not penetrate deeply into the crystal, one might suppose, especially at high energies, that they do go sufficiently deep to be sensible of the periodic structure of the crystal in the z-direction. In the case of X-rays, which penetrate much more efficiently, peaks in reflectivities are determined by conditions for Bragg reflection off planes of atoms. If we try to apply Bragg theory to LEED we deduce that peaks in the (0,0) beam are caused by reflection from planes of atoms parallel to the surface. If the spacing between these planes is c, the Bragg condition for a peak is:

$$\frac{2\pi}{\lambda} = integer \times c, \tag{4.6}$$

ensuring that reflections from successive planes are in phase. λ, the wavelength of the electrons, will not be quite the same as it is in free space because of the "inner potential" well inside the crystal: V_0

$$\lambda = 2\pi(2E - V_0)^{-\frac{1}{2}}, \tag{4.7}$$

E, V_0 , and λ are in atomic units. Substituting 4.7 into 4.6 yields:

$$E = \frac{1}{2}\left[c^2(integer)^2 + V_0\right]. \tag{4.8}$$

In the high energy range there is reasonable correlation with Bragg theory but in intermediate and low energy ranges there are more experimental peaks than Bragg theory predicts. Peaks that coincide most closely with the Bragg condition are called "primary" peaks and all others "secondary" peaks, but sometimes the complications are such that even this classification can be ambiguous.

4.2.3 Thermal Vibrational Amplitudes

In addition to its primary use in giving information on the structures of surfaces and adsorbates, LEED may also serve as a probe of the surface vibrational amplitudes. Just as in X-ray diffraction, the intensities of the diffraction spots decay exponentially with the mean-square amplitude of the atomic vibrations:

$$I = I_0 \exp\left(-\sum_i \triangle k_i^2 < v_i^2 >\right). \tag{4.9}$$

In this expression I_0 is the intensity from a rigid lattice of scatterers, $\triangle k$ the momentum transfer of the scattered electron, and $< v_i^2 >$ the mean-square amplitude of vibration of the atom from its equilibrium position.

This equation expresses the fact that only those atoms that are in their equilibrium positions in the ordered structure will contribute to the intensity of the Bragg peaks. The electrons that are scattered from atoms displaced from their equilibrium positions will contribute to the diffuse background intensity. The vibration of the atoms does not change the width of the diffracted beams, only their intensity. Increasing the crystal temperature increases the amount of time the atoms spend away from their equilib-

rium position; thus the intensity of the diffraction beams falls off as the temperature is raised [48].

Isotropic thermal vibrations of the crystal atoms were taken into account by the previous versions of LEED programs [54] through the generation of "temperature-dependent phase shifts" (these being complex numbers), in that the temperature effect was included through the multiplication of each atom's scattering amplitude by a Debye-Waller factor e^{-M}, where:

$$M = \frac{1}{2}\left\langle (\triangle k \cdot \triangle \nu)^2 \right\rangle_T = \frac{1}{6}|\triangle k|^2 \left\langle (\triangle \nu)^2 \right\rangle_T . \tag{4.10}$$

Here $\triangle k$ is the momentum transfer resulting from the diffraction from one beam into another. $\triangle k$ is defined inside the surface, where the muffin-tin constant is added to the outside electron energy. The real part of the complex number $\triangle k$ is taken, since only the real part gives rise to the wave interference on which the Debye-Waller factor is based. In the high-temperature limit ($T \gg \theta_D$, where θ_D is the Debye temperature[5]) we have, in atomic units:

$$\left\langle (\triangle k)^2 \right\rangle_{T\to\infty} \simeq \frac{9T}{m k_B \theta_D^2}, \tag{4.11}$$

where the atomic mass m is expressed in units of the electron mass, $k_B = 3.17 \times 10^{-6}\, hartrees/kelvin$, and the actual and Debye temperatures in Kelvin.

To account for the fact that vibrational amplitudes for surface layers may be different from those of bulk layers, the programs accept as input an enhancement factor (with components parallel and perpendicular to the surface) that is multiplied into $\left\langle (\triangle k)^2_{T\to\infty} \right\rangle$. The programs allow this enhancement factor to depend on the atomic species; thus for layers of the same atomic species, a single enhancement factor is to be used.

For low temperatures ($T \lesssim \Theta_D$) the expression 4.11 is inadequate. In the very-low temperature limit the correct expression is:

$$\left\langle (\triangle k)^2 \right\rangle_{T\to 0} \simeq \frac{9}{m k_B \theta_D} \left(\frac{1}{4} + 1.642 \frac{T^2}{\Theta_D^2} \right). \tag{4.12}$$

In the LEED programs used here, a single functional form is used to represent the temperature dependence of $\left\langle (\triangle \nu)^2 \right\rangle$ for all T: setting $T = 0$ (zero-point motion) in Equation 4.12, one obtains the interpolated thermal displacement as used in TensEr-LEED [7]:

[5] $\Theta_D = \frac{h\nu_D}{k_B}$, with ν_D being the maximum vibrational frequency.

$$\left\langle (\triangle v)^2 \right\rangle_T = \overline{[\langle (\triangle v)^2) \rangle_{T=0}] + [(\triangle v)^2)_{T\to\infty}]}. \tag{4.13}$$

4.2.4 The Concept of Tensor LEED

The recent years have seen a tremendous growth of the complexity of surface structures solved, much of which is due to the experimental and theoretical progress made in low-energy electron diffraction, and, in particular, the introduction of the Tensor LEED approximation for the calculation of LEED intensities [43]. Conventional full dynamic LEED calculations are limited by the fact that the time to compute the electron wave diffracted from a surface scales essentially as N^3 with N the number of independent scattering centres in the unit cell. So, with growing complexity of the surface under consideration, the computational effort to calculate a single LEED spectrum rises rapidly. To make things worse, the number of free parameters in a complex structure optimisation is usually also much larger than for a "simple" surface, requiring many more I,V calculations. For example, in a straightforward grid search, the effort scales exponentially with the number of free parameters.

The Tensor LEED approximation aims to resolve the problem of scaling behaviour with system size. It is based on the idea that, while low-energy electron diffraction from a surface is governed by multiple scattering, a small modification of a given reference surface will only cause a small change in the diffracted electron wave field and may be treated by a perturbational approach. Once the full dynamic scattering from the reference surface is known, the wave functions of structurally similar surfaces are deduced with computing times scaling only linearly with the number of atoms involved. In other words, the strategy is

- to perform a full dynamic LEED calculation once for a *reference surface*, saving those parts of the wave function needed later for the perturbational treatment, and then
- to use that wave function to calculate approximate amplitude changes δA for geometrically, stoichiometrically or vibrationally modified surface structures.

The remaining task is to reliably determine the structural *best fit* within the portion of the parameter space accessible via Tensor LEED. A number of optimisation strategies for LEED have been proposed over the years [23]. So far, the preferred method is that introduced by Kottcke and Heinz [25]. It offers the advantage of being a global approach

to structure optimisation (avoiding the risk of being caught in the local optimum closest to the starting position of the search) but with relatively improved scaling behaviour.

As already mentioned, the Tensor LEED approximation is based on a full dynamic calculation of the LEED wave function for one suitably chosen *reference surface* [36, 56]. Here, some basic formulae suffice to derive the Tensor LEED approximation to a full dynamic calculation. The starting point is the scattering of electrons from a surface described by the muffin-tin approach, *i.e.* by the scattering potential:

$$V = V_0 + \sum_i \upsilon_i, \tag{4.14}$$

with υ_i being the individual atomic potentials forming the surface and V_0 the complex inner potential. Following the original treatment of Rous and Pendry[43], the LEED state diffracted by the surface is written as:

$$\left|\Phi^+(k_{\shortparallel})\right\rangle = G^+ \left|\varepsilon(k_{\shortparallel})\right\rangle, \tag{4.15}$$

where $|\varepsilon(k_{\shortparallel})\rangle$ stands for the incident state in the far past and G^+ denotes the Green function for the full surface potential. $|\varepsilon(k_{\shortparallel})\rangle$ is chosen such that, when acted upon by the free space Green function G_0^+, it generates a plane wave of given energy E with a momentum component $k_{\shortparallel}$ parallel to the surface. The total Green function G^+ can be expressed as a Born series in the crystal potential:

$$G^+ = G_0^+ + G_0^+ V G_0^+ + G_0^+ V G_0^+ V G_0^+ + ..., \tag{4.16}$$

or, using the potential of Equation 4.14 and the definition of the atomic t-matrix, $t_i = v_i + v_i G_0^+ v_i + ...$, as:

$$G^+ = G_0^+ + \sum_i G_0^+ t_i G_0^+ + \sum_i \sum_{j,j\neq i} G_0^+ t_i G_0^+ t_j G_0^+ + ..., \tag{4.17}$$

In principle, Equation 4.17 contains all information needed to solve the LEED problem full dynamically. For convenience, the constant inner potential V_0 is included as an energy offset in the free space Green function G_0^+. Semiclassically speaking, each scattering atom in the unit cell is now represented by its t-matrix t_i, and the path between two scattering events is described by G_0^+. Note that, in Equation 4.17, *successive* scattering events at the *same* atom do not occur. The atomic t-matrix already includes all such terms.

In order to derive the Tensor LEED approximation, a modified surface with atomic t-

matrices $\tilde{t}_i = t_i + \delta t_i$ is considered. The Green function $\tilde{G}^+$ of the new surface becomes:

$$\tilde{G}^+ = G_0^+ + \sum_i G_0^+ (t_i + \delta t_i) G_0^+ + \sum_i \sum_{j,j\neq i} G_0^+ (t_i + \delta t_i) G_0^+ (t_j + \delta t_j) G_0^+ . \qquad (4.18)$$

By carefully reordering all terms of this expression, one can arrange $\tilde{G}^+$as a power series in δt_i, *i.e.:*

$$\tilde{G}^+ = G^+ + \sum_i G_i^{start} \cdot \delta t_i \cdot G_i^{end} + O((\delta t_i)^2), \qquad (4.19)$$

where (using the reciprocity theorem for Green functions [56]):

$$G_i^{end} = G^+ - G_0^+ t_i G_0^+ - \sum_{j,j\neq i} G_0^+ t_i G_0^+ t_j G_0^+ - \ldots \qquad \textit{and}$$

$$G_i^{start} = G_i^{end\dagger *} \qquad (4.20)$$

sum up all scattering paths that *do not* end with (begin with) a scattering process at atom number i, respectively. The Tensor LEED approximation is obtained from Equation 4.19 by keeping only the term linear in δt_i and discarding all higher orders. The quantities $G_i^{end\dagger *}$ and G_i^{end} surrounding δt_i again reflect the fact that, in Equation 4.17, there must not be any *successive* scattering events at the same atom. For the modified structure, this restriction implies that no scattering path may contain the undisplaced t-matrix t_i, and then its change δt_i immediately following one another.

Equation 4.19 offers some convenient computational advantages. The only quantities that depend on the modified surface, namely the changes in the atomic t-matrices $\delta t_i - G^+$ and G_i^{end}, merely depend on the *reference surface*. So, for each particular modified structure it is only necessary to compute δt_i for all required sites i - the remaining terms need to be evaluated for the *reference surface* only. Moreover, changing the properties of different atoms simultaneously enters different terms in the sum in Equation 4.19, making it possible to evaluate each term in that sum independently for each atom, effectively linearising the effort to compute changes in the LEED state for more than one atom at a time.

Having obtained a formal expression for the Tensor LEED approximation, all we need to do is to translate it into the familiar language of LEED calculations. We are

interested in calculating the plane wave amplitudes $\tilde{A}^-_{g'}$ emerging from the modified surface ($\{g'\}$ denotes the set of reciprocal lattice vectors of the distorted surface, which may differ from that of the *reference surface*). They are usually evaluated at some position Z_0 outside the surface, the origin of the calculations, by projecting the LEED state on the wave function $\langle Z_0, k_{||} + g' |$given by:

$$\langle \bar{r} \, | Z_0, k_{||} \rangle = \exp(ik_{||} \cdot r) \cdot \delta(z - Z_0). \tag{4.21}$$

Using Equation 4.15, one obtains:

$$\tilde{A}^-_{g'} = \left\langle Z_0, k_{||} + g' \left| \bar{G}^+ \right| \varepsilon(k_{||}) \right\rangle, \tag{4.22}$$

an expression that can be split into the amplitudes leaving the *reference surface*, $A^-_{g'}$, and a sum of amplitude changes $\delta\tilde{A}^-_{i,g'}$ induced by modifying the scattering properties of individual atoms i:

$$\tilde{A}^-_{g'} = A^-_{g'} + \sum_i \delta\tilde{A}^-_{i,g'} \tag{4.23}$$

with

$$\delta\tilde{A}^-_{i,g'} = \left\langle Z_0, k_{||} + g' \left| G_i^{end\dagger *} \cdot \delta t_i \cdot G_i^{end} \right| \varepsilon(k_{||}) \right\rangle \tag{4.24}$$

by inserting Equation 4.19. Since atomic t-matrices enter a LEED calculation in their angular momentum representation centred at the atomic position r_i, Equation 4.24 can be rewritten as:

$$\delta\tilde{A}^-_{i,g'} = \sum_{l,m,l',m'} T_{i,g',l,m,l',m'} \cdot \langle r_i; l, m \, | \delta t_i | \, r_i; l', m' \rangle,$$

with

$$T_{i,g',l,m,l',m'} = \left\langle Z_0, k_{||} + g' \left| G_i^{end\dagger *} \right| r_i; l, m \right\rangle . \left\langle r_i; l', m' \left| G_i^{end} \right| \varepsilon(k_{||}) \right\rangle. \tag{4.25}$$

$T_{i,g',l,m,l',m'}$ now contains all terms that depend on the *reference surface* and is the quantity referred to as the *tensor*.

The Tensor

In order to obtain the tensor $T_{i,g',l,m,l',m'}$ from a numerical calculation, it is necessary to relate the following quantities to a conventional LEED calculation:

$$\left\langle r_i; l', m' \left| G_i^{end} \right| \varepsilon(k_{\parallel}) \right\rangle \tag{4.26}$$

and

$$\left\langle Z_0, k_{\parallel} + g' \left| G_i^{end\dagger *} \right| r_i; l, m \right\rangle. \tag{4.27}$$

As mentioned before, the operator G_i^{end} contains all scattering paths included in the total Green function G^+ except those that end with a scattering event at atom i. In Equation 4.26, this operator acts upon the incident wave and is then evaluated in angular momentum components centred around atom i. In other words, Equation 4.26 contains nothing else than the components of the *wave field incident upon but not scattered by atom i* of the *reference surface*. Now, as pointed out by Rous and Pendry [43], the *total* LEED wave function can be expressed in angular momentum components around atom i as:

$$\left\langle r \left| \Phi^+(k_{\parallel}) \right\rangle = \sum_{lm} A_{i;lm}(k_{\parallel}) \cdot \left[j_l(\kappa |r - r_i|) + t_{i,l} \cdot h_l^i(\kappa |r - r_i|) \right] \cdot Y_{lm}(\widehat{r - r_i}), \right. \tag{4.28}$$

i.e. a sum of the unscattered wave plus the contribution scattered by atom i. Simply leaving away the latter part generates:

$$\left\langle r \left| G_i^{end} \right| \varepsilon(k_{\parallel}) \right\rangle = \sum_{lm} A_{i;lm}(k_{\parallel}) \cdot j_l(\kappa |r - r_i|) \cdot Y_{lm}(\widehat{r - r_i}), \tag{4.29}$$

with Y_{lm} being a spherical harmonic, leading to:

$$\left\langle r_i; l, m \left| G_i^{end} \right| \varepsilon(k_{\parallel}) \right\rangle = A_{i;lm}(k_{\parallel}). \tag{4.30}$$

The evaluation of the second part of the tensor, Equation 4.27, yields a similar result. Following the lines of Rous and Pendry, one notices that:

$$\left\langle Z_0, k_{\parallel} + g' \left| G_i^{end\dagger *} \right| r_i; l, m \right\rangle = (-1)^m \left\langle r_i; l{-}m \left| G_i^{end} \right| Z_0, -(k_{\parallel} + g') \right\rangle, \tag{4.31}$$

and since

$$\langle r|\, G_0^+ \,|Z_0, -(k_{||}+g')\rangle = (1/2i\kappa k^+_{g'z}\Omega)\cdot\exp[iK^+_{g'}\cdot(r-Z_0)]$$

$$= (1/2i\kappa k^+_{g'Z}\Omega)\cdot\left\langle r\left|G_0^+\right|\varepsilon(-(k_{||}+g'))\right\rangle, \tag{4.32}$$

(with κ the modulus of the momentum of the "free" electron and Ω the area of the surface unit mesh for proper normalisation), we see that Equation 4.27 leads to a result very similar to that of Equation 4.30 except that the "incident" beam of the LEED state now has the lateral momentum component $-(k_{||}+g')$ instead of $k_{||}$:

$$\left\langle Z_0, k_{||}+g'\left|G_i^{end\dagger}\right|r_i;l,m\right\rangle = (1/2i\kappa k^+_{g'Z}\Omega)\cdot A_{i;lm}(-(k_{||}+g')). \tag{4.33}$$

Combining Equations 4.30 and 4.33, we see that the tensor may be obtained from conventional LEED calculations with different directions of incidence:

$$T_{i,g',l,m,l',m'} = \frac{1}{2i\kappa k^+_{g'z}\Omega}(-1)^m\cdot A_{i;lm}(-(k_{||}+g')). \tag{4.34}$$

In brief, the strategy to obtain the spherical-wave amplitude $A_{i;lm}(k_{||})$ is to perform a conventional LEED calculation (required anyways or calculate the LEED amplitudes $A^-_{g'}$ leaving the surface) and utilise the quantities introduced along the way. Standard LEED calculations are performed in two different representations. First, multiple scattering within a layer j (possibly composed of several sublayers i) is evaluated in angular momentum space, then the resulting layer diffraction matrices are transformed to plane wave representation, and combined to give $A^-_{g'}$.

For a given incident beam with component $k_{||}$, the plane-wave amplitudes $B^-_{j;g'}$ and $B^+_{j;g'}$ incident on a particular crystal layer j are required. For the self consistent layer stacking method [56], $B^-_{j;g'}$ and $B^+_{j;g'}$ do not immediately result from the full dynamic treatment of interlayer scattering. Instead, in a conventional layer stacking step, one combines the reflection and transmission matrices $R^\pm_{j;g_1,g_2}$ and $T^\pm_{j;g_1,g_2}$ of a layer with the effective reflection matrix $R^{eff,-}_{j+1;g_1,g_2}$ of an underlying stack of layers to obtain the reflexion matrix of that stack with layer j on top, $R^{eff,-}_{j;g_1,g_2}$. The formalism can easily be modified to additionally provide two more effective diffraction matrices $T^{eff,-}_{j;g_1,g_2}$ and $T^{eff,+}_{j;g_1,g_2}$, which describe the propagation of plane wave amplitudes $B^+_{j;g'}$, incident on layer j from above into the space between layer j and the underlying slab:

$$B^{-}_{j;g'} = T^{eff,-}_{j,g_1,g_2} \cdot B^{+}_{j,g'}, \tag{4.35}$$

$$B^{+}_{j+1;g'} = T^{eff,+}_{j,g_1,g_2} \cdot B^{+}_{j,g'}. \tag{4.36}$$

Once all layer stacking steps have been performed, the required plane wave amplitudes can be extracted for all layers j in question, beginning with known amplitudes $B^{+}_{1;g'}$ incident on the topmost layer ($j = 1$) and moving into the crystal recursively by way of Equations 4.35 and 4.36.

For each layer j, the only remaining task is to retrieve the spherical wave amplitudes $A_{i;lm}(k_{||})$ incident on sublayer i of that layer. In order to convert $B^{-}_{j;g'}$ and $B^{+}_{j;g'}$, one employs the so-called X matrix which contains all information on intralayer multiple scattering in the angular momentum representation *just before* the final scattering process of each scattering path occurs:

$$A_{i;lm}(k_{||}) = \sum_{l',m'} A^{0}_{i,lm}(k_{||}) \cdot (1 - X)^{-1}_{l'm',lm} \tag{4.37}$$

with

$$A^{0}_{i,lm}(k_{||}) = 4\pi i^{l} \sum_{g} B^{+}_{j;g} Y^{*}_{lm}(K^{+}_{g}) + B^{-}_{j;g} Y^{*}_{lm}(K^{-}_{g}). \tag{4.38}$$

Obtaining X is a part of every conventional LEED calculation.

4.3 The Erlangen Tensor LEED Package

Using LEED, two steps are required in order to obtain accurate crystallographic information about a given surface. The first step is simply (yet not always simple) to provide from experiment a sufficiently large data base of LEED intensity vs. energy, I,V spectra measured from the diffraction pattern of the surface under investigation. The second step is their numerical evaluation in order to retrieve the atomic configuration at the surface. Since multiple-scattering effects in LEED are strong, there exists no general method to extract the desired information directly from the experimental data. Instead, one resorts to a *best fit* strategy that involves the calculation of I,V spectra from many plausible models of the surface. By comparing these to the experimental curves, it is routinely possible to determine atomic positions near that surface (with an accuracy of a

few pm in favourable cases), its chemical composition including possible substitutional disorder, and other features such as vibrational amplitudes.

The Erlangen Tensor LEED package TensErLEED[6] provides an efficient computer code for the fast computation of LEED intensity spectra from virtually any periodic surface. For the full dynamic reference calculation, the muffin-tin approach and the layer stacking method are used. Amplitude changes in Tensor LEED are accessible for geometric, vibrational and chemical displacements from the reference structure. The package also contains a structural search algorithm designed for the retrieval of the global *R*-factor minimum between calculated and measured intensity spectra within a given portion of the parameter space used in Tensor LEED [7].

When putting the Tensor LEED approach into practise, one is simultaneously confronted with at least two necessities: first, a computational method giving easy access to I,V spectra for many different combinations of parameters, and second, a reliable search strategy to identify the *best fit* in the chosen portion of the parameter space, avoiding possible local minima. The Erlangen Tensor LEED package TensErLEED is a collection of programs tailored to tackle both tasks.

4.3.1 Phase Shifts Calculation

The calculation of the different phase shifts was performed using the Barbieri / van Hove package [2], which consists of the four following programs:

- ***PhSh0***

To start with, a free atom self-consistent calculation is performed for each of the N elements for which phase shifts are required. This is accomplished by using a self-consistent Dirac-Fock (*i.e.* relativistic approach which computes, separately for each element, the self-consistent atomic orbitals). The input needed at this stage is some basic information about the shell structure of the atom under consideration. The orbitals can then be used to compute the total radial charge densities associated to each element.

- ***PhSh1***

Here one computes the muffin-tin potential by following Mattheiss' prescription[7]. In essence, the atomic charge densities of the different elements making up the structure

[6] The TensErLEED package can be downloaded from the following address: http://cpc.cs.qub.ac.uk/summaries/ADNI_v1_0.html

[7] See for reference T. L. Loucks' 1967 book: "Augmented Plane Waves Method".

that we are interested in are superimposed to reflect the actual position of these elements in the structure. Note that for the purpose of obtaining the phase shifts needed in a LEED calculation it is not necessary to know the exact position of the atoms in the structure we are interested in, because the phase shifts and hence the calculated intensities are not strongly dependent on the manner in which the phase shifts are produced[8]. For the substrate atoms, a bulk terminated structure will be sufficient in almost all cases. In general, it's preferable to use a *slab-supercell* approach in defining the surface structure rather than embedding the adatoms in a sometimes artificial bulk structure. The slab is a free-standing film with a thickness of a few atomic layers, repeated periodically as a stack of identical slabs separated by slices of vacuum. The main subtlety about the slab approach is related to the definition of the muffin-tin zero (mtz)[9].

The total potential energy in each muffin-tin sphere is obtained by summing up the electrostatic component computed by using the charge density distribution, and a local Slater-like exchange term. The final potential is then shifted to set its zero at the level of the average energy in the interstitial region (mtz).

- ***PhSh2***

Here one computes the phase shifts from the muffin-tin potential(s) choosing one of the following routines:

- *PhSh2cav* is a "Cavendish" program which produces non-relativistic phase shifts (Schrödinger equation), with possible discontinuities in energy.
- *PhSh2wil* is a program, written originally by Williams, which again produces non-relativistic phase shifts (Schrödinger equation), but without discontinuities in energy. This is the preferred program for non-relativistic phase shifts calculations.
- *PhSh2rel* computes relativistic phase shifts (Dirac equation), that are possibly discontinuous in energy.

For our phase shifts calculations we used *PhSh2rel.*

[8] In principle, one could iterate the phase shifts calculation after the LEED structure analysis to further refine the structure.

[9] The computed mtz is the average of the energy in the interstitial region, incl. the vacuum. A reasonable value for mtz is the bulk value even in the case of a slab calculation (small errors are anyway adjusted by the fitting of the inner potential in the LEED calculation).

- ***PhSh3***

An important detail is that, as a function of energy, the calculated phase shifts may, and often do, show discontinuities by π, *i.e.* jumps by π at some energies. Since the LEED programs interpolate phase shifts between energies at which they are provided, such discontinuities would give totally erroneous results at such discontinuities. The phase shifts produced from *PhSh2rel* are not necessarily continuous in energy. *PhSh3* makes them continuous and produces an output suitable as input for LEED programs.

4.3.2 TensErLEED Optimisation

In this part, we give an overview of the main mathematical aspects of the TensErLEED procedure that leads to the calculated diffraction amplitude and the search for the *best* structure. These developments can be found in detail in references [36, 56].

4.3.2.1 Reference Calculation

In the reference calculation, full dynamic I,V spectra are calculated for one particular surface structure. Along with the usual I,V output, the outgoing LEED amplitudes $A^-_{g'}$ and the wave field components incident on each atomic site i in the structure, $A_{i;lm}(k_{||})$ and $A_{i;lm}(-(k_{||}+g'))$, are stored in separate files.

4.3.2.2 Calculation of the Amplitude Changes

The second step is the calculation of amplitude changes $\delta\tilde{A}^-_{i,g'}$ for a set of suitably chosen geometrical and thermal displacements around the reference values, for all chemical elements possibly found on that site.

Having obtained the tensor, the next step is to express perturbations of the reference structure in terms of individual atomic t-matrices. For the most important application of LEED, the determination of surface geometry, changes of individual atomic positions are translated into a modified t-matrix by evaluating the scattering properties of that atom from a different spatial origin. A displacement of the scatterer by an amount δr_i is expressed in terms of a translational operator $\tau(\delta r_i)$, leading to:

$$\delta t_i = \bar{t}_i - t_i = \tau(\delta r_i)\cdot t_i \cdot \tau(-\delta r_i) - t_i. \tag{4.39}$$

Details of the computational procedure in angular momentum space have been given by Rous and Pendry [42]. In general, if a lattice site i is occupied statistically by two

chemical elements A and B, the t-matrix for that site is given by:

$$t_i = x_i \cdot t_A + (1 - x_i) \cdot t_B, \tag{4.40}$$

where x_i is the probability of finding element A on site i and t_A and t_B are the t-matrices of the two elements A and B. In the "chemical" Tensor LEED this means:

$$\delta t_i = \tilde{x}_i \cdot t_A + (1 - \tilde{x}_i) \cdot t_B - t_i = \delta x_i \cdot (t_A - t_B) \tag{4.41}$$

when the occupation probability of site i by element A is changed to $\tilde{x}_i = x_i - \delta x_i$.

Of course, two different elements occupying the same lattice site i near a surface need not necessarily reside in exactly the same position. In that case, the modified t-matrix is obtained by averaging t_A and t_B when displaced from their original position according to Equation 4.39, yielding:

$$\delta t_i = \tilde{x}_i \cdot \tau(\delta r_{i,A}) t_A \tau(-\delta r_{i,A}) + (1 - \tilde{x}_i) \cdot \tau(\delta r_{i,B}) t_B \tau(-\delta r_{i,B}) - t_i. \tag{4.42}$$

In contrast to the previous case (Equation 4.41), the resulting t-matrix is now intrinsically aspherical (as in Equation 4.39) and would be difficult to handle in a full dynamic calculation. Using Tensor LEED, the additional computational effort is drastically reduced. In fact, it is possible to rewrite Equation 4.23 so that:

$$\tilde{A}^-_{g'} = A^-_{g'} + \sum_i (\tilde{x}_i \cdot \delta \tilde{A}^-_{i,g'}(\tilde{x}_i = 1) + (1 - \tilde{x}_i) \cdot \delta \tilde{A}^-_{i,g'}(\tilde{x}_i = 0). \tag{4.43}$$

In the case of substitutional disorder, the evaluation of Equations 4.42 and 4.25 is only required for $\tilde{x}_i = 1$ (full occupation by element A) and $\tilde{x}_i = 0$ (full occupation by element B). The results for all intermediate values $\tilde{x}_i$ can then be obtained in the final step of the calculation, again reducing the necessary computational effort.

Another frequent application of Tensor LEED is the treatment of thermal vibrations [29]. In the case of isotropic vibrations with a root mean square (RMS) amplitude a_{vib}, this effect is taken into account through the Debye–Waller factor (see section 4.2.3) multiplied to the atomic t-matrix. Thus, one obtains:

$$\delta t_i = \tilde{t}_i(a_{vib}) - t_i. \tag{4.44}$$

In practise, one frequently encounters multi-parameter problems where several different quantities are varied simultaneously that apply to the same lattice site i. It is then necessary to compute the desired amplitude changes for each combination of these parameters separately, storing them so that a superposition of amplitude changes from different atoms is possible in the final step.

4.3.2.3 Structural Search

In the last step, once the desired changes $\delta\tilde{A}^{-}_{i,g'}$ between amplitudes diffracted from the reference surface and the modified structure have been calculated, I,V spectra are calculated for different parameter combinations according to Equations 4.23 or 4.43, and LEED intensities of the modified structure can be obtained as usual, *i.e.:*

$$I_{g'}(E) = \frac{k^{+}_{g'z}}{k^{+}_{0z}} \left|\tilde{A}^{-}_{g'}\right|^2 . \tag{4.45}$$

In our case, the structural search algorithm described above handles the comparison to the experimental data, identifying the combination of structural parameters that yields the minimum *R*-factor (see below) within a given portion of the parameter space, *e.g.*, by conventional *R*-factor analysis [56, 37]. In case that the *best fit* deviates strongly from the *reference surface*, a further reference calculation using the *best fit* as its input is advisable in order to minimise possible uncertainties introduced by the Tensor LEED approximation. Needless to say, if there are different classes of structural models (*e.g.*, different adsorption sites on a surface), the procedure must be repeated for all of them [7].

4.3.3 The Pendry R-Factor

A successful LEED procedure requires very careful experiments and, for the more complicated systems, a long and tedious series of computations. Even though current theory can produce "good" agreement with experiment, the agreement is never perfect. The energies at which peaks occur are dictated by the phase of waves diffracted from the atoms in the surface and are directly related to the geometry, these energies are quite well produced by theory (*i.e.* to within much less than the peak width). Intensities are less accounted for because they are influenced by many effects that are not well understood - by thermal vibrations, by inelastic losses, and sometimes by data collection techniques [37]. A visual inspection of the curves is often adequate when it comes to

the determination of simple parameters, such as a choice between sites "A" and "B" for the location of an adsorbate atom, or a uniform dilatation of the spacing between the last two layers of atoms. Indeed, the eye is well equipped to neglect the relatively poor correlation of intensities, but to rapidly assimilate and evaluate this correlation becomes much too difficult and this procedure fails. For instance, in the analysis of a diatomic molecule on a transition-metal surface (*e.g.* CO on Re), a big number of separate graphs have to be generated and compared with experiment, each one containing many peaks. Accordingly, some automated criterion is required to summarise the overall quality of agreement. Preferably this would be contained in a single number, a reliability or "*R*-factor".

The requirements of a good *R*-factor are that it is chiefly sensitive to peak *positions*. It should not be at all sensitive to absolute intensities, but should pay some attention to relative intensities especially of features that are close in energy. It should also be a very simple function of the intensities not involving higher than the first derivative with respect to energy. Otherwise, calculations must be made at closely spaced energies to ensure numerical accuracy, with a consequent increase in computing times.

Many suggestions for *R*-factors have already been made [26, 55, 66], of which the very commonly used is that of Zanazzi and Jona. They propose

$$R_{ZJ} = \frac{A}{\delta E} \int \omega(E) |c I_{th}^{'} - I_{exp}^{'}| dE, \tag{4.46}$$

where

$$c = \frac{\int I_{exp}}{\int I_{th}}, \; \omega = \frac{|c I_{th}^{''} - I_{exp}^{''}|}{|I_{exp}^{'}| + \varepsilon}, \; \varepsilon = |I_{exp}^{'}|_{max},$$

where the integrals extend over a range δE. A is chosen to normalise R_{ZJ} to unity for uncorrelated curves

$$A = \frac{\delta E}{(0.027 \int I_{exp})}.$$

Zanazzi and Jona say that empirically $R = 0.2$ is good agreement, $R = 0.35$ mediocre and $R = 0.5$ is bad agreement [66].

This function has proven useful in several determinations but is clearly empirically based and has the disadvantage of involving the second derivatives of the intensities. Pendry tried to construct an *R*-factor starting from the logical premise of intensity to intensity. The *R*-factor is then analysed statistically, and a more precise meaning is given to its value in terms of levels of confidence. In particular the way the significance level of *R* depends on the size of the database is considered. This leads to the definition

of the double reliability factor, *RR*, which determines, amongst other things, the level at which a minimum in *R* becomes significant. It will be shown that *RR* varies as the square root of the size of the database.

LEED curves consist for the main part of a series of lorentzian peaks:

$$I \backsimeq \sum \frac{a_j}{(E-E_j)^2+V_{0i}^2}. \tag{4.47}$$

Their widths are dictated by the imaginary part of the inner potential, V_{0i},

$$\Delta E = 2|V_{0i}| \tag{4.48}$$

and in most materials V_{0i} is approximately independent of the electron energy, above say $30\,eV$, and takes a value of around $-5\,eV$.

Other features can sometimes appear in the curves. For example multiple scattering can induce zero intensity in the curves. In fact these "zeroes" contain much structural information because the phase of the diffracted wave changes rapidly in their vicinity. Therefore, the zeroes should not be suppressed in a comparison of theory and experiment. Occasionally sharp features due to surface resonances appear. Electrons trapped in surface states sometimes have long lifetimes if the state sits mainly outside the surface, and produce narrow resonances.

For a series of widely spaced peaks, the criterion of insensitivity to the amplitudes is met by the logarithmic derivative of the intensity:

$$L(E) = \frac{I'}{I}, \tag{4.49}$$

which in the case of lorentzian peaks (Equation 4.47), reduces to:

$$L \backsimeq \sum_j \frac{-2(E-E_j)}{(E-E_j)^2+V_{0i}^2}.$$

At each peak in the intensity *L*, we see a $\pm$ excursion of amplitude:

$$L = \pm\frac{1}{|V_{0i}|} \qquad at \;\; E = E_j \mp |V_{0i}|. \tag{4.50}$$

This completely eliminates the amplitudes if the peaks are well separated. If the peaks overlap to some extent, the relative intensities do affect *L* but, the relative intensities of closely spaced peaks are quite well reproduced and it is desirable to have some sensitivity to this correlation. Comparison of L_{th} and L_{exp} works well except when *I* is

zero, as it can be when multiple scattering is present. The infinity in L gives too high emphasis to zeroes. Pendry therefore prefers to use instead of L a function, which gives similar emphasis to zeroes and lorentzian peaks:

$$Y(E) = \frac{L^{-1}}{(L^{-2} + V_{0i}^2)}. \tag{4.51}$$

There are two caveats when calculating Y for experimental data. Noise in the data can be dangerous in giving spurious variations in I'. Some smoothing of curves should then be attempted, *e.g.:*

$$\tilde{I} = \frac{1}{\pi} \int \frac{I(E')\sum dE'}{(E-E')^2 + \sum^2}, \tag{4.52}$$

where we choose $\Sigma < |V_{0i}|$ to avoid losing real information from $\widetilde{\mathrm{I}}$. The second caveat concerns the background that occurs in all LEED curves. Y is specifically designed to pick up small peaks well separated from large ones, and the presence of background noise will severely interfere with this process. Either the background must be carefully subtracted experimentally, or the theory must have an equivalent background added (but at the price of losing information in the weak peaks) or the background can be fitted by a smoothly varying curve whose parameters are adjusted to optimise the final R-factor. The latter is defined as:

$$R_P = \frac{\sum\limits_g \int (Y_{gth} - Y_{gexpt})^2 dE}{\sum\limits_g (Y_{gth}^2 + Y_{gexpt}^2) dE}. \tag{4.53}$$

Chapter 5

Results and Discussion

This chapter is dedicated to the LEED structural analyses performed for the noble metals Cu, Ag, and Au on the Re($10\bar{1}0$) surface, in this order respectively with the increasing atomic number. We will start by re-analysing the clean Re($10\bar{1}0$) surface in light of a recently measured LEED-I,V data set, while experimental results concerning CO adsorption on the same Re surface will be presented in the Appendix. A review of the main experimental findings collected in our group (LEED, TPD, and MEED) is given for each system metal/Re [39, 44, 33], followed by the corresponding LEED analysis using the TensErLEED computational package described in section 4.3.

All calculations were performed on a "Dell Optiplex 755" machine with an Intel Core2 Duo CPU ($3\,GHz$, $3.2\,GiB$ RAM) utilising Ubuntu Linux Release 9.04 (Jaunty Jackalope) and the GNU Fortran 95 compiler Gfortran-4.3.3.

5.1 The Clean Rhenium($10\bar{1}0$) Surface

The re-investigation of the clean rhenium($10\bar{1}0$) surface was briefly undertaken as an introductory part to the forthcoming calculational work on the adsorbate-covered Re surface. In fact, the major findings as to the surface termination and the determination of its interlayer spacings have been the subject of Davis and Zehner's paper from 1980 [12], and later by Döll et al. in the study of anomalous hydrogen adsorption on Re and Ru($10\bar{1}0$) [15]. The latter decided to perform their LEED analysis by using a $50-200\,eV$ energy range in order to avoid complications concerned with choices for some nonstructural parameters in the lower energy region below $50\,eV$; *e.g.* phase shifts and the imaginary component of the inner potential. They also restricted it to the comparison

between beams (0,1) and (1,1). Figure 5.1 shows the LEED (1×1) pattern produced by the clean Re$(10\bar{1}0)$ surface.

On the other hand, in Pauls' work on the same clean surface [33], the LEED analysis was extended to two additional beams (1,0) and (0,2) in the energy range $50-230\,eV$.

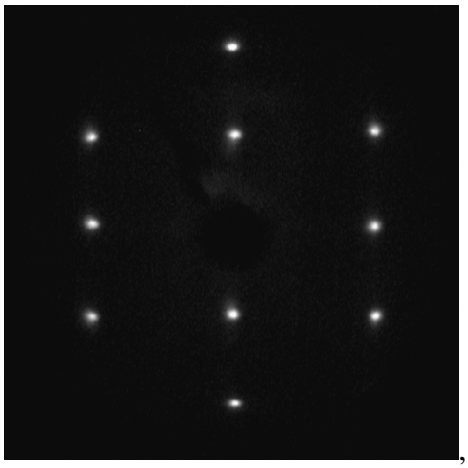

Figure 5.1: Re(1×1) LEED pattern.
The LEED image of the clean Re$(10\bar{1}0)$ surface was recorded at $E_e = 76\,eV$ and $T = 200\,K$.

In the present work, a new LEED-I,V data set was used, recently measured by Przyrembel[1] as a pre-step in the investigation of the Cu/Re$(10\bar{1}0)$ system [39]. Indeed, we found it interesting to get acquainted with the TensErLEED package (described in chapter 4) by re-investigating this already known surface and comparing the new resulting interlayer spacings to the previous ones. The present data set includes 8 beams measured for a wider energy range of $50-340\,eV$.

5.1.1 Surface Termination

In the TensErLEED reference calculation for the Re$(10\bar{1}0)$ surface, a rectangular unit mesh with lattice constants $a = 2.761\,\text{Å}$ and $c = 4.456\,\text{Å}$ was used [28].

Similarly to Pauls and Davis et al. [33, 12], full dynamical LEED calculations were performed for both "A"- and "B"-terminations (*cf.* section 2.2.1, Figure 2.2) at normal electron incidence. For the "A"-termination, a slab was used that consists of two composite layers with an interlayer distance of $1.594\,\text{Å}$ (bulk value). The "B"-termination

[1] The same chamber and crystal sample were used to generate both Pauls' and Przyrembel's I,V data sets. Among these measurements, the crystal had undergone many sputtering and annealing cycles and therefore can be considered as completely new and clean.

was built as an "A"-terminated crystal + 1 sublayer ($\frac{1}{2}$ composite layer), separated from the "A"-terminated slab by 0.797 Å.

A simple visualisation of the spectra as shown in Figure 5.2 suffices to deduce that not only for energies below $230\,eV$ but also up to $340\,eV$, the "B"-termination can definitely be ruled out and this based on these two arguments:

- it displays intensities much lower than the measured ones
- several peak contradictions with the experimental curves (*i.e.* maxima vs. minima and vice-versa) occur in all the beams.

5.1.2 Structural Parameters

5.1.2.1 Experimental Data Measured by Pauls

New fully dynamical LEED calculations for the clean Re($10\bar{1}0$) surface using the TensErLEED package were performed [7]. In Table 5.2 the geometrical displacements obtained by fitting Pauls' experimental data are compared with Pauls' own best fit values [33] as well as with the values obtained by Davis et al. [12] and Chen [10]. Note that Pauls used van Hove's 1993 version[2] of the Tensor LEED package [53].

	d_{12}	d_{23}	d_{34}	V_0	R_P	R_{ZJ}	ΔE
Present work	-11%	-1%	-2%	$10.7\,V$	0.23	–	$724\,eV$
Pauls	-12%	-2%	–	$10.8\,V$	0.22	0.08	$724\,eV$
Davis et al.	-17%	$+1\%$	–	$14.0\,V$	–	0.19	$400\,eV$
Chen	-7.3%	$+0.2\%$	$+0.9\%$	–	–	–	–

Table 5.1: Comparison of structural parameters for Re($10\bar{1}0$) - literature values.
The d_{ij} represent the layer relaxation (in percent) from the bulk value between layers i and j.
"Present work" and "Pauls" values are obtained by fitting Pauls' experimental data [33]. They are compared to those of Davis et al.
Chen's values were obtained by the local-volume potentials method (LVP) [10]. Note also that theoretical estimates by Auret and van der Merwe, using atomic pair potentials, indicate, *e.g.,* that the equilibrium linear dimensions of net meshes may change by 5% and elastic constants by more than 50% in going from the bulk crystal to a monolayer [52].

[2]The thermal vibrational effects on the surface atoms in van Hove's TLEED version [53] are expressed as the layer's experimentally deductible effective Debye temperature Θ_D. Whereas the same quantity can be optimised as an independent parameter in the new TensErLEED version [7] provided one introduces a plausible starting-value.

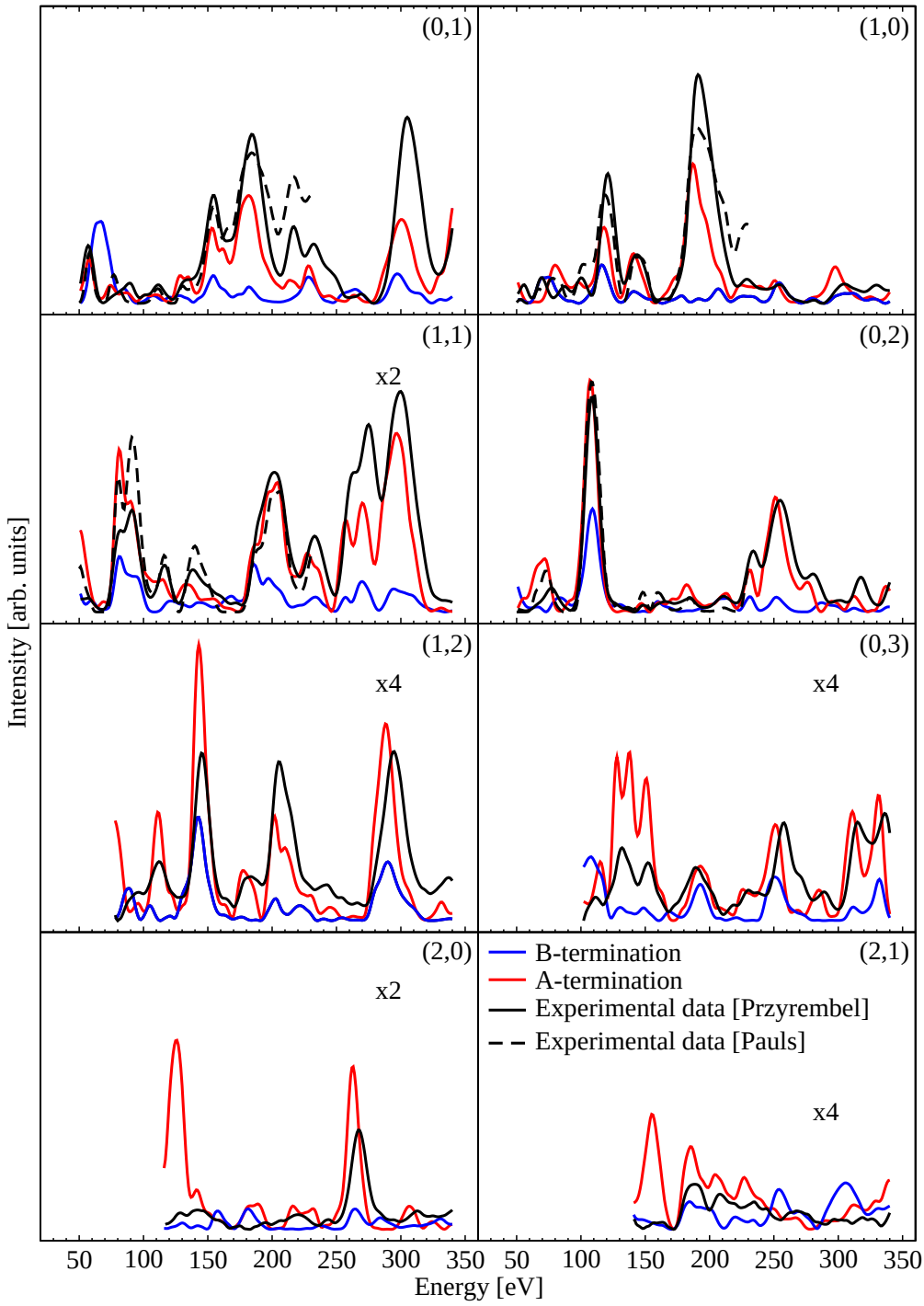

Figure 5.2: LEED-I,V spectra for the "A"- and "B"-terminated Re(10$\bar{1}$0) surface. Comparison between theoretical LEED-I,V spectra for the "A"- and "B"-terminated clean Re(10$\bar{1}$0) surface with the experimentally measured data by Pauls and Przyrembel. In Pauls' data only the 4 top beams are available.

By these calculations, it was possible to reproduce quasi-identical I,V spectra to Pauls' ones. The slight difference in the R_P-factor of 0.01 can be considered as negligible, given that the statistical error of the Pendry R-factor for Pauls' range of data equals merely 0.05, and is in general defined as:

$$var(R_p) = R_{P(best)} \sqrt{\frac{8V_{0i}}{\triangle E}},$$

with the imaginary component of the inner potential, $V_{0i} = 5\,eV$ and $\triangle E$ the total energy width of all beams, in this case $724\,eV$. The condition for an acceptable fit is that the R_P value is lower than the limit $0.22 + var(R_P)$, which in this case is fully satisfied. At this stage, one can verify that the programme can be properly run and thus, existing results can be, down to minor fluctuations, well reproduced.

5.1.2.2 Experimental Data Measured by Przyrembel

The geometrical displacements obtained for the "A"-terminated Re($10\bar{1}0$) surface were found to be in very good agreement with those calculated by Pauls, who also obtains a lower Zanazzi and Jona R_{ZJ}-factor[3] than the one obtained by Davis et al.; see Table 5.2. As a next step, we wanted to optimise Przyrembel's new[4] experimental data [39], and compare the resulting geometrical displacements with the previous ones; the point being the extrapolation of the analysis to a wider energy range with more reflected beams to fit.

Given that we intentionally considered the raw data, *i.e.* including $E < 150\,eV$ for the (2,0) beam and $E < 185\,eV$ for the (2,1) beam, we wanted to show that it is sometimes necessary to "cut out" the experimental data that do not seem to be reproducible by any means. The presence of this kind of "artefacts" fortunately doesn't divert the optimisation trend[5]. Indeed, in Table 5.2 we show that the "mediocre" R_P value of 0.42 is not representative of non-satisfactory LEED-I,V analysis, but rather reflects the discrepancy in the intensity as well as the quality of the experimental data.

[3]Pendry thoroughly compares Zanazzi and Jona's R-factor with the R-factor he defines, see section 4.3.3. In this work we restrict our calculations of the reliability factor given by Pendry. The R_{ZJ} value is only given according to Pauls' presentation of his results.

[4]We refer to Przyrembel's experimental I,V spectra by citing his diploma thesis within which he did the measurements. The data themselves are published in the present PhD thesis.

[5]Note that the search procedure can be trapped in local minima with a converging R_P value but with non-fully optimised structural parameters.

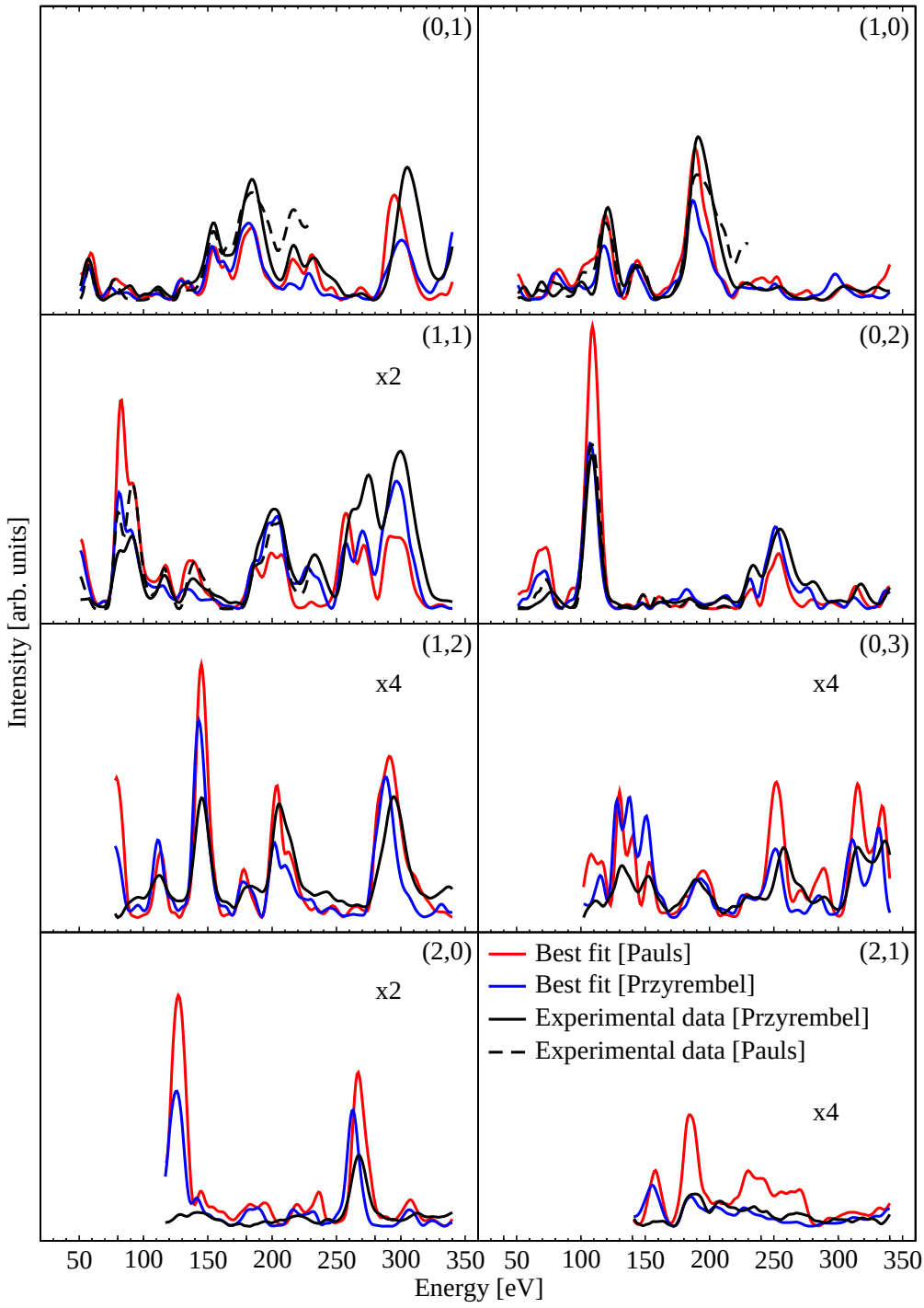

Figure 5.3: LEED-I,V best fits for the Re(1×1) phase.

Comparison between LEED-I,V spectra obtained by Pauls and the ones fitted on Przyrembel's experimental data.

In fact, when we compare Pauls' best fit with Przyrembel's data we find an R_P value of 0.50, which in normal cases would rule out the corresponding structural model. In Figure 5.3 Pauls' fit (red curve) and our optimised LEED-I,V spectra, this time based on Przyrembel's data (blue curve), are displayed. We observe that both curves satisfactorily reproduce the same topography. The peak intensities, as one would expect, vary from the one fit to the other, as they both depend on the experimental conditions and on the surface itself. The (2,1) beam illustrates well this discrepancy and can be seen as a good indicator as to whether one should include it or not in the optimisation procedure. The relaxation of the topmost Re layer calculated from this new analysis is found as -14%, which remains in very good agreement compared to Pauls' value, -2.2% of Re-topmost layer's relaxation, and up to $+3.6\%$ when compared to that value from Davis et al.

	d_{12}	d_{23}	d_{34}	V_0	R_P	ΔE
Pauls' best fit	-12%	-2%	–	$10.8\,V$	0.50	$724\,eV$
Present work	-14%	-1%	-1%	$9.8\,V$	0.42	$2007\,eV$

Table 5.2: Comparison of structural parameters for Re($10\bar{1}0$) - past and present work. "Present work" refers to the parameters obtained by fitting Przyrembel's experimental data, to which Pauls' best fit is also compared.

We can conclude from this introductory analysis, consisting of the TensErLEED optimisation of two different experimental I,V data sets of the clean Re($10\bar{1}0$) surface that the quality of the experimental data plays a major role in the degree of reliability, in this case a low value of the Pendry R-factor. Still the optimisation of the structural parameters leads to values that agree with those in the literature. This pre-analysis also predicts how delicate the task of investigating more complex systems can be, the aim of which remains to find the right balance between the quality of the experimental data and the R_P-factor estimation.

5.2 Copper Adsorption on Rhenium($10\bar{1}0$)

Thin copper film adsorption on the Re($10\bar{1}0$) surface was investigated in our laboratory by Przyrembel by means of LEED, MEED, and TPD. The experimental setup and conditions are described in more detail in Przyrembel's diploma thesis [39]. For the sake of convenience, we summarise the important experimental findings here, in the sequence LEED, TPD, and MEED, before we move on to the structural analyses.

We recall that as far as the Re hcp ($10\bar{1}0$) surface is concerned, the adsorbate (Cu, Ag, Au) coverage is defined in the following manner: This surface has an atomic density of $8.125 \times 10^{18}\, topmost\, atoms/m^2$ and provides as many equivalent adsorption sites. Hence, a complete monolayer of adsorbate atoms (Cu, Ag, Au) [$\Theta_{ads} = 1\,ML$] is reached when all these adsorption sites are actually occupied. In this configuration, the surface termination has switched from the less corrugated "A" to the more corrugated "B" termination. Due to the peculiar hcp surface geometry, the ($10\bar{1}0$) surface can (and will) accommodate another monolayer in order to rebuild the energetically more favourable "A" termination, and we end up with a total of two monolayers = one bilayer (*BL*) as the stable configuration. This is the reason why ($10\bar{1}0$) hcp films usually grow in bilayers.

5.2.1 Experimental Results

5.2.1.1 LEED

In the previous section we discussed that the clean, unreconstructed Re($10\bar{1}0$) surface exhibits a well-ordered (1×1) diffraction pattern with sharp and bright spots on a very low background. The deposition of Cu in different amounts at $800\,K$ causes at first a slight increase of the LEED background[6], but no change in the (1×1) geometry of the Re substrate surface. As one approaches the bilayer Cu coverage, this background reaches a minimum, and again a bright and sharp (1×1) diffraction pattern appears, as shown in Figure 5.4.

After depositing more than $1\,BL$ of Cu, the background increases again indicating some inherent disorder and roughness, but the pattern is still dominated by the (1×1) geometry of the Re host surface. This can *a priori* be taken as strong evidence for pseudomorphic growth of the Cu atoms.

The fact that the (1×1) pattern prevails, independent of the Cu coverage, Θ_{Cu}, along with the observation that under no circumstances (temperature, coverage, deposition

[6]The elevated temperature was chosen in order to avoid CO coadsorption [35].

rate) a Cu-induced LEED superstructure emerged (unlike the Au and Ag on Re(10$\bar{1}$0) systems, studied at a later stage), supports our assumption that in the sub-bilayer coverage regime, pseudomorphic (1×1) oriented Cu islands coexist with 2*D* Cu lattice gas. With increasing Cu coverage, these islands increase in size and gradually coalesce.

In LEED, this behaviour suggests for the coverage range $0 < \Theta_{Cu} < 1\,BL$, that the intensities of the observed diffraction pattern represent a linear superposition of uncovered Re(1×1) areas and locally completed Cu(1×1) bilayer film islands with the Cu coverage Θ_{Cu} as a parameter, what is also found experimentally, according to the relation [39]:

$$I^{h,k}_{total} = \left(1 - \frac{\Theta_{Cu}}{\Theta_{BL}}\right) I^{h,k}_{Re(1\times1)} + \frac{\Theta_{Cu}}{\Theta_{BL}} I^{h,k}_{Cu(1\times1)}. \tag{5.1}$$

One requirement here is that the sample temperature during the LEED-I,V measurements (ca. $360\,K$) is sufficiently low that the mobility of individual Cu atoms is frozen and the incoherent diffuse scattering from Cu lattice gas atoms is negligible.

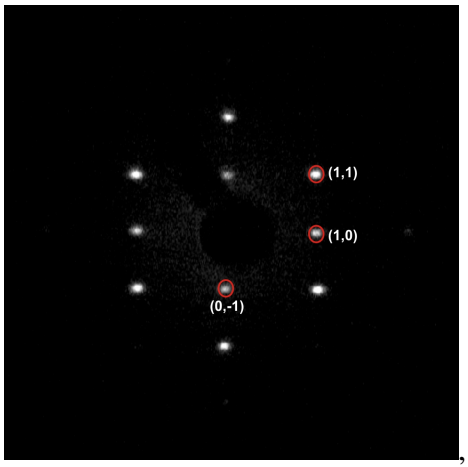

Figure 5.4: Cu/Re(10$\bar{1}$0) (1×1) LEED pattern.
The LEED image of the system Cu/Re(10$\bar{1}$0) was recorded at $E_e = 154\,eV$, $T = 358\,K$, and $\theta_{Cu} = 0.98\,BL$. A coverage-dependent linear combination was performed for all observed beams and is shown for the red-circled diffraction spots (0,-1), (1,0), and (1,1) in [39].

The growth and development of the Cu surface phase were not only followed by LEED but also by temperature-programmed desorption (TPD, section 5.2.1.2) and medium-energy electron diffraction (MEED, section 5.2.1.3). The development of the Cu film morphology can be subdivided into three regimes, the sub-bilayer ($\Theta_{Cu} < 1\,BL$), the closed bilayer ($\Theta_{Cu} = 1\,BL$), and the multilayers with $\Theta_{Cu} > 1\,BL$.

5.2.1.2 TPD

In Figure 5.5 we display a series of Cu TPD spectra, spanning the initial Cu coverages between $0.06 - 2.6\,BL$. Clearly, two Cu TD states appear: a high-temperature state between 1150 and $1220\,K$ denoted as β, which is associated with the Cu atoms that are in direct chemical contact with the Re surface (first BL) and an α state coming off between 940 and $1100\,K$ as soon as the bilayer coverage is exceeded.

Except for small Cu coverages ($\Theta_{Cu} < 0.2\,BL$) all TD maxima of the β state are located on a single exponentially rising curve indicating a clear zero-order desorption kinetics.

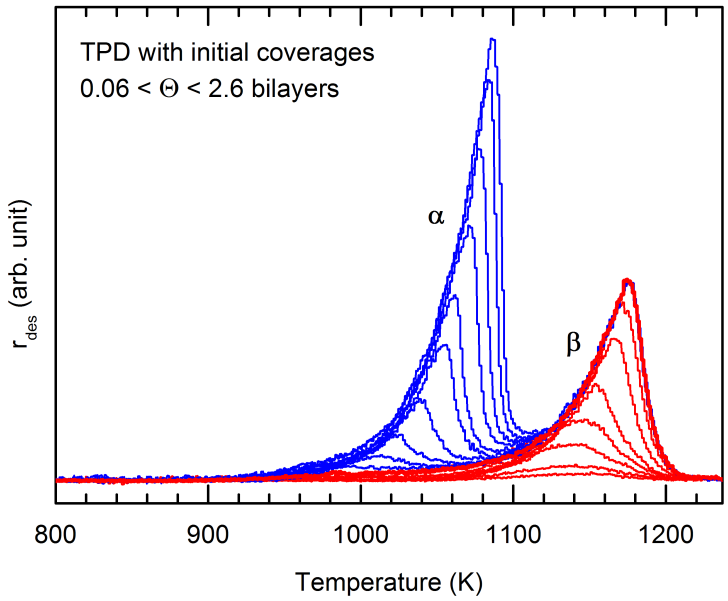

Figure 5.5: Cu/Re($10\bar{1}0$) TPD spectra.
The spectra are shown for initial Cu coverages, $0.06 \leq \Theta_{Cu} \leq 2.6\,BL$ [39].

A detailed analysis of the TPD spectra yields (strongly coverage-dependent) desorption energies of $\triangle E^{\beta}_{des} = 320 - 340\,kJ/mol$ for the β state at low coverages; the increase with coverage pointing to attractive Cu-Cu interactions that are responsible for the observed island growth. The α state, on the other hand, reflects those Cu atoms that form the multilayers ($\Theta_{Cu} > 1\,BL$). Again the α maxima coincide with a single exponential curve that describes the evaporation (sublimation) of the bulk Cu phase. The respective desorption energy analysis yields $\triangle E^{\alpha}_{des} \approx 300\,kJ/mol$, somewhat lower than the Cu heat of sublimation ($\triangle H^{1000\,K}_{sub,Cu} \approx 333\,kJ/mol$) and the higher coverage ($\Theta_{Cu} > 0.3\,BL$) limit $\triangle E^{\beta}_{des} \approx 360\,kJ/mol$.

5.2.1.3 MEED

We recall that the MEED data were always taken *in situ*, *i.e.* during film deposition. Not only do they reflect the various stages of the Cu-surface interaction including the growth mode but they also enable us to calibrate the Cu coverage. The MEED intensity is plotted against the Cu evaporation time (for fixed Cu flux).

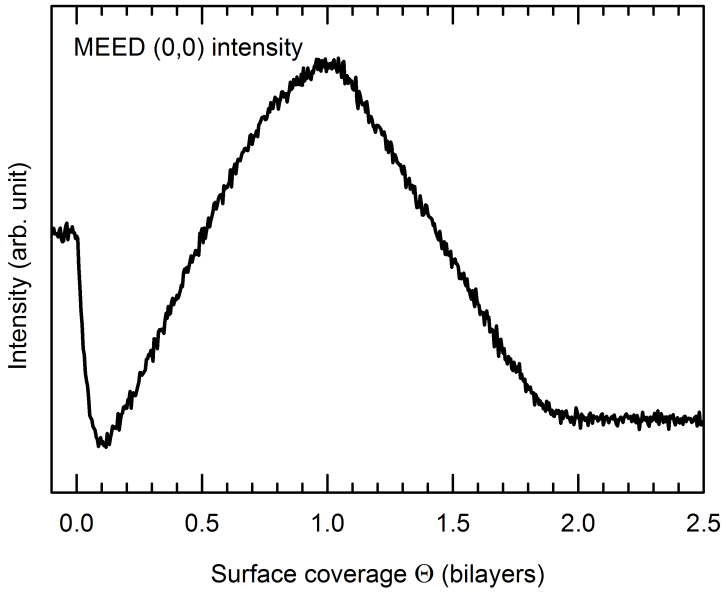

Figure 5.6: Cu/Re(10$\bar{1}$0) MEED (0,0) intensity as a function of Cu coverage.
The sample temperature was $T = 800\,K$, the electron energy $5\,keV$. Clearly, the highest intensity (electron reflectivity) is obtained for the complete first bilayer (*BL*) [39].

The MEED maximum always coincides with the saturation of the β peak of the desorption spectra. This means that the highest reflectivity of the Cu-covered sample is reached for the complete bilayer coverage. According to our previous considerations about the surface stability of (10$\bar{1}$0) hcp surfaces this means that also the Cu closed layer film is terminated by the smooth "A" configuration. Along with our LEED observations of section 5.2.1.1, which showed right at this coverage a clear (1×1) pattern with very low background.

The continuous MEED-intensity decrease following the first bilayer coverage as evident from Figure 5.6 clearly indicates incomplete multiple layer growth with its inherent surface roughness and, hence, points to a kind of Stranski-Krastanov growth mode.

5.2.2 LEED Structural Analysis

In the following part, we are going to present the results of our dynamical LEED structure analyses of the Cu layers. The purpose of this effort is to determine, by means of a quantitative LEED-I,V analysis, the location of the Cu atoms on the Re(10$\bar{1}$0) surface. In detail, we will show how the theoretical TensErLEED calculation can be employed to confirm the pseudomorphic character of the growth, to disentangle the exact (1×1) surface geometry, and to assess possible structural changes exerted on the Re surface by the Cu overlayer(s).

5.2.2.1 The Closed Bilayer

As described in Section 4.3, the Barbieri and van Hove code was used to calculate the Cu and Re phase shifts [2]. If not stated otherwise, a slab of two ad-layers stacked above a Re bulk (up to 10 layers) was built in a hcp fashion. For the muffin-tin radius of Re a value of $2.58\,a.u.$ (that corresponds to the atomic radius $r_{Re} = 1.37\,\text{Å}$) is a reasonable choice. For Cu on the other hand, *two* phase shifts calculations were performed. The first one used a muffin-tin radius corresponding to the Cu covalent radius, *i.e.* $2.41\,a.u.$ ($r_{Cu} = 1.27\,\text{Å}$), and the second one tried a muffin-tin radius that is equal to that of a Re atom ($2.58\,a.u.$). Since no perceptible differences could be seen in the LEED-I,V spectra, calculated with these two different values, phase shifts calculations were restricted to the use of the atomic radii values. The phase shifts calculations were extended up to angular momenta of $L = 12$, whereby a relativistic computation was considered.

Concerning the Cu(1×1) reference structure for the closed bilayer, $\Theta_{Cu} = 1\,BL$, TensErLEED calculations were performed for 8 different structure models, of which a schematic top and side view are presented in Figure 5.7.

Since there is no direct way to gather exact information about the *local* Cu coverage from the experiment, it appears necessary to also perform theoretical LEED-I,V calculations on structure models including "B"-terminated structures with $1\,ML$.

The first step was to consider the four possible structure models for $1\,ML = 0.5\,BL$. The "best" R_P value was found for the pseudomorphic site, *i.e.* long-bridge (structure (b) in Table 5.3). From this point, we restricted the reference calculation to the four structures that can be possibly built on the long-bridge sites, the twelve[7] remaining possibilities thus being ruled out.

[7] Although implausible, the 12 remaining models were nevertheless tested in a first attempt as no optimisation of the Cu(1×1) phase could be successful with the input parameters found for the optimised Au(1×1)/Re phase.

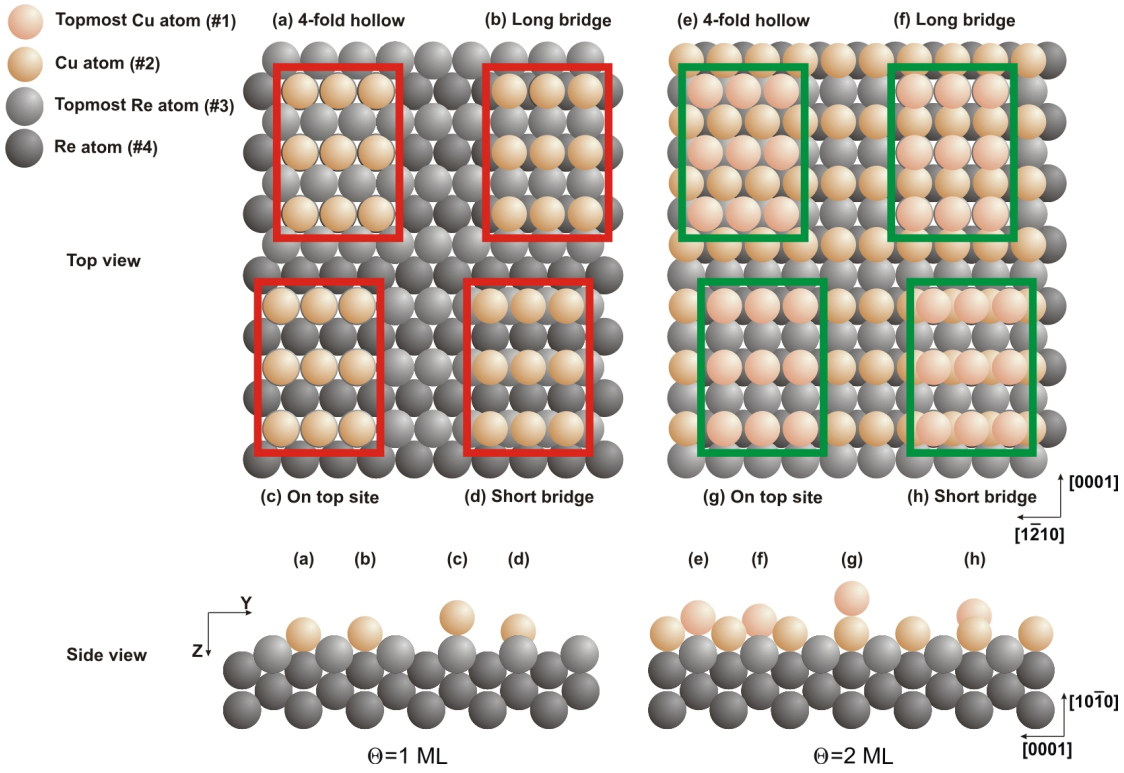

Figure 5.7: Different structure models tested for the Cu(1×1) phase.
The eight most plausible structures are depicted for $\Theta = 1\,ML$ and $2\,ML$ ($1\,BL$). The red and green frames delimit the surface for each occupancy site. Cu and Re atoms are drawn by keeping their real radii ratio.

The present LEED-I,V analysis involved a set of 8 LEED spectra measured at normal incidence in the energy range $38-342\,eV$, the spectra were produced by averaging symmetry-equivalent spots, for instance the (1,1) beam results from averaging the (1,1), (1,-1), (-1,1), and (-1,-1) beams. Choosing first all possible high-symmetry adsorption sites (4-fold hollow, on-top, long-bridge, and short-bridge), we then proceed to the Cu(1×1) reference calculation. For this purpose, interlayer distances resulting from the optimisation of the Au(1×1)/ Re(10$\bar{1}$0) structure were taken as "plausible" initial values [34]. Surprisingly, this assumption did not lead to any reference structure to which the perturbational procedure could be successfully applied. In fact, not a single model of the eight proposed ones could be optimised such that the R_P value would converge to a minimum value.

Figure 5.8 underlines the fact that an inappropriate choice for the reference parameters can lead to totally unacceptable "theoretical structures". A decisive parameter

here is the choice of an appropriate vertical layer distance d_{12} (z direction[8]). In a first attempt, we simply tried d_{12} that had proven to be good for calculating the Au(1×1) phase on Re(10$\bar{1}$0), *i.e.* $d_{12} = 0.82$ Å.

However, it soon turned out that this represents a bad starting value for the Cu(1×1) layer. For this reason, interlayer distances with values in the vicinity of the Re bulk values were implemented in the reference calculation. This assumption is supported by the fact that the Cu atomic radius is by $\sim 7\%$ smaller than Re, and even by $\sim 12\%$ smaller than Au. An immediate decrease of about -18% in the R_P value (comparison between the R-factors for structure (e) with d_{12}(Au(1×1)) and d_{12}(Re(10$\bar{1}$0)) is obtained, which indicates that this hypothetical model is more likely to lead to convergence than the previous one. One can thus assess, up to a certain limit, how the TensErLEED programme can be sensitive, and therefore the choice of the initial values is decisive for the continuity of the optimisation procedure. The Pendry R-factor values for the eight reference calculations with Re bulk values are presented in Table 5.3.

Reference calculations carried out with this assumption led to a clear advantage for structure (e), namely a bilayer ($\Theta_{Cu} = 2\,ML$) with a pseudomorphic growth of Cu atoms. We recall that a good test for the "best" structure is the estimation of the statistical error, $var(R_P)$, previously defined in paragraph 5.1.2.1 on page 59. The sum of experimental I,V energy ranges for this system is $\triangle E = 1867$ (*cf.* Table 9.2 on page 149), the statistical error, has thus a value of 0.1. This makes the optimisation of the remaining structures unnecessary: the next best structure is by 0.12 "worse" than structure (e).

Reference structure	Site	(#) of Cu layers	R_P-factor
(a)	4-fold hollow	1	0.88
(b)	Long-bridge	1	0.77
(c)	On-top	1	0.91
(d)	Short-bridge	1	0.93
(e)	4-fold hollow	2	**0.65**
(f)	Long-bridge	2	0.82
(g)	On-top	2	0.86
(h)	Short-bridge	2	0.88

Table 5.3: Reference structure calculations for the Cu(1×1) phase.

[8]For a (1×1) symmetry, the Cu-atoms' x and y coordinates are the same as those of the Re bulk.

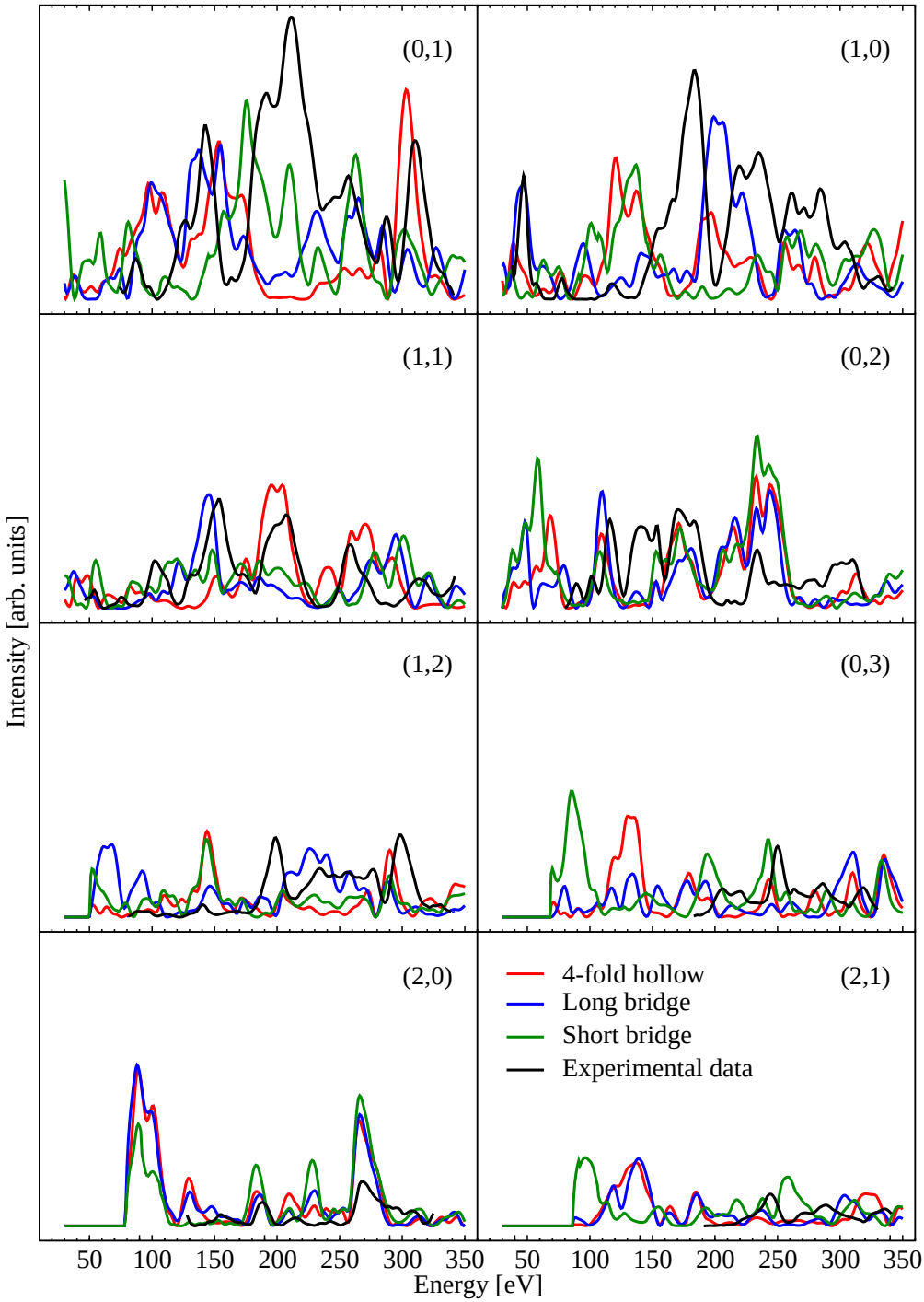

Figure 5.8: LEED-I,V reference structure spectra for the Cu(1×1) phase.
The three "best" reference structures calculated with gold parameters are presented. The occupancy site refers to the Cu-site in the topmost layer. The Cu-on-Re layer is built in a pseudomorphic fashion, *i.e.* with Cu atoms located in the long-bridge site. The corresponding, totally unacceptable, R_P values are: 0.93, 0.94, and 0.80 for short-bridge, long-bridge, and 4-fold hollow sites, respectively.

The optimisation of (1×1)-symmetry structures is relatively easy due to their symmetry in x and y directions. The calculation of amplitude changes was done for the four chemical entities constituting the four top layers: two Cu top layers deposited on two Re layers. This pseudomorphic configuration is depicted in Figure 5.9, the 4 underlying layers form the Re-substrate.

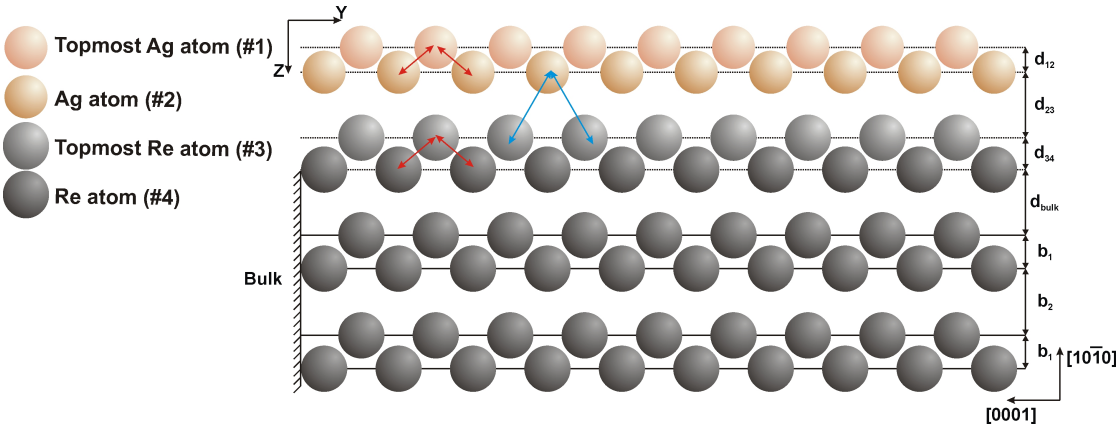

Figure 5.9: Geometry of the Cu(1×1) optimised structure.

The d_{ij} interlayer distances were simultaneously varied, b_i represent the fixed bulk interlayer distances. The arrows represent the respective atomic distances, which were deduced from the TensErLEED calculations. The arrows in red indicate the distance between atoms in layers with a termination sequence B-A, L_{BA}, and are deduced from the expression: $L_{BA} = \sqrt{(\frac{a}{2})^2+(\frac{c}{2})^2+d_{ij}^2}$. Whereas the blue arrows indicate the distance between atoms in layers with a termination sequence A-B, L_{AB}, defined as $L_{AB} = \sqrt{d_{ij}^2+(\frac{c}{2})^2}$. With a and c being the lattice parameters and d_{ij} the respective calculated interlayer distances.

Note that for all reference structures, the inner potential was initially chosen as $V_0 = (-11.80-5i)\,eV$ with the real part used as a fitting parameter.

In the calculation of the amplitude changes, two types of parameters were subject to variation, namely the $\delta\tilde{A}^{-}_{i,g'}$ (described in paragraph 4.3.2.2) for each lattice site i, the thermal vibrational amplitudes v_i, which account for the atomic displacements (in Å) due to temperature (see 4.2.3 on page 40), and the geometrical displacements of the atomic components of the four top layers, d_{ij}, shown in Figure 5.9. A variation step of down to 0.01 Å for each parameter was considered for the thermal vibrational amplitudes and a step of 0.001 Å for the geometrical displacements.

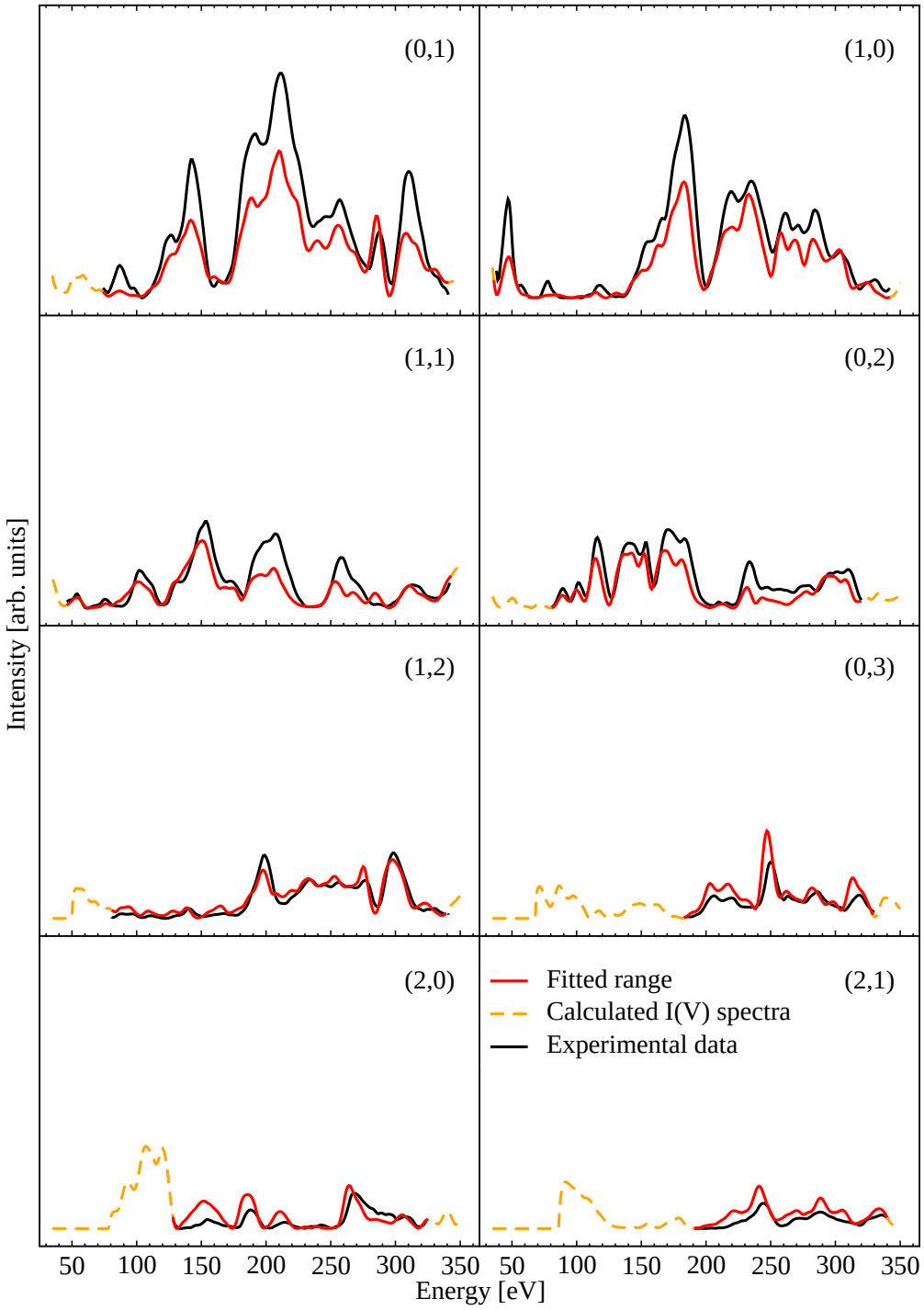

Figure 5.10: LEED-I,V spectra for the optimised closed Cu(1×1) bilayer.

The search program in the TensErLEED package simultaneously optimises all the variational parameters. Ultimately, this yields a structure with the lowest Pendry R-factor value. In Figure 5.10, we show the corresponding LEED I,V spectra for the Cu(1×1) structure, which was optimised leading to an improved R-factor value of $R_P = 0.22$. This included optimisation of the real part of the inner potential V_{0r} as a function of electron energy, see Figure 5.11.

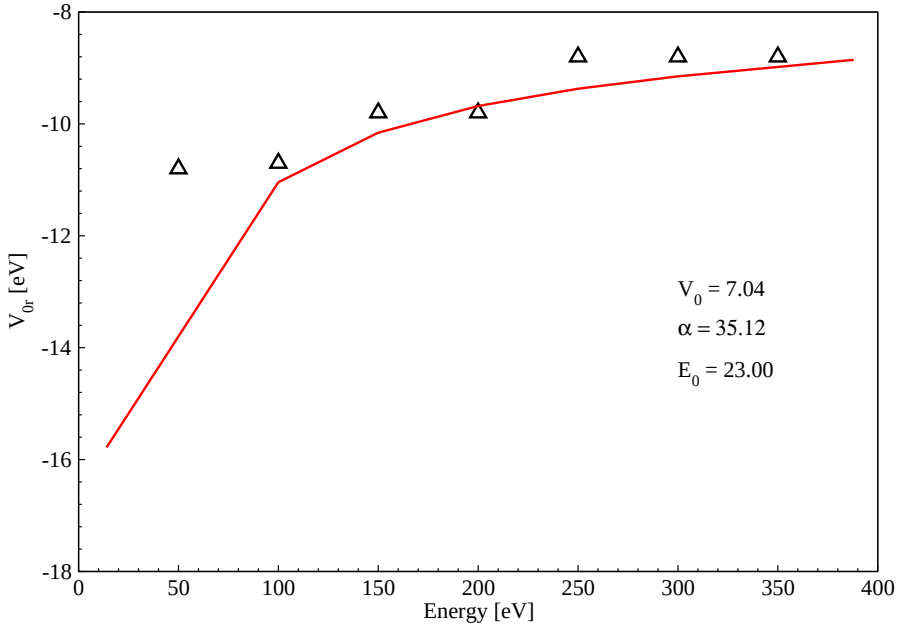

Figure 5.11: Optimisation of the energy-dependent inner potential for the Cu bilayer. $V_{0r}(E)$ was calculated within selected energy intervals of $50\,eV$ according to the function $V_{0r} = \left(V_0 + \frac{\alpha}{\sqrt{E-E_0}}\right)\,eV$ with fit parameters $\alpha = -35.12$, $V_0 = -7.04\,eV$, and $E_0 = 23.00\,eV$. In this way the R_P-factor could be improved by $\triangle R_P = -0.03$ leading to $R_P = 0.22$.

TensErLEED calculations show that copper grows hcp-wise, displaying for the two top layers a Cu-Cu interlayer distance[9] $d_{12} = 0.593(\pm0.001)$ Å, which is by 16% smaller than the relaxation that the topmost layer presents in the Re bulk (reference value taken 0.709 Å as re-calculated in this work for the clean Re surface, Table 5.1 on page 59). The distance between the topmost and the second Cu layer is thus $Cu^{(1)} - Cu^{(2)} = 2.687(\pm0.001)$ Å.

[9]Interlayer distances are presented with an accuracy up to 0.1%. As far as (1×1)-symmetry structures are concerned, the TensErLEED programme provides a discrete set of values leading to the lowest R_P-factor. The task gets harder with system complexity.

The Cu adlayer exhibits an additional contraction of 0.9% in comparison to the $Re^{(2)}$-$Re^{(3)}$ interlayer spacing in the Re bulk, $1.578(\pm 0.001)$ Å, with a resultant distance $Cu^{(2)} - Re^{(3)} = 2.722(\pm 0.001)$ Å (The $Re^{(2)}$-$Re^{(3)}$ distance in the clean surface being 2.730 Å).

Interlayer distances	Reference value [Å]	Best fit value [Å]
d_{12}	0.692	0.593
d_{23}	1.566	1.564
d_{34}	0.809	0.762
d_{bulk}	1.594	1.569

Table 5.4: Optimised interlayer distances for the Cu(1×1) structure.

Furthermore, LEED calculations reveal a contraction of the Re-Re interlayer spacing, with $d_{34} = 0.762(\pm 0.001)$ Å. Considering that in the clean state a Re($10\bar{1}0$) surface exhibits about 2% contraction of the third interlayer spacing (re-calculated value for the clean Re surface $d_{34} = 0.781$ Å), we see that the Cu adsorption causes this spacing to contract by 2.4%, the variation of the Re-Re distance is in this case negligible ($Re^{(3)} - Re^{(4)} = 2.735(\pm 0.001)$ Å). It should be pointed out that the contraction effect spreads till the 5^{th} layer in Figure 5.9 on page 72, since the so-called interlayer spacing between our slab and the bulk, d_{bulk}, commonly kept constant in the fit procedure, was also considered as a fitting parameter. The minimum value for the *R*-factor was achieved for $d_{bulk} = 1.569(\pm 0.001)$ Å which illustrates another contraction of about 1.5% of the Re bulk value, and the contraction of the distance from the bulk value $Re^{(4)} - Re^{(5)} = 2.739$ Å to $2.725(\pm 0.001)$ Å.

Therm. vib. amplitude	Reference value [Å]	Best fit value [Å]
ν_1(Cu)	0.18	0.12
ν_2(Cu)	0.12	0.10
ν_3(Re)	0.07	0.08
ν_4(Re)	0.06	0.04

Table 5.5: Characteristic thermal vibrational amplitudes for the Cu(1×1) phase.

In Table 5.5, optimised thermal vibrational amplitudes are given, which correspond to the overall isotropic thermal displacement $< \upsilon_i >$, previously defined in section 4.2.3.

These amplitudes were fitted for the mentioned chemical sites. According to the Van Hove interpolation method, the Debye temperature, Θ_D, for the top Cu layer was calculated to be around $480(\pm 48)\,K$ and for the Cu layers beneath $\Theta_D = 580(\pm 78)\,K$. The error margin, for instance for the Cu topmost layer, is defined as:

$$\Delta(\Theta_D) = \frac{|\Theta_D(v_1^{Cu}) - \Theta_D(v_1^{Cu} + 0.01\,\text{Å})| + |\Theta_D(v_1^{Cu}) - \Theta_D(v_1^{Cu} - 0.01\,\text{Å})|}{2}.$$

Note that the Debye temperature strongly depends on the RMS displacement $< v_i^2 >$. As already mentioned, a shift of ± 0.01 Å in the Cu topmost layer would lead to an averaged difference in Θ_D of $\pm 48\,K$[10]. In fact, it is delicate to draw conclusions about thermal vibrations from such results, because the treatment of thermal vibrations in the multiple-scattering theory is inadequate mainly due to the negligence of correlations in the vibrations between atoms. The thermal displacement of the Re top layer (#3) corresponds to a Debye temperature, $\Theta_D = 815(95\pm)\,K$, which is, up to $\pm 4\%$, comparable to Θ_D(Re) values found in the literature [34, 40].

5.2.2.2 Copper Multilayers with Coverages $\Theta_{Cu} > 1\,BL$

The MEED data mentioned in paragraph 5.2.1.3 and also the rise of the diffuse LEED background beyond $\Theta_{Cu} = 2\,ML$ suggests that the growing Cu film exhibits a fair amount of atomic roughness for coverages larger than the single bilayer. In terms of film growth mode this means that a stacking of incomplete, rough Cu islands (likely consisting of bilayer arrays) occurs, at least under the conditions of our (standard) Cu deposition between between 650 and $800\,K$ surface temperature, and we can clearly address the respective film growth as of the Stranski-Krastanov type. Since the (1×1) LEED pattern is dominated by the dimensions of the Re host lattice up to the deposition of more than 4 Cu bilayers we conclude on the formation of "hcp" copper at least up to this film thickness. Thereby, it is not unreasonable to grow hcp instead of fcc copper by an appropriate choice of a host lattice for epitaxy. In this respect, *e.g.,* Wormeester et al. succeeded in growing hcp-copper on a bcc-oriented W(100) surface [63].

A qualitative TensErLEED analysis was performed on the experimental LEED-I,V curves measured for coverages $\Theta_{Cu} = 1.5$, 2, and $2.5\,BL$. Assuming that Cu continues to grow hcp-wise, two possibilities should be considered: First, one could think

[10] For Pt(111), *e.g.*, a change of as much as $60\,K$ in the Debye temperature has no effect on its structure on the scale of $0.02\,$Å [53].

of a growth type that assembles individual Cu monolayers regardless of the fact that "B" terminations are energetically unfavourable. This would lead to alternating A-B-A-B terminations and, hence, to periodic fluctuations of the surface corrugation. The other possibility is that the growth occurs strictly bilayer-wise, with the exclusive "A"-termination and no periodic fluctuations in the corrugation.

Coverage Equivalent to $1.5\,BL$

Two possible hypotheses were considered in the LEED analysis of experimental I,V curves measured for the Cu coverage $\Theta_{Cu} = 1.5\,BL$. First, a homogeneous "B"-terminated structure was assumed, which consists of a 5 layers slab (2 Re-layers + 3 Cu-layers), growing on the Re bulk in a similar arrangement as for the closed bilayer. The input parameters in the reference structure were chosen similar to those found for the bilayer (*cf.* Table 5.4). This structure was optimised and converged to an $R_P = 0.44$. On the other hand, we have optimised the structure resulting from a random combination of two pseudomorphic domains, one with a *local* coverage of $1\,BL$ covering about 40% and the other with a *local* coverage of $2\,BL$ covering about 60% of the surface, which led to $R_P = 0.25$.

An improvement of 43% in the R_P-factor is already a very good indicator of a predominantly bilayer-wise Cu growth mode. Additionally, a qualitative visualisation of the LEED-I,V curves in Figure 5.12 confirms that the possibility of a layer-by-layer growth mode can definitely be ruled out, since a clear discrepancy can be observed at around $E = 225\,eV$ in the (1,1) beam as well as at $E = 210\,eV$ in the (0,1) beam. Moreover, the coverage relation (60 : 40) mentioned above, supports the MEED observations, which revealed a less smooth surface for just this coverage range between 1 and $2\,BL$ and did not show an additional peak for Cu coverages beyond the closed bilayer, see Figure 5.6. A peak of this kind has been found, *e.g.*, for Au and Ag grown on the Re($10\bar{1}0$) surface. The theoretically optimised structure leads to an acceptable increase of 5.9% in the Cu coverage compared to the *global* (integral) coverage $\Theta_{Cu} = 1.6\,BL$, which is within the experimental error margin[11] of $\pm 10\%$.

[11] Przyrembel's experimental Cu coverage is given with an uncertainty of $\pm 7\%$ for the closed bilayer. The experimental error margin is assessed to be of $\pm 10\%$ with increasing coverages, *i.e.* for $1.5 - 2.5\,BL$

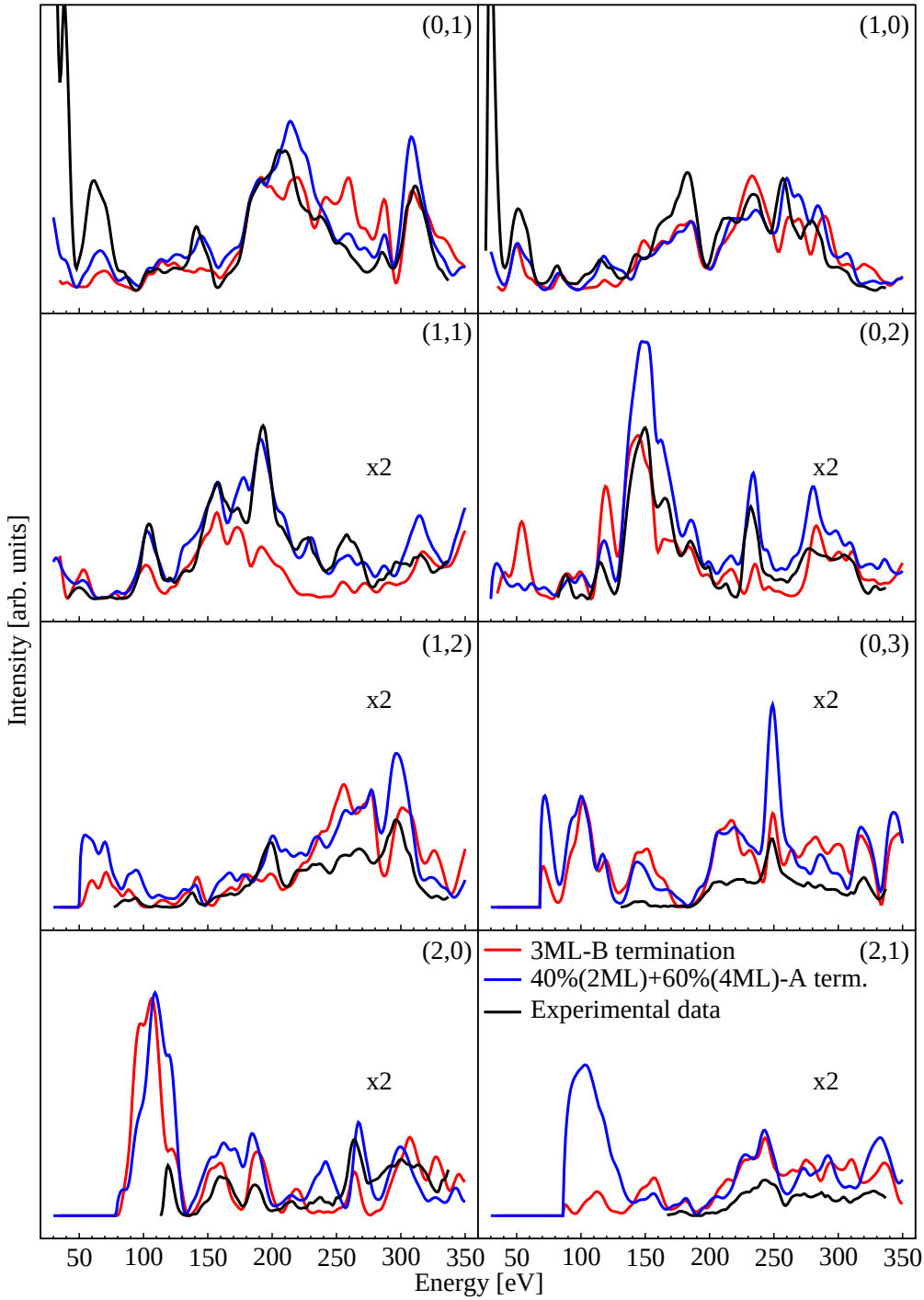

Figure 5.12: LEED-I,V spectra for the Cu(1×1) phase with $\Theta_{Cu} = 1.5\,BL$.

The best fit for the present combination led for the bilayer covered part to geometrical displacements similar[12] to those found for the complete Cu bilayer. The remaining 60% with $\Theta_{Cu} = 2\,BL$ consist of Cu islands with an B-A-B-A sequence. We have estimated the interlayer spacing between the two top Cu layers, $Cu^{(1)}$-$Cu^{(2)}$ as $0.45(\pm 0.02)$ Å. This represents a $\sim 25\%$ increased contraction of the topmost Cu layer compared to the complete bilayer. The Cu bilayer underneath is separated by $1.51(\pm 0.02)$ Å, which is by 3% smaller than the interlayer spacing between the Cu slab and the Re slab found for the closed bilayer phase, which shows that the compression of the Cu layers varies with the number of the adsorbed Cu layers.

Coverages Equivalent to $2\,BL$

The same procedure was followed for the determination of the Cu(1×1) structure observed for $\Theta_{Cu} = 2\,BL$. The B-A-B-A sequenced surface was optimised by TensErLEED. The LEED-I,V spectra presented in Figure 5.13 show in overall a good agreement between the experimental curves and the fitted ones and convergence was reached with $R_P = 0.30$. The peak profiles are in fact well reproduced but are accompanied by a loss in the intensity for higher order beams. This R_P value is somewhat higher than that of the optimised Cu(1×1) phase with $1.5\,BL$ ($R_P = 0.25$). This degradation apparently indicates the increasing roughness and admixture of structural motifs stemming from incomplete Cu layers. This is in the line with the MEED data.

The best fit obtained by the LEED quantitative analysis of Cu(1×1) phase with $\Theta_{Cu} = 2\,BL$, provides us especially with information about interlayer spacings, although the data obtained are not of the same reliability as those found for the closed bilayer. Anyway, the $Cu^{(1)}$-$Cu^{(2)}$ interlayer distance is found to be $0.47(\pm 0.02)$ Å. This value (20% of the Cu-Cu relaxation in the closed bilayer) is in good agreement with the 24% relaxation calculated for the $2\,BL$ coexisting domain in the Cu(1×1) phase with $1.5\,BL$. The $Cu^{(2)}$-$Cu^{(3)}$ interlayer distance was determined as $1.51(0.02\pm)$ Å, similar to the value of 1.53 Å found for the same structure in the $1.5\,BL$ phase.

[12] Variations of ± 0.01 Å in the interlayer spacings are totally reasonable, as the fit procedure for the $1.5\,BL$ structure consists in the simultaneous optimisation of 18 independent parameters.

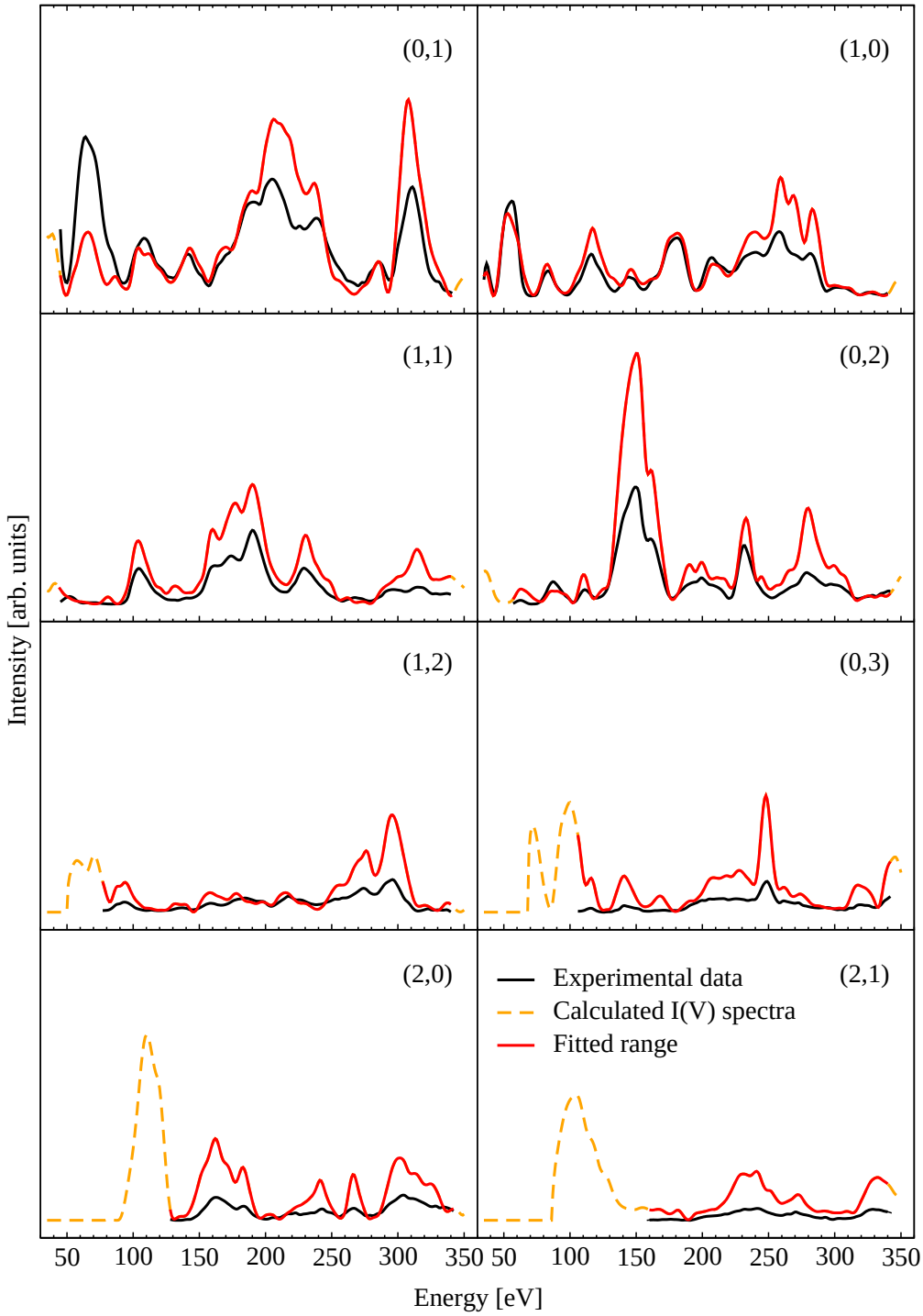

Figure 5.13: LEED-I,V spectra for the Cu(1×1) phase with $\Theta_{exp} = 2\,BL$.

Coverages Equivalent to $2.5\,BL$

We recall that the LEED pattern of the Cu(1×1) phase is still observed upon further Cu deposition to coverages of $\sim 2.5\,BL$. Analogous to what has been done for $\Theta_{Cu} = 1.5\,ML$, the "B"-terminated structure (with a B-A-B-A-B) was investigated by TensErLEED and, in parallel, a superposition of the combination of the "A"-terminated structures with $2\,BL$ and $3\,BL$, respectively, was tested.

From Figure 5.14 it is evident that the LEED-I,V spectra are less well reproduced than those of structures with lower coverages. Nevertheless, a major discrepancy that appears in the (0,1) beam at $E = 110\,eV$ and many in the (1,0) beam clearly rule out the possibility of "B"-terminated (1×1) structures. The optimisation of both possibilities also yields different R_P-factors: 0.48 for the "B" termination with exactly $2.5\,BL$, and $R_P = 0.33$ for the combination of 70% of $2\,BL$ and 30% of $3\,BL$. The coverage following from the LEED calculation is thus by 6.1% lower than the one experimentally determined, which is still within the experimental error margin of 10%. If now, as a reasonable approximation, the integral surface is assumed as a superposition of $\sim 70\%$ of $\Theta_{Cu} = 2\,BL$ and 30% of $\Theta_{Cu} = 3\,BL$, this leads to a $Cu^{(1)}$-$Cu^{(2)}$ interlayer spacing of 0.46 (±0.02) Å between the topmost Cu layers of the $2\,BL$ coverage domain. We can thus conclude that three different quantitative LEED analyses lead to a consistent value of $0.46(\pm0.02)$Å, suggesting a shortened Cu-Cu distance of about $2.66(\pm0.02)$ Å in this position. The interlayer spacing between the second and third layer $Cu^{(2)}$-$Cu^{(3)}$ was found to be $1.53(\pm0.02)$ Å, also consistent with the values found for lower coverages, which we can average to $1.52(\pm(0.02)$ Å. This in turn corresponds to a $Cu^{(2)}$-$Cu^{(3)}$ distance shortening of about $2.70(\pm0.02)$ Å. The slight compression ($\sim 20\%$) found within these Cu layers (which comprise at least up to four adsorbed monolayers) is in fact not a calculational coincidence, but rather represents a physical phenomenon that we try to assess somewhat more below. Concerning the remaining surface with $\Theta_{Cu} = 3\,BL$, we consider that a distribution of 30% is not substantial enough to assess the interlayer spacings with certainty. At this stage, Cu atoms seem to grow in distinguished islands, which are, however, not extended enough to give credible account of the interlayer distances beyond four adsorbed Cu monolayers.

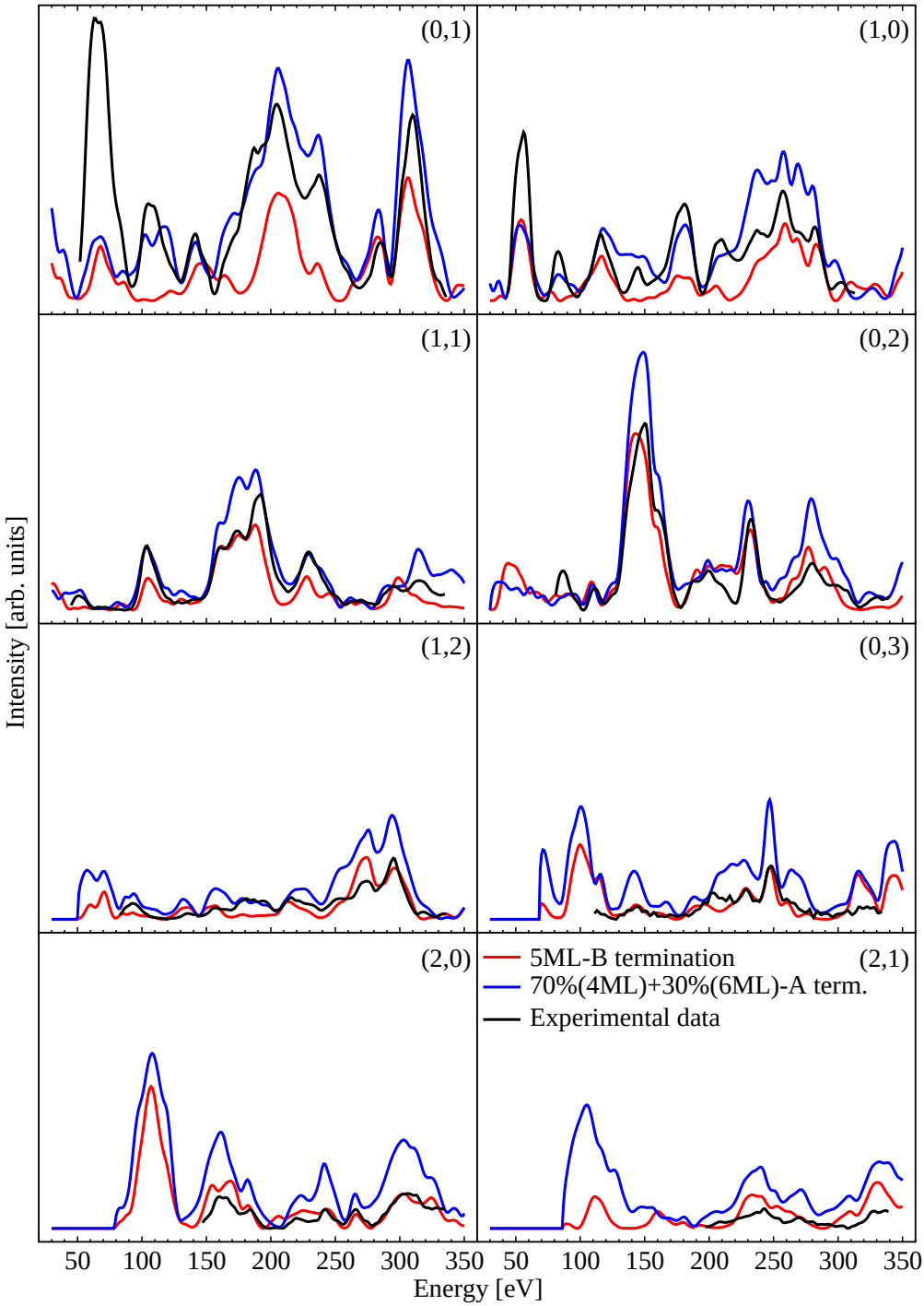

Figure 5.14: LEED-I,V spectra for the Cu(1×1) phase with $\Theta_{exp} = 2.5\,BL$.

Synopsis

In the light of these results, we can deduce that copper forms hcp islands, which, however, appear to be somewhat more squeezed in z-direction than the layers of an "ideal" copper hcp crystal would be, see Figure 5.15. Indeed, we have attempted to calculate the lattice parameter, c, of such a crystal (for Re, $c_{Re} = 4.456\,\text{Å}$) based on the fact that in an ideal hcp crystal the ratio $\frac{c}{a} = \sqrt{\frac{8}{3}} \backsimeq 1.633$, this leads to $c_{Cu} = 4.17\,\text{Å}$. The resulting $Cu^{(1)}$-$Cu^{(2)}$ first interlayer spacing is $\sim 0.74\,\text{Å}$ and the second one, $Cu^{(2)}$-$Cu^{(3)}$, thus is $\sim 1.47\,\text{Å}$. We notice that in reality the Cu-Cu hcp short spacing (0.46 Å in the $2\,BL$) is approximately 37% smaller than that of an ideal Cu hcp crystal, whereas the long spacing, averaged to $1.52(\pm 0.02)\,\text{Å}$, is more or less in the range of the ideal crystal value. Copper therefore doesn't produce its own hcp crystal when it grows on the Re(10$\bar{1}$0) surface, the Cu-Cu interplay seems to hamper the creation of a genuine Cu hcp crystal supported by the Re host surface. Neither does copper retrieve its natural fcc configuration. We recall that the fcc(110) facet morphologically resembles the hcp(10$\bar{1}$0) one, but with equal interlayer spacing, which is nothing other than the copper radius itself, 1.278 Å.

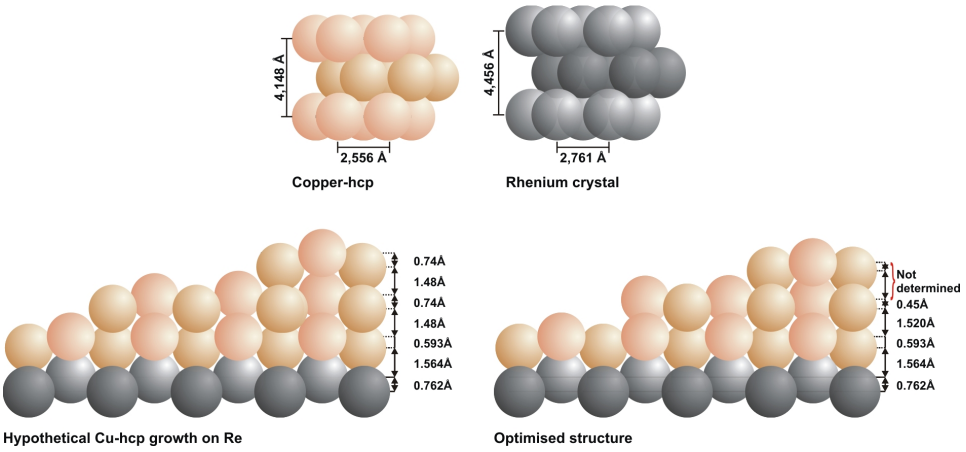

Figure 5.15: Comparison between ideal and real, experimentally found hcp Cu.

To summarise, we present in Figure 5.16 a schematic view of the growth sequence of Cu atoms on the clean Re(10$\bar{1}$0) surface. As expected, since Cu atoms are by $\sim 7\%$ smaller than the Re host substrate atoms and *a priori* no compression forces have to act on the Cu atoms, Cu grows pseudomorphically and, as shown, approximately bilayer-wise. Furthermore, there is no reason for any Cu-induced strain on the Re surface, as the cohesive energies of Cu and Re differ substantially (338 and $782\,kJ/mol$, respectively),

and a formation of extended Cu bulk clusters on top of the Re surface could not put much strain on the Re surface region. On the other hand, the surface free energies of the two metals are relatively similar ($3.60\,J/m^2$ for Re [59] and $1.56\,J/m^2$ for Cu [50]), and one rather expects pronounced wetting of the Re surface by Cu. As our data show, this is indeed what occurs. Along with the attractive Cu-Cu interactions, small $2D$ Cu bilayer aggregates nucleate and coalesce, with increasing surface concentration, to more or less extended $2D$ Cu bilayer islands. Note that in the multilayer range, a higher layer starts forming before the lower is completed as can be deduced from the MEED observations. From the LEED (1×1) pattern observed for all submonolayer coverages and the round spot profile (within our experimental LEED resolution) we deduce that in $x-y$ direction (parallel to the surface) these islands exhibit the same local geometry as the underlying Re substrate, whereas in z direction, *i.e.* perpendicular to the surface, the Cu-Cu layer distance is essentially somewhat smaller than the respective Re-Re layer distance.

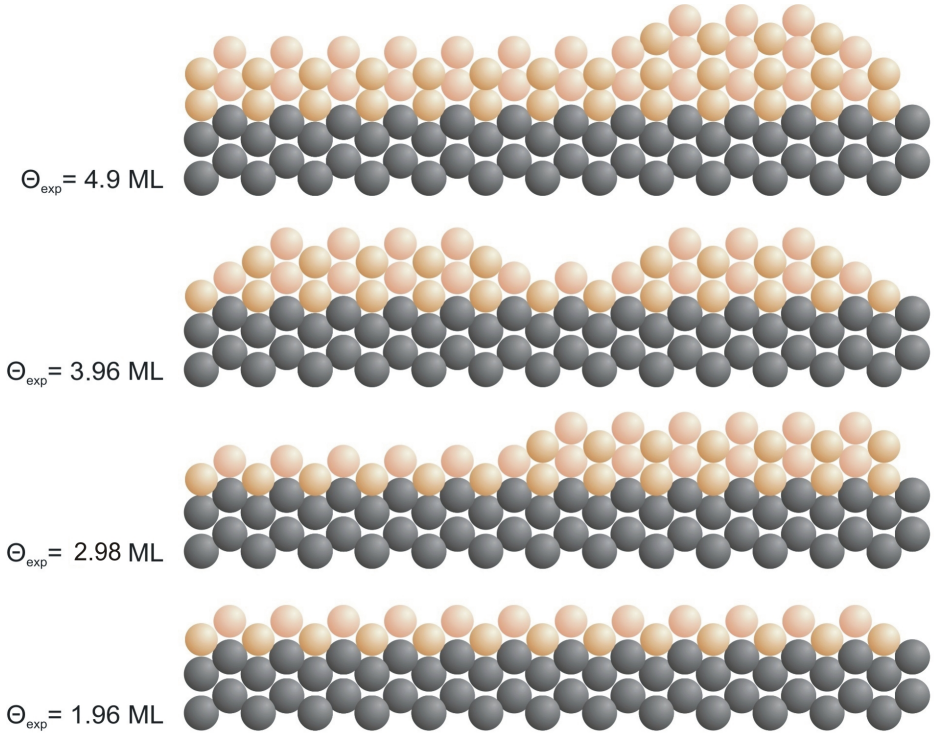

Figure 5.16: Stranski-Krastanov growth sequence of Cu on the Re(10$\bar{1}$0) surface. The coverages are given in monolayers, $1\,BL = 2\,ML$. These values correspond to the *global* coverage measured experimentally by Przyrembel [39].

5.3 Silver Adsorption on Rhenium($10\bar{1}0$)

Silver film epitaxy has been the subject of several studies, and particularly in our group, Ag adsorption on ruthenium and rhenium($10\bar{1}0$) and (0001) surfaces has widely been investigated [27, 32, 45, 57, 58, 44]. The compilation of the respective results is of great interest in order to understand, among others, the mechanism that makes silver form on the Re($10\bar{1}0$) surface the two well-ordered (1×4) and c(2×2) phases in the sub-bilayer range, accompanied by the peculiar reversible temperature-driven transition of the (1×4) phase to the c(2×2) phase first reported by Vollmer [57].

In the following, we will focus on a quantitative structural analysis of LEED-I,V data that have recently been measured by Scherf in the context of his Ph.D. thesis [44]. In order to better understand the Ag/Re($10\bar{1}0$) system, we will start by giving a brief overview of his main experimental findings concerning coverage-dependent LEED and MEED phases, thermal desorption spectra and binding states.

5.3.1 Experimental Results

5.3.1.1 LEED

The structure and morphology of Ag films has been studied for coverages Θ_{Ag} ranging between 0.18 and $14\,ML$ in the temperature interval $120 \leq T \leq 700\,K$. A series of coverage-dependent LEED measurements was carried out, in which Θ_{Ag} was continuously increased. Generally, the Ag deposition was performed at $700\,K$ in order to give the Ag atoms sufficient mobility to form ordered phases. After the deposition (with an upper coverage limit of *ca.* $14\,ML$) the sample was allowed to cool to $300\,K$ before the LEED spectra were recorded.

Similarly to Vollmer's observations, Scherf, too, detected and verified two ordered Ag phases, which were both coverage and temperature dependent, namely a (1×4) phase that appears in the temperature range between RT and $640\,K$, and a c(2×2) phase that was only detectable beyond *ca.* $500K$. In an extended series of Θ- and T-dependent LEED measurements Scherf succeeded in narrowing down the borders of existence of both phases in a $T(\Theta)$ diagram. In brief, the (1×4) phase is stable between $120\,K$ and $600\,K$, whereas the c(2×2) phase exists between $\sim 450\,K$ and $700\,K$. A third phase occurring at somewhat larger coverages is a (1×1) Ag phase associated with a coverage of $2\,ML = 1$ bilayer (*BL*) and reflecting pseudomorphic (hcp-like) growth.

To somewhat summarise Scherf's conclusions on the existence of the three phases

we can state that the LEED "extra" intensity of the (1×4) phase is highest around $\Theta_{Ag} = 1.5\,ML$ and that of the c(2×2) phase at somewhat lower coverages, *i.e.*, around $1.34\,ML$. It has to be mentioned here that the c(2×2) phase could not be observed at coverages beyond $1.5\,ML$. As pointed out in his thesis [44], the precision of the coverage data suffers somewhat from the fact that both LEED and TPD do not allow to distinguish between the *global* and the *local* Ag coverage, which may differ substantially, depending on the temperature and annealing history.

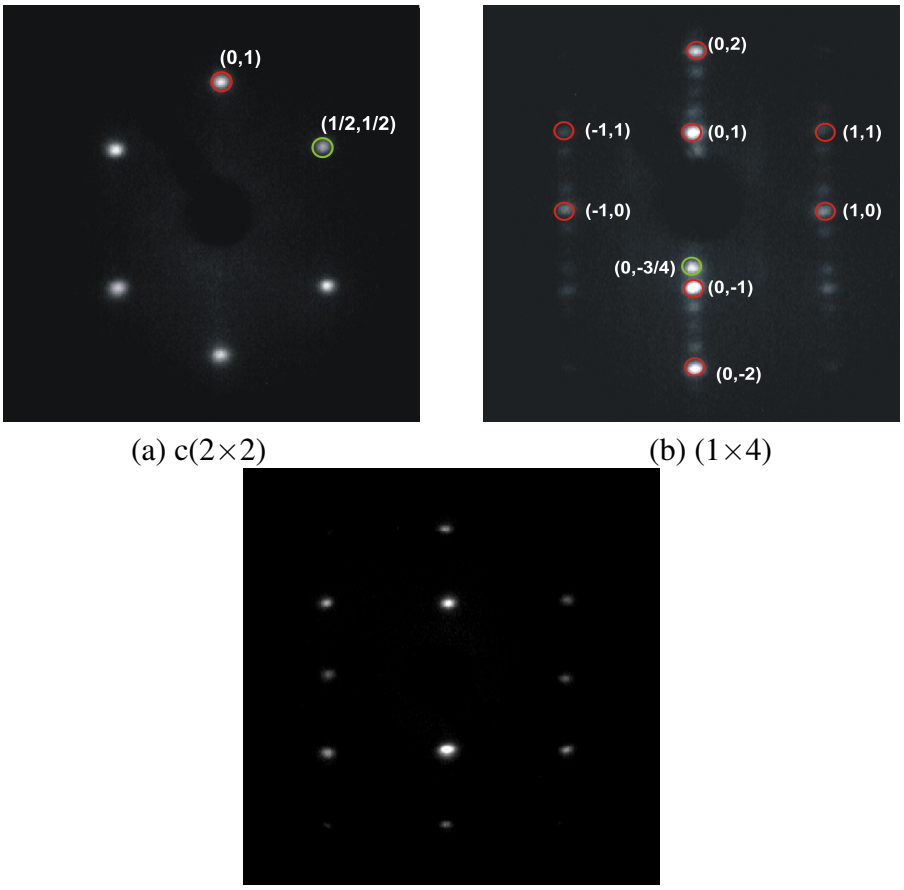

(a) c(2×2) (b) (1×4)

(c) (1×1)

Figure 5.17: Ag/Re(10$\bar{1}$0) (n×m)-LEED patterns.

The shown (n×m) LEED patterns are observed in the coverage range $\Theta_{Ag} \leq 2\,ML$. The respective LEED images were taken at (a) $T = 600\,K$ and $E_e = 22\,eV$; (b) at $T = 120\,K$ and $E_e = 112.1\,eV$; and (c) at $T = 120\,K$ and $E_e = 77.3\,eV$.

5.3.1.2 MEED

As already mentioned, the epitactic growth of vapour-deposited Ag on the Re($10\bar{1}0$) surface was controlled *in-situ* by MEED up to a film thickness of $14\,ML$ by monitoring the (0,0)-beam intensity at $700\,K$. For surface coverages $\Theta_{Ag} \leq 2\,ML$ the MEED intensity oscillates strongly with coverage and shows, according to a varying surface roughness, pronounced minima and maxima, see Figure 5.18.

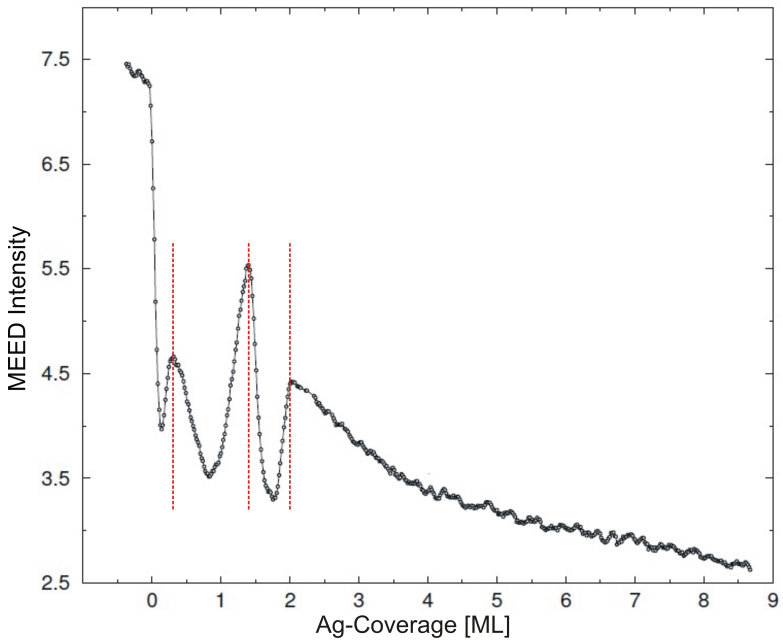

Figure 5.18: Ag/Re($10\bar{1}0$) MEED (0,0) intensity as a function of Ag coverage.
All MEED measurements were performed at $700\,K$ with an electron energy, $E_{el} = 5\,keV$, and a grazing angle of 2° [44].

In our MEED experiment, the experimental conditions were adjusted such that the surface simply acted as a mirror of the MEED electrons and, hence, sensitively recorded the surface roughness of the sample. Accordingly, the amplitude of the MEED signal strongly depends on the adatoms' mobility, in other words, on the surface temperature. Indeed, Scherf performed a T-dependent series of silver vapour-deposition showing that even a temperature of $550\,K$ is not sufficient to ensure enough mobility and ordering as can be deduced from the largely absent MEED oscillations. These oscillations only occur at temperatures beyond $\sim 650\,K$ and are especially pronounced at $700\,K$ (see Figure 5.18). In the sub-bilayer range, a first maximum develops at *ca.* $0.25\,ML$ almost linearly with Ag coverage. This follows a strong decay until a second sharp maximum

appears at $\sim 1.34\,ML$, before the intensity steeply falls again to reach a minimum at $\sim 1.55\,ML$. Note that only a coverage increment of $\Delta\Theta = 0.18\,ML$ is necessary to pass over from the sharp maximum to this minimum! A third maximum is then, as expected, reached at $\sim 2\,ML$, when the comparatively smooth bilayer is formed. Continuing Ag deposition then causes a monotonous decrease of the MEED intensity up to $\Theta_{Ag} \approx 4\,ML$, where an incommensurable (1×10) LEED structure appears indicating a relaxation of the Ag film in [0001] direction (for further details, see [44]). This behaviour clearly points to an incomplete multilayer growth that provides a steady amount of surface roughness.

5.3.1.3 TPD

Some of the typical Ag thermal desorption spectra measured by Scherf are shown in Figure 5.19, depicting the two desorption states α and β. The α state is characteristic of multilayer growth, *i.e.*, for $\Theta_{Ag} \geq 2\,ML$, and the β-state is associated with Ag desorption from the first bilayer coverage range. Concerning the β state desorption maximum, we observe a systematic shift towards higher temperatures with the Ag coverage ($0.1 \leq \Theta_{Ag} \leq 2\,ML$); at $\Theta = 2\,ML$ it appears at $1055\,K$.

A closer look at the spectra containing the β state in the lower coverage regime (drawn in red) reveals the formation of a shoulder around $925\,K$ and for a coverage of $\sim 1.5\,ML$. This shoulder already appears long before the β state has reached its maximum at $2\,ML$, thus indicating an incomplete growth mode as discussed further below.

The quantitative evaluation of thermal desorption of silver follows a complicated fractional-order kinetics [44]. The energy of desorption for the first Ag monolayer is $\triangle E_{des} = 302\,kJ/mol$. Between $1-2\,ML$ the desorption energy drops from 250 to $140\,kJ/mol$, but it continuously increases along the coverage until $210\,kJ/mol$ at $\Theta_{Ag} \approx 2\,ML$, while for $\Theta_{Ag} \approx 2.5\,ML$ $\triangle E_{des}$ reaches $258\,kJ/mol$, which is almost identical with the sublimation enthalpy of bulk silver ($\triangle H_{sub}(Ag) = 266\,kJ/mol$).

Up to $1\,ML$, the lateral attraction forces between Ag atoms seem to dominate the growth process, causing the shift of the β-maximum towards higher T. This is established by the fact that the desorption itself is preceded by an equilibrium in which condensed $2D$ Ag islands and a $2D$ Ag gas phase coexist. From $1.5\,ML$ on the growth mode changes in favour of a three-dimensional Ag aggregation. In fact, although the first Ag bilayer is not yet homogeneously completed and free Re adsorption sites are still available, Ag atoms already begin to form the second bilayer. This is known as simultaneous-

multilayer growth mode (SM). The deposition of silver up to 10ML causes the intensity of the α-state to continuously increase. Ag atoms, admittedly, agglomerate in this region and form a 3D-bulk phase as corroborated by the surface roughness suggested by the MEED intensity decrease [57, 44].

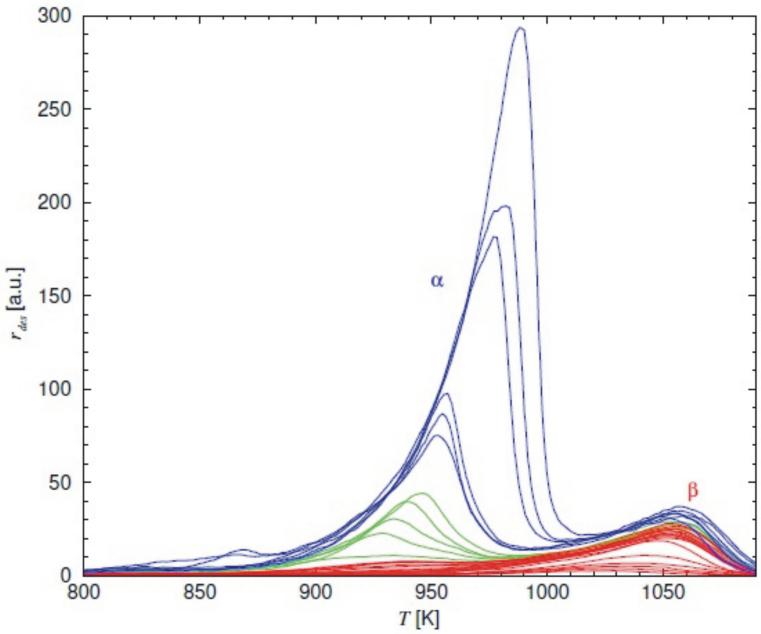

Figure 5.19: TPD spectra for the Ag/Re system.
Series of TPD measurements at a heating speed $\beta = 3\,K/s$. The colours distinguish three coverage ranges: $\Theta_{Ag} \leq 2\,ML$ (red), $2-4\,ML$ (green), and $4-10\,ML$ (blue).

5.3.2 LEED Structural Analysis

The purpose of the work reported in this part is to determine, by means of a quantitative LEED structural analysis, the location of Ag atoms chemisorbed on the Re(10$\bar{1}$0) surface. As we have seen in the experimental part, silver forms, depending on coverage and temperature, three phases, *i.e.*, a (1×4), a c(2×2), and a (pseudomorphic) (1×1) phase. Of special interest in this context is the structure of the first two phases c(2×2) and (1×4). Various structural models will be proposed for these phases. Based on the compilation of the experimental findings from LEED, MEED, and TPD, we will attempt to determine the true real-space Ag superstructures, also in view of a better understanding of the peculiar c(2×2)↔(1×4) phase transition.

5.3.2.1 The Sub-Bilayer Coverage Range

The Ag-c(2×2) Phase

The structural search for the Ag-c(2×2) surface was initialised with the models (A) - (F), as shown in Figure 5.20. The model (A) was tested on the basis of a model that Vollmer has previously proposed from her STM observations[13]. This structure with a relatively low *local* coverage of $\Theta_{Ag} = 0.5\,ML$, displays a single "B"-terminated Ag layer with the Ag atoms located on the long-bridge site formed by two Re atoms in the $[1\bar{2}10]$ direction.

It is to be mentioned that structure (F) resembles model (A) as far as the local symmetry is concerned. However, since the topmost Ag atoms lie on a lower Ag layer, the stable "A"-termination with a *local* coverage $\Theta_{Ag} = 1.5\,ML$ is recreated. These two models, (A) and (F), have a particular common feature in that they both exhibit a somewhat rigid topmost Ag layer that is constrained to relax only perpendicularly to the surface (especially at T around $600\,K$), as any deviation in x or y directions would immediately break the c(2×2)-symmetry. Structures (B) and (D) have in common that they consist of Ag-pairs, which are centred on the Re short-bridge site in structure (B), and centred on the 4-fold hollow site in structure (D). The overall structure looks, in this case, like a slightly distorded honeycomb that we choose to refer to as "empty honeycomb-like" structure in order to make the distinction with the models to follow. The corresponding coverage of models (B) and (D) is $\Theta_{Ag} = 1\,ML$. Structures (C) and (E) are the exact reproduction of structures (B) and (D), respectively, except that an additional Ag atom has been inserted in the centre of the hexagonal ring. The coverage of these structures therefore increases to $1.5\,ML$ and they are referred to as "filled honeycomb-like" structures.

For the LEED intensity calculations up to electron energies of $350\,eV$ the phase shifts were generated from the self-consistent potential calculated using the Barbieri-Van Hove program [2] with angular momentum quantum numbers up to $L = 12$. Electron attenuation was simulated by an imaginary part of the inner potential equal to a constant value of $V_{0i} = 5\,eV$. The real part of the inner potential, V_{0r}, was also kept constant and initially set equal to $11.8\,eV$. It was treated as an adjustable parameter in the calculation. A total of 9 (7 integer-order and 2 fractional-order) beams were considered.

[13] Note that for the present study only structures involving pseudomorphic adsorption sites were considered. In practise, the Ag-c(2×2) phase and the (1×4) phase, as well, were investigated after the determination of the (1×1) structure that leaves no other choice than the pseudomorphic site.

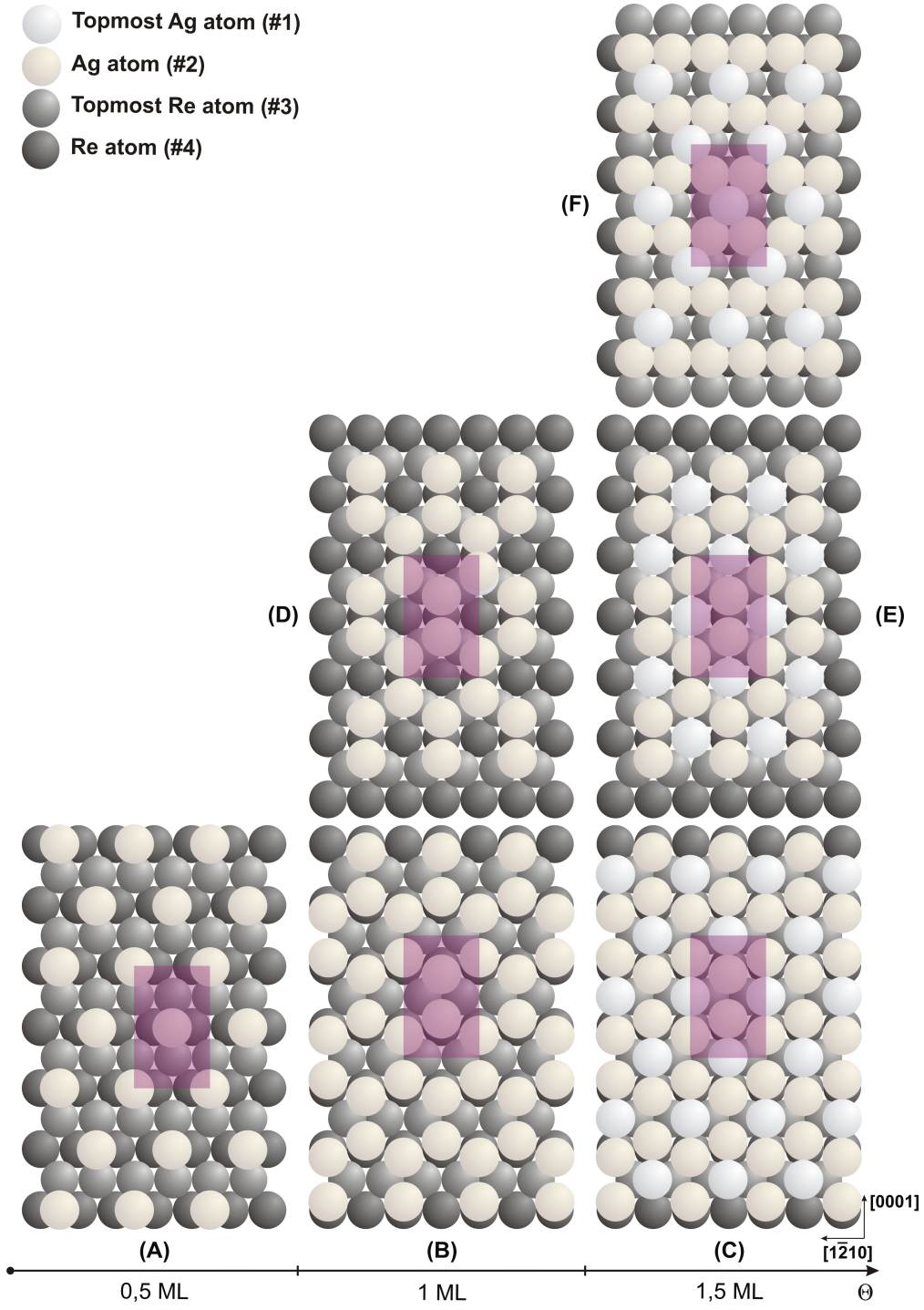

Figure 5.20: Ball-model representation of different tested Ag-c(2×2) structures.
The c(2×2) unit mesh is represented by the rectangles in purple. The denomination "honeycomb-like" is only associated to structures (B), (C), (D), and (E) due to the planar disposition of its 6 constituting Ag atoms. By analogy, structures (A) and (F) have a mere diamond pattern with vertical angles of only 58.22° and 31.78° due to the anisotropic character of the (10$\bar{1}$0) surface.

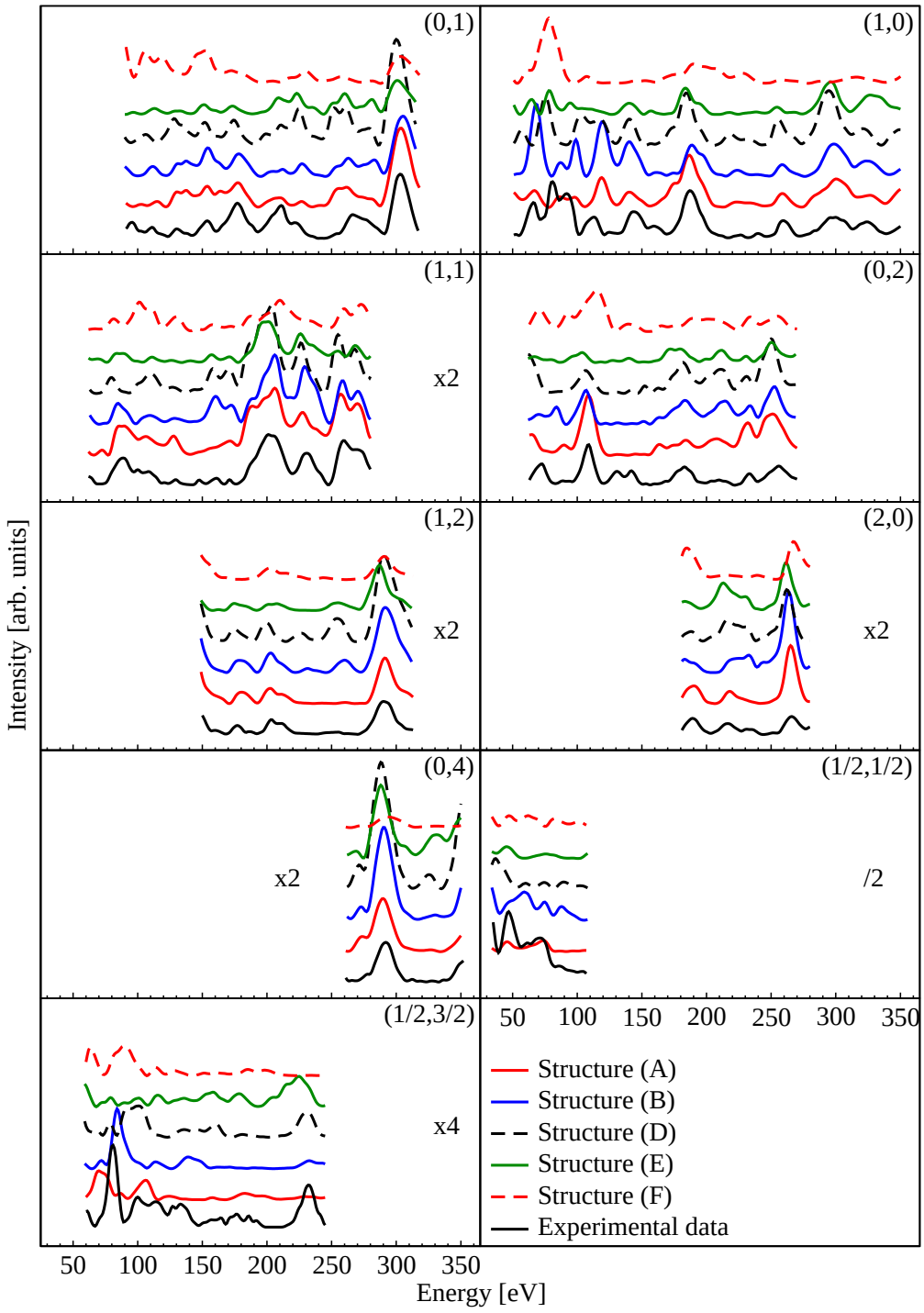

Figure 5.21: Comparison of calculated LEED-I,V spectra for the Ag-c(2×2) structure. Comparison of optimised LEED-I,V spectra for all tested Ag-c(2×2) structural models except structure (C), which is separately presented in Figure 5.22. For a better visualisation of the spectra, (A) spectra were incremented by 0.1, (B) by 0.2, (D) by 0.3, (E) by 0.4, and (F) spectra by 0.5. Here, the $(\frac{1}{2},\frac{1}{2})$ beam is of a particular interest since clearly none of the tested structures, characterised by a fairly low intensity, can reproduce the experimental spectrum. Structure (E) is the closest in terms of shape, with a Pendry R-factor, $R_{(\frac{1}{2},\frac{1}{2})} = 0.67$.

The initial reference calculation of the six models yielded the Pendry R-factors presented in Table 5.6. Each reference calculation consisted in the simultaneous variation of thermal vibrational amplitudes and a 3-directional geometrical variation of the Ag overlayer(s) as well as the two topmost layers of the truncated Re bulk. The same initial input parameters were implemented for each structure. The two lowest R_P-factors were found for structure (B) and (C). Given that for this cumulative energy range, $\triangle E = 1580$, the statistical error, $\triangle R = 0.62\sqrt{\frac{40}{1580}} = 0.1$, is relatively high and that the lowest R_P value is not low enough to rule out the five other possibilities, it was required to optimise all six structures. Indeed, at least one optimisation cycle had to be performed that reached convergence in order to make sure that none of the "wrong" structures would turn out to be better than the others, especially over a wide range of variational steps. Table 5.7 summarises the six optimised structures and their respective R_P-factor as well as the number of variation cycles required to attain convergence. We chose to show the LEED-I,V spectra relative to the five structures with $R_P > 0.32$ separately in Figure 5.21.

Reference structure	Coverage (ML)	R_P-factor
(A)	0.5	0.69
(B)	1.0	**0.62**
(C)	1.0	**0.66**
(D)	1.5	0.70
(E)	1.5	0.73
(F)	1.5	0.91

Table 5.6: Pendry R-factors calculated for the six tested Ag-c(2×2) models.

As already mentioned, determination of the atomic arrangement in the c(2×2) surface layer has been performed using the TensErLEED method. Several structural models have been examined but only one has been found to produce satisfactory agreement with experiment. In this model, (C) in Figure 5.20, the Ag superstructure can be depicted as a honeycomb-like structure (six $Ag^{(2)}$ atom ring) centred by a somewhat elevated $Ag^{(1)}$ atom located on the short-bridge site formed by two topmost Re atoms. This results in a *local* c(2×2) coverage of 1.5 ML.

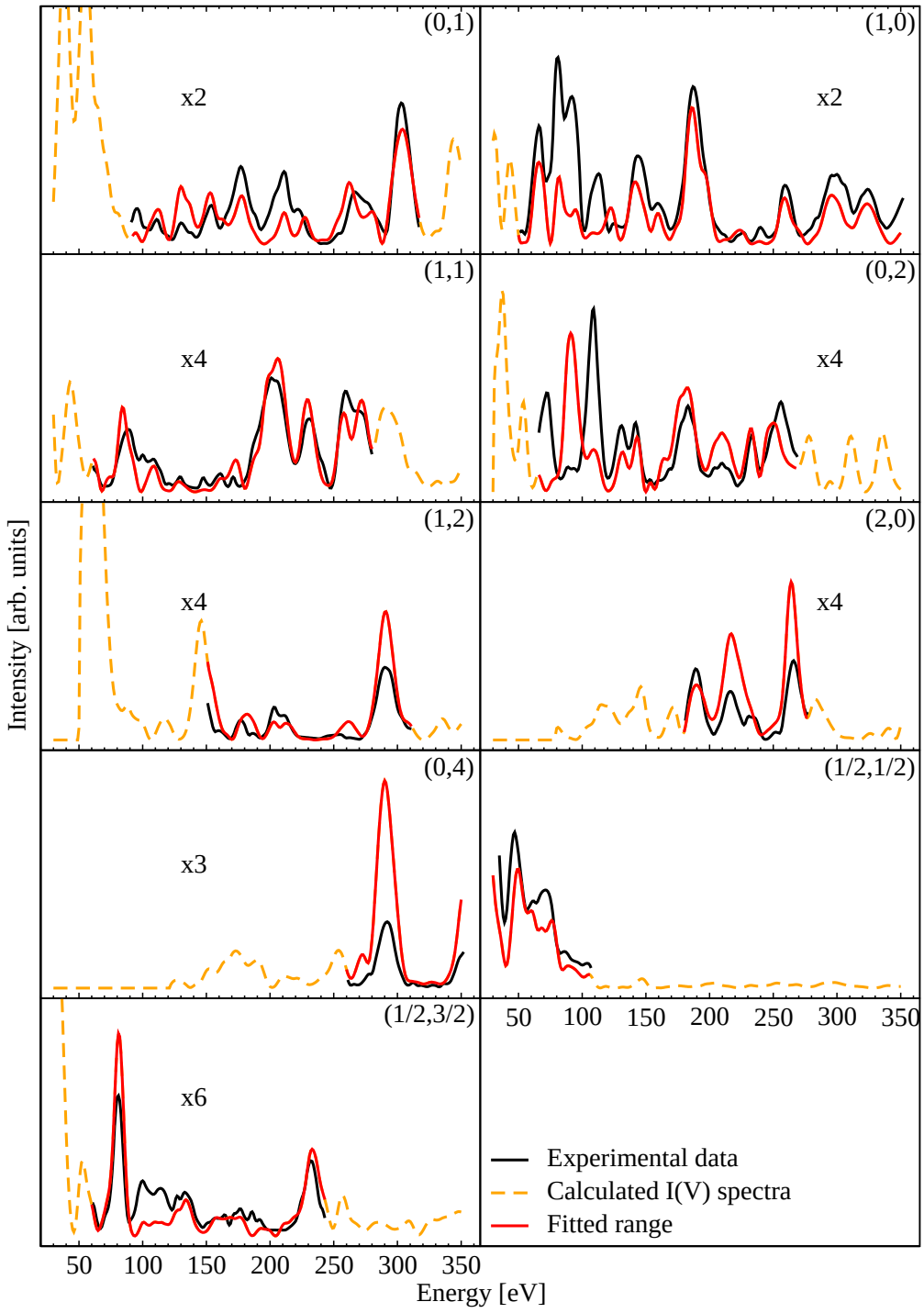

Figure 5.22: LEED-I,V best fit spectra for the Ag-c(2×2) structure (C).

Qualitatively, the $(\frac{1}{2},\frac{1}{2})$ fractional-order beam has been the strongest indicator as to why, among the six proposed models, structure (C) is indisputably the best structure. The $(\frac{1}{2},\frac{3}{2})$ beam is also reasonably well reproduced by (C), in that it is the only one reproducing both major peaks at $80\,eV$ and $230\,eV$. We estimate that the integer-order beams show in overall a good agreement ($R_{int} = 0.33$), the slight intensity discrepancies for $E < 130\,eV$ in (1,0) and (0,2) beams is not much influent since the corresponding peaks are in fact detected but with much lower intensities. We recall that the present data have been measured at $600\,K$, where thermal effects are expected to influence the experimental I,V data.

Reference structure	Optimisation cycles (#)	Best fit R_P-factor		
		Total R_P	Integ.- order	Fract.- order
(A)	19	0.40	0.30	0.73
(B)	24	0.45	0.37	0.71
(C)	53	**0.32**	0.33	0.30
(D)	24	0.46	0.40	0.68
(E)	24	0.48	0.44	0.63
(F)	22	0.65	0.60	0.84

Table 5.7: Comparison of the R_P-factors for the six optimised Ag-c(2×2) structures.

As one can see, structure (C) necessitated *ca.* twice *a*s much iterations as the five other candidates, but with an $R_P = 0.32$ and an error margin of 0.07, this structure clearly emerges as the most plausible one. Although in this case the resulting overall R_P-factor[14] is still relatively high, the R_P of just the two fractional-order beams, $(\frac{1}{2},\frac{1}{2})$ and $(\frac{1}{2},\frac{3}{2})$, clearly is only acceptable for structure (C). Note that only the fractional-order LEED spots originate from the Ag superstructure alone, whereas the integer-order beams contain a significant contribution from the Re substrate. Structure (C) exhibits by far the lowest $R_P = 0.30$ for the fractional-order beams, which in itself is a very strong argument for (C) to be the "right" structure. In the final LEED calculations, the real part of the potential was replaced by the energy-dependent function: $V_{0r} = 8.67 + \frac{10.52}{\sqrt{E-25}}$, while the initial value was taken $V_{0r} = 11.80\,eV$. The best fit obtained for structure (C), shown in Figure 5.22, yields an error on the R_P-factor of 0.05. As shown in Table 5.7, the next "best" structure is (A), whose R_P-factor is by 0.08 greater than that attained for structure (C). Therefore all the five tested models except (C) can be ruled out.

The analysis of LEED-I,V spectra is a multi-parameter problem in which all quantities of interest are determined in a simultaneous fit. And as all LEED-I,V data were recorded at high temperature ($\approx 600\,K$), we remind that the observed surface relaxation and thermal vibrational amplitudes correspond to thermal equilibrium around $600\,K$.

As already done for Cu, the Ag (and later Au) and Re atoms will be referred to as $\mathrm{Ag}^{(i)}$ and $\mathrm{Re}^{(i)}$, where i is the corresponding atom-label in Figure 5.23. For all models investigated, the interlayer distances, d_{ij}, and the interatomic spacings, a_{i-j}, were varied over a reasonably wide range.

[14] Agreement between theory and experiment is generally considered good for R_P below 0.3.

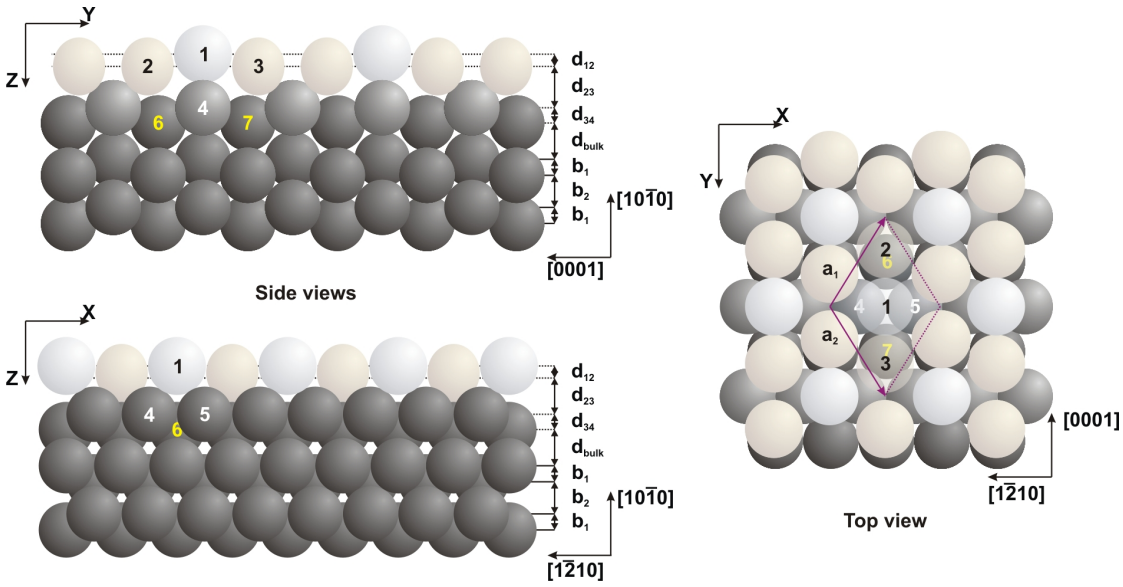

Figure 5.23: Geometrical displacements relative to the Ag-c(2×2) structure.
The diamond (in purple) represents the unit mesh used in the TensErLEED calculations to reproduce the c(2×2) pattern. $\overrightarrow{a_1}$ and $\overrightarrow{a_2}$ are the unit vectors related to the Re unit mesh by $\overrightarrow{a_1}\begin{pmatrix} 2.761 \\ 0 \end{pmatrix}$ and $\overrightarrow{a_2}\begin{pmatrix} 0 \\ 4.456 \end{pmatrix}$.
The unit mesh contains the 7 Ag and Re atoms which undergo a symmetry-dependent geometrical displacement. Additionally to the surface relaxation in the z direction, atom pairs (2,3) and (6,7) can only move in the y direction, while the atom pair (4,5) is only allowed to move in the x direction.

The optimised structural parameters obtained for structure model (C) are summarised in Table 5.8. It reveals that the distance between the two Re atoms lying underneath and in direct contact with the topmost $Ag^{(1)}$ atom, $a_{4,5} = 2.68\,\text{Å}$, contracts by 2.9% when compared with the bulk distance. The varied distance $Ag^{(2)}$-$Ag^{(3)}$ was optimised and found to be $6.13(\pm 0.02)\,\text{Å}$. The so-called "Ag dimers"[15] positioned at every second Re short-bridge site are characterised by a distance of $2.78(\pm 0.02)\,\text{Å}$. The topmost Ag atom, $Ag^{(1)}$, is bound to $Ag^{(2,3)}$ atoms by $Ag^{(1)} - Ag^{(2)} = Ag^{(1)} - Ag^{(3)} = 3.092(\pm 0.02)\,\text{Å}$ in the [0001] direction. On the diagonals, $Ag^{(1)}$ forms four bonds to its next nearest neighbours such that $Ag^{(1)} - Ag^{(2')} = Ag^{(1)} - Ag^{(3')} = 3.12(\pm 0.02)\,\text{Å}$[16].

[15] Again, we indicate that the so-called "Ag dimer" consists of the pair formed by Ag atoms located in the Re three-fold hollow sites

[16] The primes refer to the symmetry equivalent next nearest Ag atoms.

Therm. vib. amplitudes	Reference value [Å]	Best fit value [Å]
$\nu(Ag_1)$	0.18	0.31
$\nu(Ag_2)$	0.18	0.30
$\nu(Ag_3)$	0.18	0.30
$\nu(Re_4)$	0.07	0.13
$\nu(Re_5)$	0.07	0.13
$\nu(Re_6)$	0.06	0.11
$\nu(Re_7)$	0.06	0.11
Vertical displacements [Å]		
d_{12}	0.60	0.41
d_{23}	1.80	1.97
d_{34}	0.78	0.7
d_{bulk}	1.53	1.55
Horizontal displacements [Å]		
$a_{2,3}$	6.68	6.13
$a_{4,5}$	2.76	2.68
$a_{6,7}$	4.46	4.62
V_{0r}	11.80	12.70
R_P-factor	0.66	0.32

Table 5.8: Optimised structural parameters for the Ag-c(2×2) structure model (C).

The Debye temperature for the topmost $Ag^{(1)}$ atoms is $\Theta_D = 160(\pm 20)\,K$. The $Ag^{(2,3)}$ atoms in the dimers located $0.41(\pm 0.02)$ Å below $Ag^{(1)}$ atoms are characterised by $\Theta_D = 175(\pm 20)\,K$. The distance found in the Ag dimer, $Ag^{(2')} - Ag^{(3')} = 2.78(\pm 0.02)$ Å implies a shrinking of the relative Ag radii by about 3.4%. This is not the first study that reveals this behaviour of silver[17]. In the fourth layer, *i.e.* the second and deepest considered Re layer, the Re bulk unit cell stretches by $\sim 3.6\%$, $Re^{(6)} - Re^{(7)} = 4.62(\pm 0.02)$ Å. Our estimation of Debye temperatures of Re layers, the mean square displacement obtained from our best fit is $0.13(\pm 0.02)$ Å, which corres-

[17] An early paper by Campbell about metal radii in surface science [9] reports an experimentally estimated Ag radius of 1.39 Å in the Pt(111)-Ag(1×1) system.

ponds to $\Theta_D = 400(\pm 28)\,K$ for the topmost Re layer, and to $\Theta_D = 500(\pm 60)\,K$ for the Re layer below.

The Ag(1×4) Phase

We proceeded to the LEED structural determination of the Ag(1×4) phase in a way similar to what has been done for the Ag-c(2×2) phase, our search has been extended to altogether six possible models as shown in Figure 5.24. These models span Ag coverages ranging from $\Theta_{Ag} = 1.25\,ML$ to $\Theta_{Ag} = 1.75\,ML$. It has to be kept in mind, however, that the Ag island growth can cause pronounced differences between the *global* coverage (as estimated from the geometry of the observed LEED pattern) and the *local* coverage, which can be markedly different and may vary between lower and higher values. Note that a satisfactory LEED superstructure already appears if only $\sim 50\%$ of the surface phase exhibits long-range order!

Unlike gold, silver does not form a (1×3) phase, nor does it form a sequence of (1×n) structures, see section 5.4. The first ordered Ag structure stable at $300\,K$ is the (1×4) phase. Specifically for silver, a major difficulty consists in the fact that the long-range order phases are T-dependent. Furthermore, as already seen for the c(2×2) phase, the theoretical analysis for this phase is hampered by the fact that silver can (and partly will) grow inhomogeneously.

Reference structure	Coverage [ML]	R_P-factor
(A)	1.25	0.69
(B)	1.25	**0.64**
(C)	1.50	0.68
(D)	1.50	0.74
(E)	1.75	**0.66**
(F)	1.75	0.81

Table 5.9: Reference calculation for the six tested Ag(1×4) structural models.

The six models depicted in Figure 5.24 were proposed on the basis of reproducing the (1×4)-symmetry, including the more unlikely models (D) and (F), which consist of an additional "B"-terminated Ag single-row in the uppermost plane. The reference calculation for these two models yielded R_P-factors beyond the error margin, $var(R_P) =$

0.08 for the cumulative energy range $\triangle E = 2466$, that makes structures with $R_P > 0.74$ unacceptable, see Table 5.9.

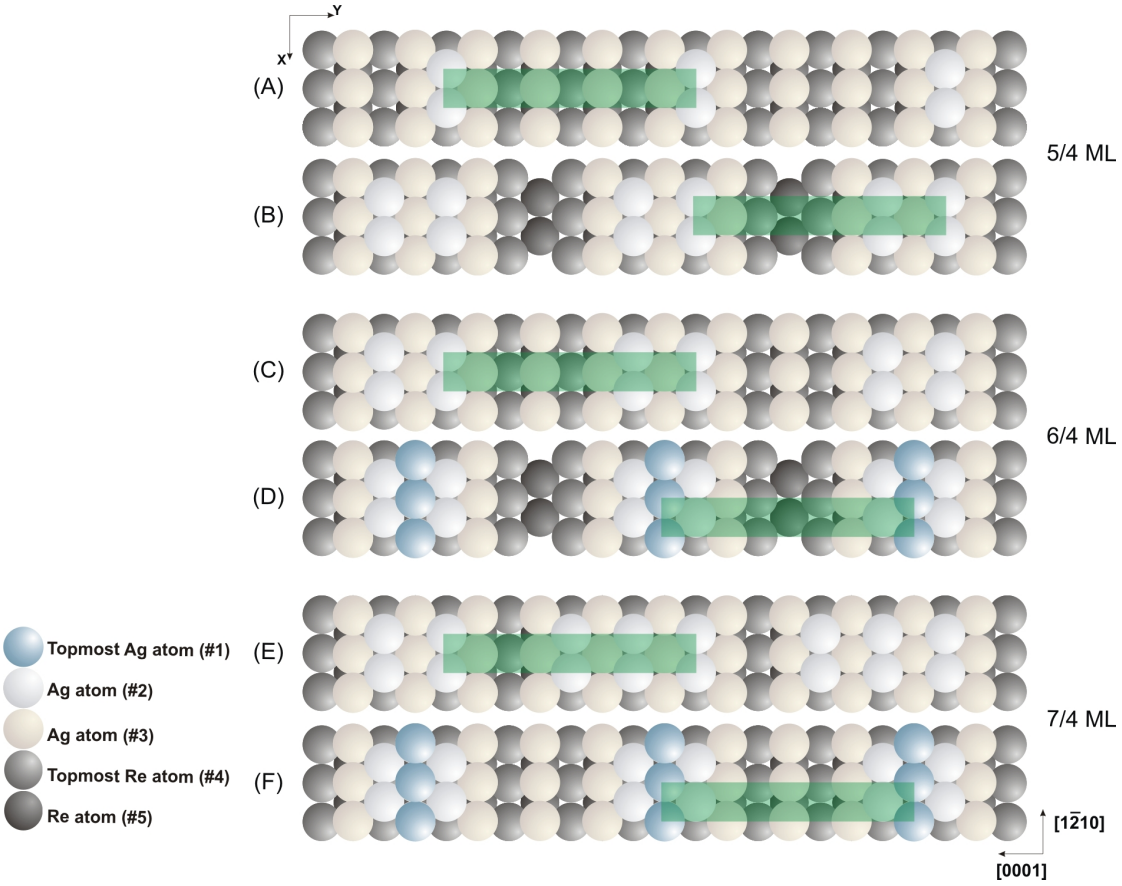

Figure 5.24: Various structure models tested for the Ag(1×4) phase.
The unit mesh is represented by the green rectangles and is in each case 4 times as large as the Re unit mesh. Beside these six structures, a few other possibilities to build a (1×4)-symmetry could be envisaged. However, structures involving single Ag adlayers (leading to a "B"-terminated surface) were intentionally ignored, as well as all models having non-pseudomorphic adsorption sites.

The optimisation of the remaining structures (A), (B), (C), and (E) has been undertaken. During this operation, the structures (A) and (C) at some points couldn't reach convergence below $R_P = 0.46$ and $R_P = 0.42$, respectively. Upon a more thorough optimisation, the lowest values of R_P have been reached for structures (B) and (E), with $R_P = 0.29$ and $R_P = 0.28$, see Figure 5.25.

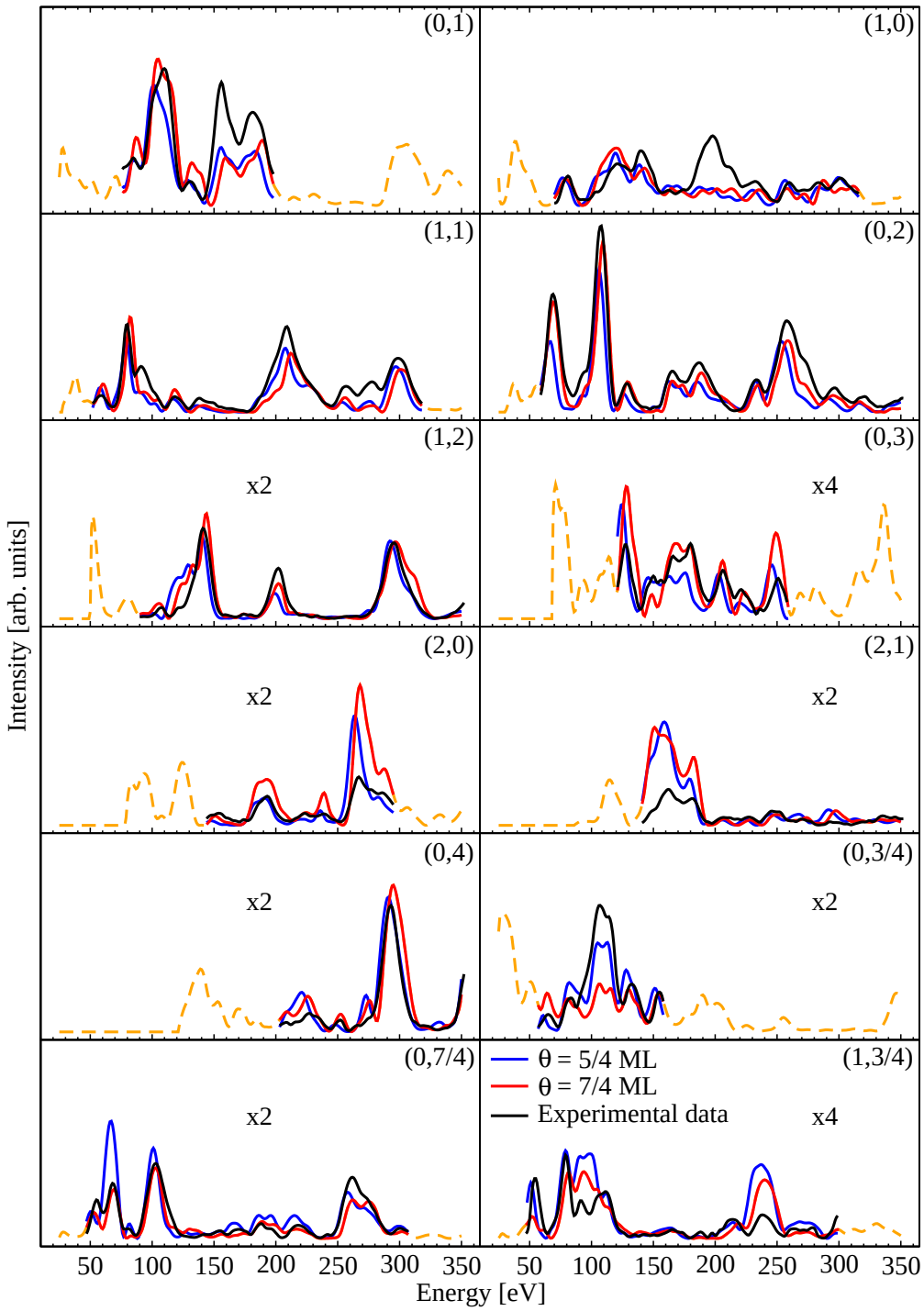

Figure 5.25: Optimised LEED-I,V spectra for the Ag(1×4) phase: models (B) and (E). In this case, the LEED-I,V spectra analysis appears to be insufficient to settle a decision between structures (B) ($\Theta_{Ag} = 5/4ML = 1.25ML$) and (E) ($\Theta_{Ag} = 7/4ML = 1.75ML$). The existence of another geometry that can lead to a better fit is quite unlikely. In fact, we can observe that although structure (E) has a coverage which is by 40% higher than that of structure (B), both structures exhibit a very similar topography even where the curves are less well-reproduced, *e.g.* for $E = 180 - 220eV$ in the (1,0) beam.

The R_P-factors relative to the fractional-order beams are found as 0.32 and 0.30 for structures (B) and (E), respectively. It is indeed quite peculiar not being able to clearly distinguish between these two structures upon a thorough LEED search procedure, nor to find visible discrepancies from the fitted spectra. Moreover, the Pendry R_{frac}-factors relative to the fractional-order beams have a $var(R_{frac}) = 0.07$, which is not small enough to rule out structure (B).

We used in the final LEED calculations for the real part of the potential the energy-dependent function: $V_{0r} = 6.85 + \frac{21.07}{\sqrt{E-24}}$ for structure (B), while for structure (E) the best fit only required the constant value $V_{0r} = 9.70\,eV$. We show in Figure 5.26 the respective geometrical displacements undergone by Ag and Re atoms in both structures (B) and (E).

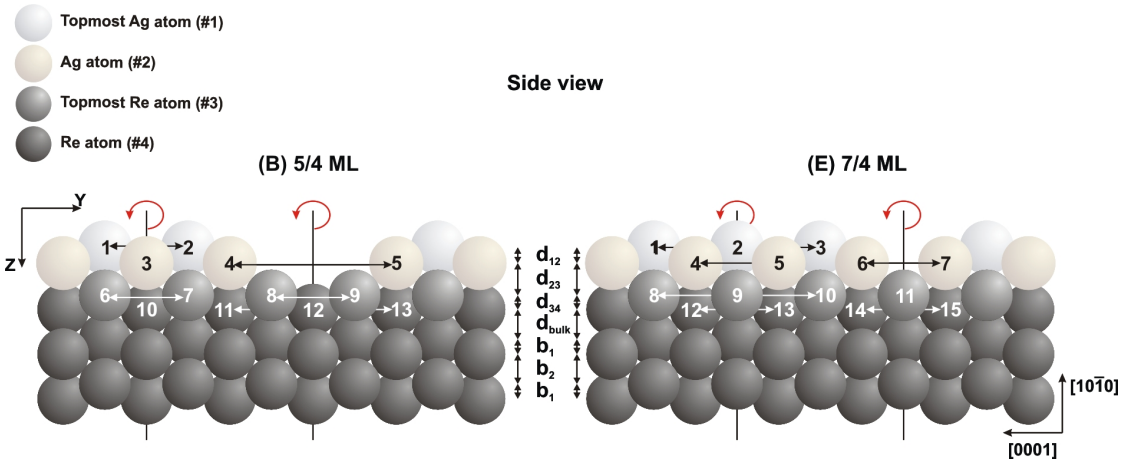

Figure 5.26: Geometrical displacements in the Ag(1×4) structure.
These geometrical displacements are symmetry-dependent. In the y direction they are represented by the respective arrows. Atoms located on the symmetry axes can only relax in the z direction. The numbered atoms are those undergoing the displacements given in Table 5.11.

The error margin on the lowest R_P-factor is calculated as 0.038 for structure (B) and as 0.04 for structure (E). The fitted geometrical displacements are also affected by an error margin corresponding to the variational step upon which a variation in R_P is detected. The same holds for the thermal vibrational amplitudes, which are presented in Table 5.10. The Debye temperature corresponding to the topmost Ag layer is found as $\Theta_D = 120(\pm 15)\,K$ for structure (B) and $\Theta_D = \{100;160\}(\pm 20)\,K$ for structure (E), where $160\,K$ is Θ_D characteristic of atom $Ag^{(2)}$, which is located on the axis of symmetry in the (x,y) plane. For the lower Ag layer we obtain for atom $Ag^{(3)}$

$\Theta_D = 430(\pm 60)\,K$ and for atoms $Ag^{(4,5)}$ $\Theta_D = 160(\pm 20)\,K$, in structure (B). In this respect, structure (E) exhibits a smaller difference, where the corresponding Debye temperatures are found as $\Theta_D = \{125\,;160\}(\pm 20)\,K$. Similarly, the thermal amplitudes of the topmost Re atoms in structure (B) are found to vary by $0.07(\pm 0.02)$ Å depending on whether these are located underneath the Ag double layer or in the wide trough. This is, however, not observed for structure (E), where the difference is markedly lower. In fact, the value of $\upsilon(Ag^{(6,7)})$ was carefully monitored during the search procedure and was found to constantly tend to low values. This is why it cannot be simply considered as a computational artefact, but rather seems to represent a counter-argument against structure (B).

	Reference	Best fit value [Å]			
Layer (#)	[Å]	$\Theta = 5/4\,ML$ (B)		$\Theta = 7/4\,ML$ (E)	
Ag-layer (#1)	0.18	$v(Ag_1)$	0.19	$v(Ag_1)$	0.23
	0.18	$v(Ag_2)$	0.19	$v(Ag_2)$	0.16
	0.18	–	–	$v(Ag_3)$	0.23
Ag-layer (#2)	0.12	$v(Ag_3)$	0.07	$v(Ag_4)$	0.16
	0.12	$v(Ag_4)$	0.17	$v(Ag_5)$	0.16
	0.12	$v(Ag_5)$	0.17	$v(Ag_6)$	0.19
	0.12	–	–	$v(Ag_7)$	0.19
Re-layer (#3)	0.07	$v(Ag_6)$	0.09	$v(Re_8)$	0.07
	0.07	$v(Ag_7)$	0.09	$v(Re_9)$	0.06
	0.07	$v(Re_8)$	0.02	$v(Re_{10})$	0.07
	0.07	$v(Re_9)$	0.02	$v(Re_{11})$	0.06
Re-layer (#4)	0.06	$v(Re_{10})$	0.09	$v(Re_{12})$	0.06
	0.06	$v(Re_{11})$	0.09	$v(Re_{13})$	0.06
	0.06	$v(Re_{12})$	0.07	$v(Re_{14})$	0.06
	0.06	$v(Re_{13})$	0.09	$v(Re_{15})$	0.06
Pendry *R*-factor		0.64	0.29	0.66	0.28

Table 5.10: Comparison of the thermal vibrational amplitudes for models (B) and (E).

The geometrical displacements in the *z* and *y* directions presented in Table 5.11 are those found for the "best" surface geometry in both cases. Again, a direct comparison

of these values is irrelevant in view of ruling out one of the structures. It is nevertheless interesting to point out that the distance between the topmost Ag atoms, namely $Ag^{(1,2)}$ in structure (B) and $Ag^{(1,3)}$ in structure (E), tend to increase by 3.6% in (B) and by 1.6% in (E). In other words, the repulsion of Ag atoms in (B) is twice as strong as the repulsion of Ag atoms in (E), which in itself could corroborate Vollmer's observations [57] (see section 5.3.3). We also note that the depth of the trough formed by the missing Ag rows is reduced in both structures by $\sim 4\%$.

Vertical displacements			
Distance [Å]	Reference value	$\Theta = 5/4\,ML$ (B)	$\Theta = 7/4\,ML$ (E)
b_1	0.00	0.00	0.10
d_{12}	0.84	0.70	0.67
b_2	0.00	0.12	0.11
d_{23}	1.73	1.69	1.68
b_3	0.00	0.08	0.07
d_{34}	0.76	0.74	0.72
b_4	0.00	0.08	0.06
d_{bulk}	1.53	1.48	1.50

Horizontal displacements					
[Å]	Reference	$5/4\,ML$	[Å]	Reference	$7/4\,ML$
$a_{1,2}$	4.456	4.616	$a_{1,3}$	8.912	9.052
$a_{4,5}$	8.912	8.532	$a_{4,5}$	4.456	4.696
$a_{6,7}$	4.456	4.396	$a_{6,7}$	4.456	4.276
$a_{8,9}$	4.456	4.536	$a_{8,10}$	8.912	8.722
$a_{11,13}$	8.912	8.992	$a_{12,13}$	4.456	4.556
–	–	–	$a_{14,15}$	4.456	4.656

Table 5.11: Vertical and horizontal displacements for structures (B) and (E).
The respective optimised parameters are shown in Figure 5.26. The $a_{i,j}$ is the varied interatomic distance in the y direction between atoms i and j.

The main conclusion from this part is that - although models (B) and (E) differ by a coverage of $0.5\,ML$ - the experimentally measured LEED-I,V curves can be reproduced

almost equally well by both models; one could even think of a coexistence of both structures in domains. We admit that in terms of R_P and R_{frac} values a slight advantage for structure (E) might appear, but the strong resemblance of the topography of these surfaces prevents a final decision by means of a LEED analysis only, as illustrated in Figure 5.27. Indeed, the three pseudomorphous Ag missing-rows in structure (B) are strictly equivalent to structure (E) from which the facet formed by atoms $Ag^{(3,6)}$ has been cut off. In other words, the twice as large width of the trough in structure (B) compared to structure (E) appears to have a little influence only on the shape of the respective LEED-I,V curves.

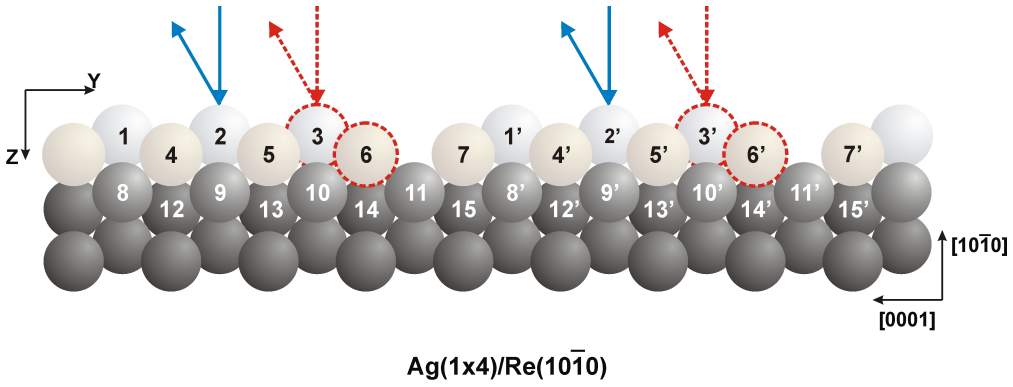

Figure 5.27: Illustration of similarities between Ag(1×4) structures (B) and (E). The removal of atoms $Ag^{(3,6)}$ from structure (E) with $\Theta_{Ag} = 1.75\,ML$ transforms the latter into structure (B) with $\Theta_{Ag} = 1.25\,ML$. Electron beams scattered by sites (3 and 3′) in structure (E) are equivalent to those scattered by sites (2 and 2′) in structure (B), as indicated by blue and red arrows, respectively. The numbering scheme follows that of structure (E) in Figure 5.24. The atoms marked with a prime are obtained by a mere translation in the y direction.

5.3.2.2 The Closed Bilayer

On the stable "A" surface termination of the Re(10$\bar{1}$0), silver forms a (1×1) LEED phase suggesting a pseudomorphic growth. As shown in Figure 5.17, a (1×1) pattern can first of all be produced by depositing just a single monolayer ($\Theta_{Ag} = 1\,ML$) of Ag atoms either in on-top, short- or long-bridge, or in 4-fold hollow lattice positions. However, any of these structures will produce the highly corrugated "B" termination of the (10$\bar{1}$0) surface, while only the addition of another Ag monolayer to a total of one bilayer ($\Theta_{Ag} = 2\,ML$) will restore the stable "A" termination. Support for the latter structural assumption is corroborated by two previous LEED analyses concerning 1) the (1×1) phase formed by copper atoms on Re(10$\bar{1}$0) where exactly this bilayer configuration

has led to the best R_P-factor, see section 5.2.2.1, and 2) the Au(1×1) phase formed on the same Re surface [34], where the Au atoms were found to simply continue the hcp lattice perpendicular to the surface.

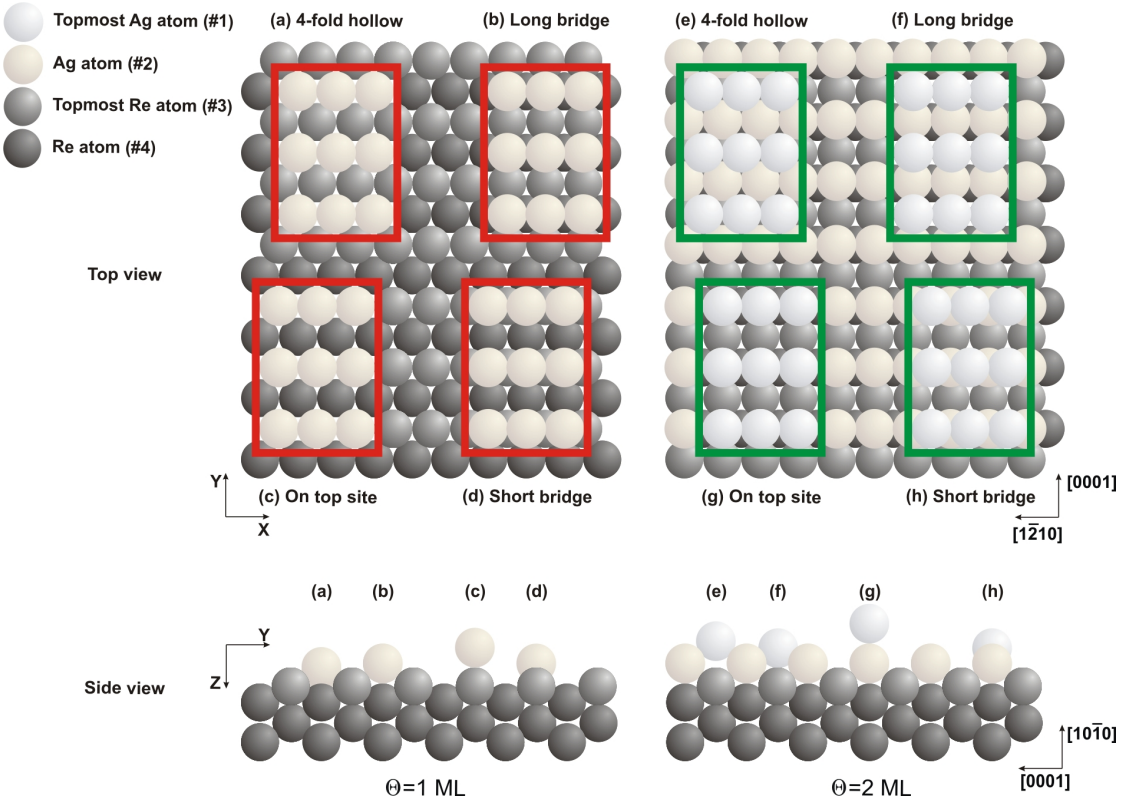

Figure 5.28: Schematic ball-model for the eight different tested Ag(1×1) structures. Structures (d), (e), (f), and (g) depict the four possible structures built on the pseudomorphic (b)-Ag layer. In the initial coarse LEED calculation, the latter yielded the lowest R_P-factor of 0.78, see Table 5.12.

Coarse LEED calculations have been performed for eight different surface geometries, including those with $\Theta = 1\,ML$. The four possibilities (a), (b), (c), and (d) shown in Figure 5.28 had also to be tested keeping in mind that silver atoms are by $\sim 5\%$ larger than Re atoms. The result found for copper is not evident enough to ignore these possibilities, although they are very improbable. The initial reference calculation for the eight models yielded by far the lowest value, $R_P = 0.38$ and $var(R_P) \backsimeq 0.06$, for structure (e). In other words, the real-space Ag structure on the Re($10\bar{1}0$) surface is, as expected, the "A"-terminated pseudomorphous Ag bilayer, giving account for a Stranski-Krastanov-like growth mode. This result is nicely in line with our findings for copper (see section 5.2) as well as for gold (see section 5.4) on the same Re surface.

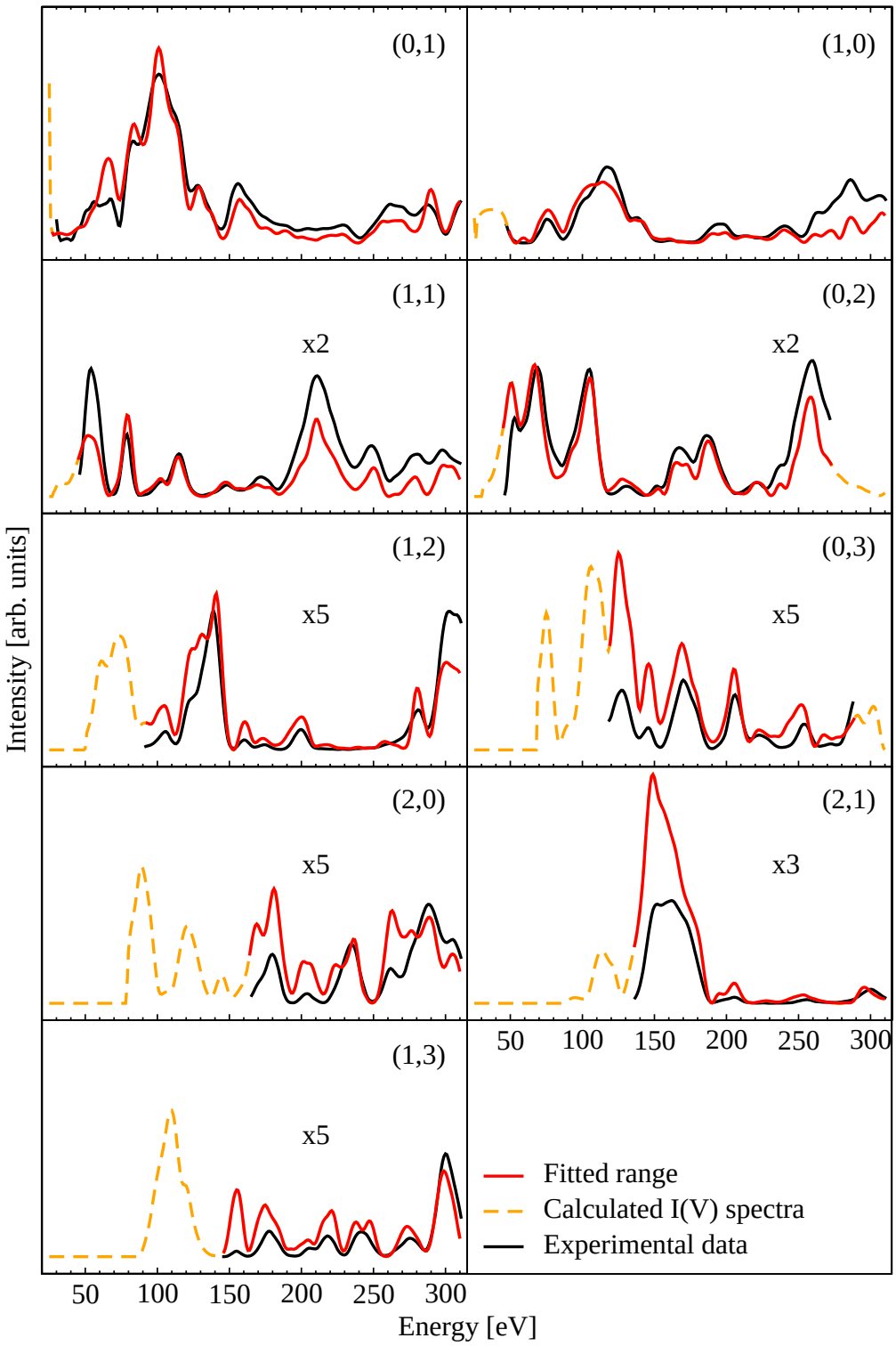

Figure 5.29: Optimised LEED-I,V spectra for the Ag(1×1) phase.

Structure	Site	(#) of Ag layers	R_P-factor
(a)	4-fold hollow	1	0.94
(b)	Long-bridge	1	0.78
(c)	On-top	1	0.93
(d)	Short-bridge	1	0.93
(e)	4-fold hollow	2	**0.38**
(f)	Long-bridge	2	0.80
(g)	On-top	2	0.93
(h)	Short-bridge	2	0.93

Table 5.12: R_P-factor calculated for the different tested Ag(1×1) reference structures.

The refinement of structure (e) for nine diffracted beams has led to quite a good agreement with the experimental I,V curves, see Figure 5.29. The lowest value of $R_P = 0.23$ was reached for an overall energy range of 1701 points.

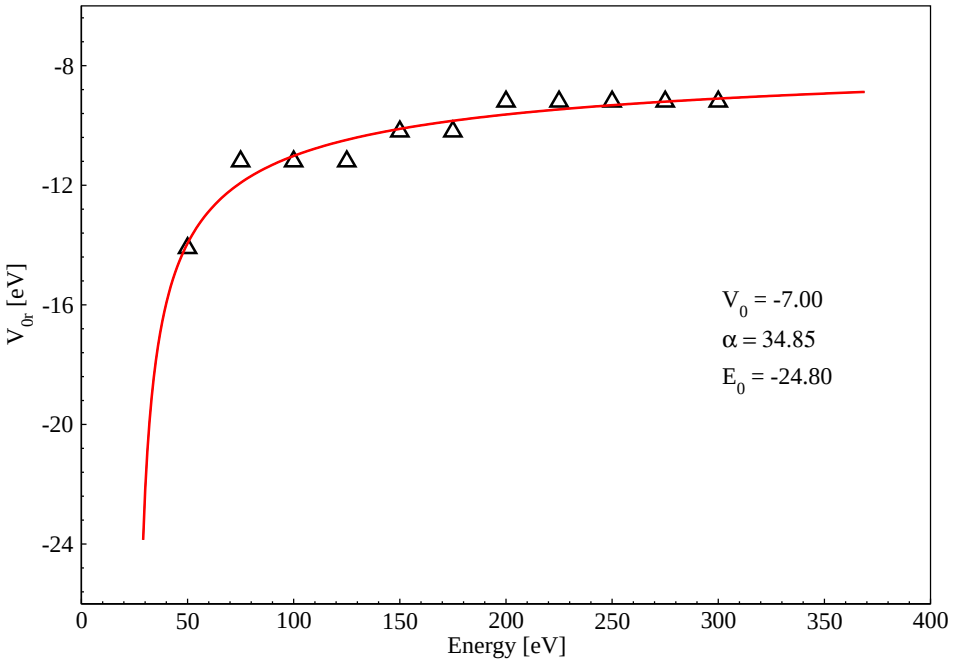

Figure 5.30: Optimisation of the energy-dependent inner potential for the Ag bilayer. $V_{0r}(E)$ was calculated within selected energy intervals of $50\,eV$ according to fit parameters $\alpha = -34.85$, $V_0 = -7.00\,eV$, and $E_0 = 24.80\,eV$. In this way, the R_P-factor could be improved by $\triangle R_P = -0.02$.

The real part of the potential was fitted by $V_{0r} = \left(-7.00 + -\frac{34.85}{\sqrt{E-24.80}}\right) eV$, which led to the improvement of the R_P-factor value by -0.02. For the (1×1)-symmetry, 8 independent parameters have been simultaneously varied, see Figure 5.30. In addition to the thermal vibrational amplitudes corresponding to each Ag and Re atom of the topmost surface layer, the interlayer distances (shown in Figure 5.31) have been optimised, respectively, with an unmodified (x,y)-plane symmetry.

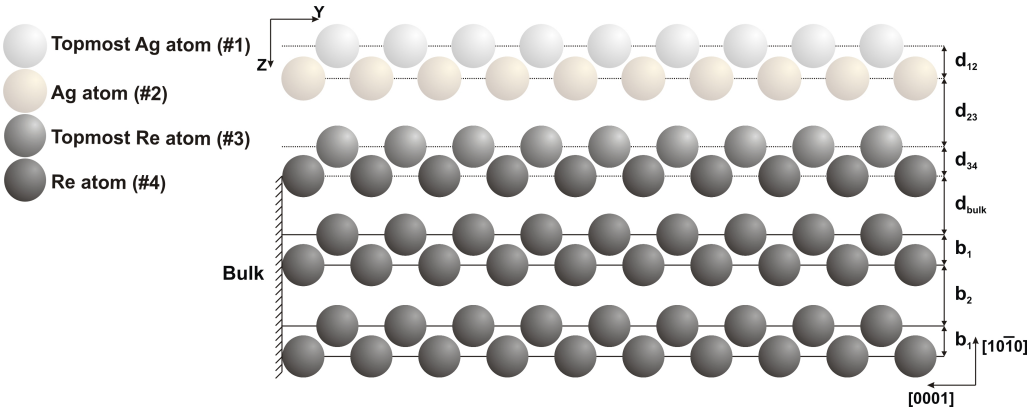

Figure 5.31: Schematic illustration of the optimised Ag(1×1) structure (e).

The topmost $Ag^{(1)}$ layer is characterised by a Debye temperature, $\Theta_D = 160(\pm20)\,K$, the $Ag^{(2)}$ layer below has a $\Theta_D = 200(\pm20)\,K$. We remind that the LEED measurements for the Ag(1×1) phase were performed at $T = 120\,K$. These values lie in the same range as those previously calculated for gold by C. Pauls, namely $\Theta_D(Au^{(1)}) = 170\,K$ and $\Theta_D(Au^{(2)}) = 200\,K$, calculated from the analysis of LEED-I,V curves measured at room temperature [33]. Interestingly, the mean square displacement corresponding to the topmost $Re^{(3)}$ layer is relatively high, $\upsilon_3(Re) = 0.12\,\text{Å}$, while it was found as $0.08\,\text{Å}$ in the Cu/Re system and as $0.07\,\text{Å}$ in the Au/Re system. This conspicuous difference can be interpreted as a direct consequence of the inhomogeneous character of Ag growth: As we have already pointed out when discussing the TPD spectra of Figure 5.19, the sub-bilayer spectra (in red) exhibit for coverages, $\Theta_{Ag} \lesssim 2\,ML$, a slight increase in the α-state region, precisely around $T \sim 930\,K$, although the first bilayer is by no means completed. This suggests that Ag atoms, unlike Cu and Au, tend to grow in multilayers before the bilayer is completely closed, thereby leaving uncovered Re patches and the possibility of elevated vibrational amplitudes.

Th. vib. amplitude	Reference value [Å]	Best fit value [Å]
ν_1(Ag)	0.18	0.16
ν_2(Ag)	0.12	0.13
ν_3(Re)	0.07	0.12
ν_4(Re)	0.06	0.04

Table 5.13: Characteristic thermal vibrational amplitudes for the Ag(1×1) phase.

The optimised geometry of the Ag(1×1) structure is characterised by the vertical displacements summarised in Table 5.14. The Ag atoms in the bilayer have a distance, $Ag^{(1)} - Ag^{(2)} = 2.757(\pm 0.001)$ Å, whereas Ag atoms are bound to the Re topmost layer by $Ag^{(2)} - Re^{(3)} = 2.855(\pm 0.001)$ Å. The $Re^{(3)} - Re^{(4)}$ distance is not much more affected than the equivalent distance in the clean Re surface, $0.781(\pm 0.001)$ Å. And the distance to the bulk, d_{bulk}, is found to be the same as the one calculated for gold, but by $\sim 2\%$ smaller than that calculated for the Cu/Re system.

Distance	Reference value [Å]	Best fit value [Å]
d_{12}	0.840	0.857
d_{23}	1.730	1.785
d_{34}	0.757	0.771
d_{bulk}	1.534	1.534

Table 5.14: Optimised interlayer distances for the Ag(1×1) phase.

5.3.3 Silver Growth Mode and the Phase-Transition c(2×2)↔(1×4)

Our LEED analyses of the different Ag phases formed on the clean Re($10\bar{1}0$) surface corroborate the combined MEED and TPD results, which show that the silver growth follows a Stranski-Krastanov-like simultaneous-multilayer growth mode: It was found that higher layers are already populated before the first Ag bilayer is completed. We consider this to be the reason for the relatively high thermal vibrational amplitude found for the topmost Re layer (see Table 5.13).

Concerning the sub-bilayer coverage range, our LEED analysis has shown that structures with coverages $1.25\,ML$ and $1.75\,ML$, see Figure 5.24 (B) and (E), respectively, reproduce the experimtal I,V curves equally well and can hardly be distinguished from

each other (see Figure 5.25). In order further to clarify matters, we recall Vollmer's STM measurements for low *global* Ag coverages ($\sim 0.3\,ML$) [57]. Within the limits of resolution, the STM images suggest an alternating structure of two bright and two dark rows, see Figure 5.32 on the left. This picture can be directly associated with Ag(1×4) structure (B) rather than the model originally proposed by Vollmer, which consists of a single-layer of "B"-terminated Ag double-rows alternating with two empty rows. Our new findings suggest a different interpretation: The Ag atoms in the low coverage range adsorb in the pseudomorphic sites and tend, due to attractive forces, to aggregate in bilayer-slabs, leaving relatively broad troughs inbetween.

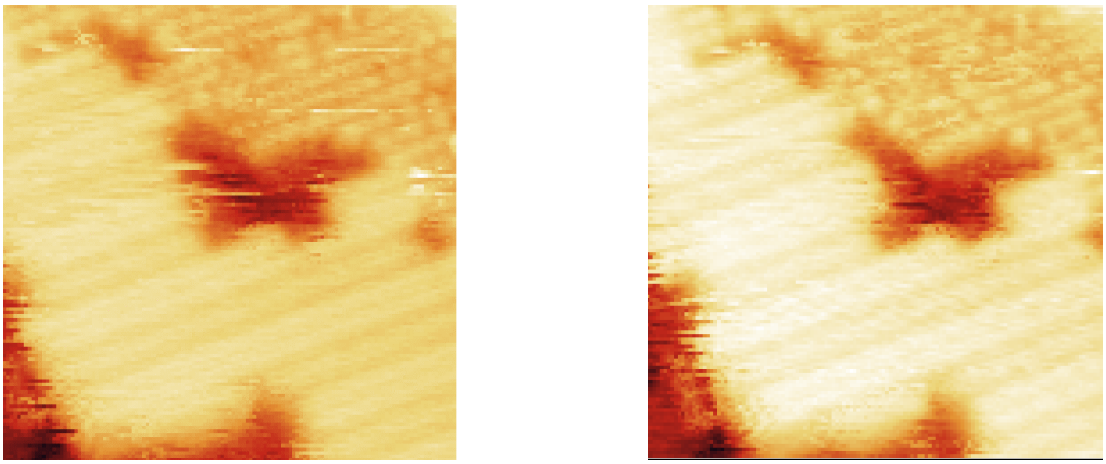

Figure 5.32: Atomic scale structure of a Ag(1×4)/Re(10$\bar{1}$0) island.
STM measurements for $\Theta_{Ag} = 0.3\,ML$ with a resolution of 88 Å × 88 Å. Tunnel current and voltage were $I = 1.46\,nA$ and $U = 0.011\,V$. The right picture shows the Ag row shift after within a few minutes [57].

Interestingly, Vollmer observed that within a few minutes under constant room temperature conditions, an Ag row can shift in one particular direction leading to the formation of a slab of three rows, see Figure 5.32 on the right. Scherf observed silver layers with a (1×4) periodicity for the broad coverage range $0.2\,ML \leqslant \Theta_{Ag} < 2\,ML$, *i.e.* also for coverages exceeding $1.25\,ML$. This means that the surface for which LEED-I,V curves were provided cannot consist of structure (B) only. More plausible is that the surface contains coexisting domains of structures (B) and (E) and possibly uncovered Re patches, as follows:

$$\Theta_{glo}^{(1\times4)} = c_B \times \Theta_{Ag}^{1.25\,ML} + c_E \times \Theta_{Ag}^{1.75\,ML} + c_{Re} \times \Theta_{Ag}^{0\,ML}, \tag{5.2}$$

where the coefficients c_B, c_E, and c_{Re}[18] refer to the ratio of domains (B), (E), and the uncovered Re patches, respectively. In the ideal case where the averaged *local* coverage equals the *global* one (found as $1.5\,ML$ in the experiment), equation 5.2 is satisfied by the coexistence of both Ag structures with equal proportion and with $c_{Re} = 0$. Assuming that in this case the Ag(1×4) phase consists of structure (E) only, then the coefficient c_{Re} would be equal to ~ 0.14.

The optimised c(2×2) structure as it comes out of our calculation is structure (C) with $\Theta_{Ag} = 1.5\,ML$, see Figure 5.20. Experimentally, Scherf finds that the c(2×2) phase has the highest LEED intensity for a *global* coverage, $\Theta_{Ag,glo} = 1.34\,ML$. Keeping in mind the difference between Θ_{loc} and Θ_{glob}, we thus assume that the analysed area in the experiment is $\sim 89\%$ covered by Ag-c(2×2)-(C) structure islands, according to:

$$\Theta_{glo}^{c(2\times2)} = c_C \times \Theta_{Ag}^{1.5ML} + c_{Re} \times \Theta_{Ag}^{0ML}, \tag{5.3}$$

where $c_C = 0.89$ and $c_{Re} = 0.11$.

Regarding the reversible T-dependent c(2×2)↔(1×4) order-order phase transition, it has been experimentally observed that this transition takes place at higher temperatures if Θ_{Ag} exceeds $1\,ML$ than those if $\Theta_{Ag} \leqslant 1\,ML$. Unfortunately, the respective phase transition is strongly influenced by spurious coadsorption of carbon monoxide, whereas a change in entropy of the CO-free system rather plays an insignificant role (more thermodynamical aspects are discussed in Scherf's thesis [44]). Note that our findings regarding the c(2×2) phase suggest that 11% of uncovered Re surface area still offer abundant sites for (dissociative) CO adsorption upon cooling [33]. In addition, we emphasise that many references to c(2×2) structures exist in the literature, commonly discussing structure models equivalent to structures (A) and (F) in Figure 5.20 [65, 22, 64, 27, 7]. A filled honeycomb-like structure such as the structure (C), which we propose here, has to our knowledge not yet been reported.

To conclude, the judicious association of experimental results and theoretical analysis of the Ag/Re($10\bar{1}0$) system makes us believe that Ag atoms form the c(2×2) phase with a filled honeycomb-like pattern, according to structure (C). Another notable fact about this model with a *local* coverage of $1.5\,ML$, is the agreement that it shows with the MEED observation, in that the peak intensity relative to the c(2×2) phase is actually by $\sim 22\%$ higher than that corresponding to the closed bilayer, see Figure 5.18. We recall that MEED is an excellent probe for the surface smoothness. In this respect, the distance between the two top Ag layers is estimated as $0.41\,\text{Å}$ in model (C), while the

[18] $c_{Re} = 1 - (c_B + c_E)$.

(1×1) closed bilayer exhibits a distance of about 0.86 Å, in other words, this is twice as large as in the c(2×2) structure (C) we propose.

In comparison to any of the other proposed models the formation of the (1×4) phase from the c(2×2) structure with its filled honeycomb-like arrangement upon cooling requires little rearrangement of the Ag layer; namely the mere translation of the three-fold coordinated Ag atoms to the nearby long-bridge sites, and a lateral hopping of the Ag atom centred in the hexagon. An order-order transition that leads, under compression, to the formation of a uniform Ag(1×4) structure (E) along with the uncovering of about 24% of the Re substrate[19].

[19]The phase transition c(2×2)→(1×4) occurring at $\Theta_{glo}^{c(2\times2)} = 1.34 ML$ implies a silver layer contraction leaving ∼ 24% of uncovered Re surface area.

5.4 Gold Adsorption on Rhenium($10\bar{1}0$)

Several studies of gold epitaxy on different metal substrates, mainly rhenium and ruthenium, were performed in our group [33, 58, 60]. The quantitative structural LEED analysis on the system Au/Re($10\bar{1}0$) described in this work was undertaken in order to shed light on the structure of the experimentally observed long-range ordered Au-phases. In detail, our LEED analysis is essentially based on experiments performed by Pauls, and accordingly, we will first give a brief overview of the experimental findings, including a previous theoretical investigation of the Au(1×1) phase [33], then move on to our theoretical investigation of the Au($1\times$n) phases, with n = 1, 3, and 4.

5.4.1 Experimental Results - MEED and LEED

Pauls undertook his experimental investigations of the Au/Re($10\bar{1}0$) system in order to elucidate the complex interplay between surface bound CO and deposited Au films. He came up with an interesting correlation between the thermodynamic spreading pressure of the CO adsorbate and the formation of long-range ordered submonolayer Au($1\times$n) superstructures.

The deposition of Au vapour at $800\,K$ on the rhenium surface has been investigated by MEED and the resulting films by LEED-I,V measurements. The elevated temperature has been chosen to avoid CO coadsorption and to facilitate any possible Au ordering by surface diffusion. The first observed overlayer structure has a (1×3) periodicity, which, according to Pauls, occurs in the coverage range between $0.28\,ML$ and $1.33\,ML$. Upon increasing the Au coverage, a series of (1×4), (1×5), and (1×6) structures appears. Finally, a (1×1) structure manifests itself which was assigned a coverage of $2\,ML = 1\,BL$. At higher gold coverages up to $8\,ML$ a (1×8)-LEED structure develops that has been attributed to a hexagonal by reconstructed gold layer on top of pseudomorphic hcp Au terraces.

The grazing MEED measurements, where again the intensity of the directly reflected (0,0) $5\,keV$-electron beam is plotted *versus* the deposition time, exhibit two pronounced intensity maxima separated by a deep minimum around $t_{evap} \approx 9\,min$ as well as some (rather significant) wiggles between 4 and $7\,min$ [34]. Owing to the strictly constant Au vapour flux, the time scale can be 1 : 1-converted to Au coverages.

The occurrence of the second maximum at about $t_{evap} \approx 12\,min$ always coincides with the fully developed pseudomorphic (1×1) LEED pattern and is a clear indication for a smooth surface that acts as a “mirror” for the grazing incidence MEED electrons.

By means of careful calibration measurements the coverage associated with this (1×1) phase was revealed $\Theta_{Au} = 2\,ML$ (or 1 bilayer (BL) respectively). At very small coverages and sufficiently high temperatures (as in Pauls' deposition experiment), the Au atoms form a homogeneous $2D$ lattice gas, where the Au atoms are believed to decorate and heal the inherent step and defect sites of the clean Re surface. This should lead to an improved smoothening, since we know from thermal desorption data on other Re surfaces that typical defect densities are about $3-5\%$ of the monolayer density [32, 58]. However, as soon as the coverage increases, $2D$ solid Au islands become stable in equilibrium with the still existing lattice gas and lead to an increased roughness of the surface. This in turn causes a progressive decrease of the MEED intensity until a minimum is reached at Au coverages where the whole surface is covered by dispersed (1×3) islands. If the Au deposition is continued after the first MEED minimum, we find a steep re-increase until a sharp second maximum is formed which coincides, as mentioned above, exactly with the Au coverage necessary to form the complete Au bilayer. Apparently, this (1×1) layer has a similar "electron reflectivity" as the clean Re$(10\bar{1}0)$ surface.

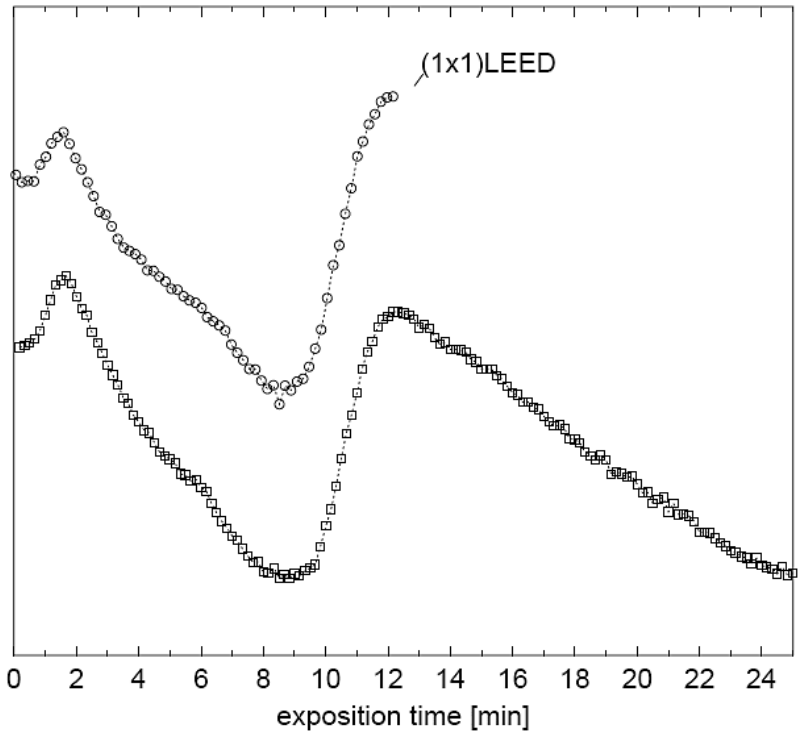

Figure 5.33: Au/Re$(10\bar{1}0)$ MEED (0,0) intensity as a function of Au coverage.

5.4.2 LEED Structural Analysis

Although the structural LEED investigation of the Au(1×1) phase had already been performed by Pauls we nevertheless analysed the LEED-I,V curves a second time in order to gain experience with the respective computational procedure and to verify Pauls' results. This is important in view of a seamless transition to the structure analysis of the Au(1×3) and (1×4) phases with their considerably larger unit cells, which is one of the main efforts of this work.

5.4.2.1 The Closed Bilayer

The Au(1×1) phase was subject to a quantitative TensErLEED analysis described in Pauls' PhD thesis [33]. The approach being similar to the one for the Cu(1×1) and Ag(1×1) phases and leading to the same result in terms of coverage and morphology.

We recall that gold has an atomic radius $r_{Au} = 1.44\,\text{Å}$, and thus the Au atom is by $\sim 5\%$ larger than a Re atom, which leads to a negative lattice misfit. Apart from the fact that in the phase shifts calculations an Au muffin-tin radius was used equal to that of Re ($2.58\,a.u.$), the procedure followed for the Cu/Re and Ag/Re systems was repeated for gold. The LEED-I,V curves for the Au(1×1) phase were measured in the energy range $E = 50 - 350\,eV$. In Figure 5.34 we show them alongside the calculated and optimised I,V spectra. All in all, the curves were successfully reproduced and yielded an R_P-factor of 0.22 in the above mentioned energy range and of 0.17 in the energy range $E = 50 - 230\,eV$. Indeed, among the eight structure models also described for silver in Figure 5.28 on page 105, the pseudomorphic bilayer is by far the best one for the Au(1×1) structure, as well.

The two gold layers undergo a relaxation of $+3\%$ for d_{12} (0.82 Å) and $+6\%$ for d_{23} (1.69 Å) in comparison with the ideally terminated Re crystal. The changes in the Re substrate layers are found to be the same as in the Ag(1×1) phase, see Table 5.14.

5.4.2.2 Sub-Bilayer Coverages

The Au(1×3) Phase

Pauls observed that the first well-ordered Au overlayer phase is a (1×3) phase, displayed in Figure 5.35. The intensity maximum of the fractional-order LEED spots was reached after a deposition time t_{evap} of *ca.* $8\,min$. According to Figure 5.33, this should be related with a coverage of $\Theta^{(1\times3)} = \frac{4}{3} = 1.33\,ML$.

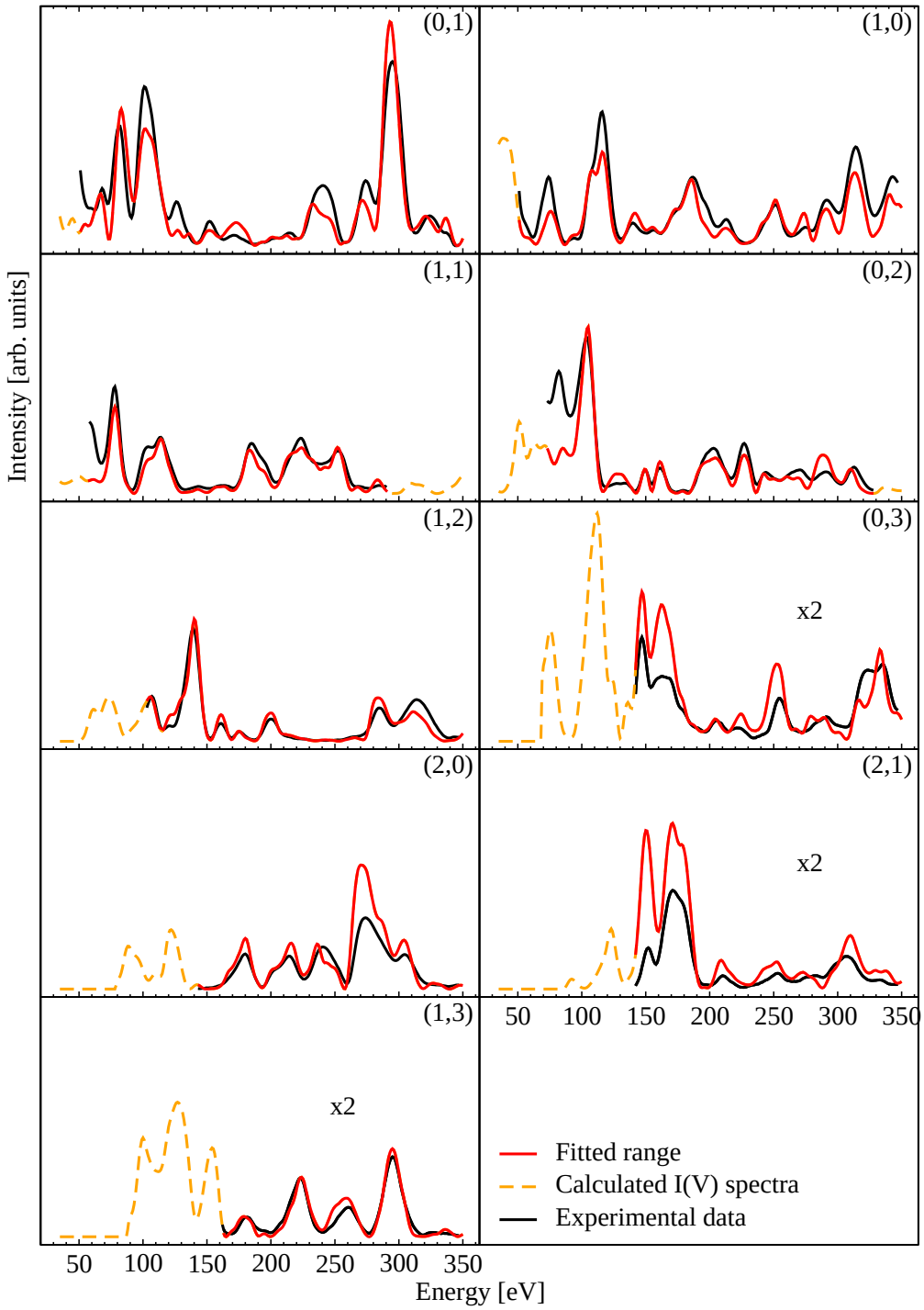

Figure 5.34: Optimised LEED-I,V spectra for the Au(1×1) phase.

It is also noticed that the (1×3) structure appears for the first time already at a coverage of $\sim 0.28\,ML$ and persists up to $\Theta = 1.33\,ML$, after which a gradual shift and splitting of the "extra" spots begins. Furthermore, there is an almost linear increase in the intensity of the fractional-order beams up to the assumed *global* coverage $\Theta^{(1\times3)} = 1.33\,ML$.

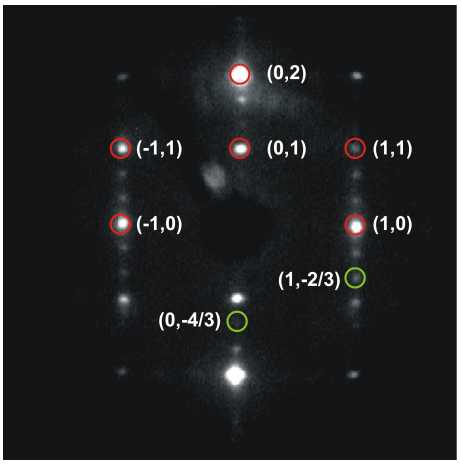

Figure 5.35: Au/Re($10\bar{1}0$) (1×3) LEED pattern.
Measured at room temperature with an electron energy of $110\,eV$ [33]. The additional fractional-order reflexes of the Au(1×3) structure are clearly visible.

The linear increase of the fractional-order beam intensity is indicative of island-like growth of small (1×3) domains (small compared to the LEED transfer width). The overall situation in the assumed coverage range $0.28 \leq \Theta \leq 1.33$ can then be described by an equilibrium in which (1×3) Au islands coexist with a homogeneous Au lattice gas phase or uncovered Re patches, depending on temperature. The Au adsorbate consists of spatially separated homogeneous phases with different densities, and as the coverage increases at a given temperature, the equilibrium is shifted in favour of the higher-density phase. We further note that the lower limit of the (1×3) phase, *i.e.,* $\Theta = 0.28\,ML$, coincides exactly with the first intensity maximum observed in the MEED experiment and that is followed, for increasing coverages, by a strong intensity decrease, thus supporting the idea that the beginning appearance of "$2D$ solid" (1×3) islands impairs the reflectivity for MEED electrons.

The (1×3) pattern implies a three-fold periodicity in [0001] direction as compared to the Re substrate lattice (the unit mesh is illustrated by the green rectangle in Figure 5.36 and is $13.368\,\text{Å} \times 2.761\,\text{Å}$). The resulting surface contains Au triple or quintuple chains

parallel to the $[1\bar{2}10]$ direction interrupted in [0001] direction either by single empty rows (corresponding to a coverage of $\Theta = \frac{5}{3}\,ML$) or by dual empty rows (coverage of $\frac{4}{3}\,ML$), see Figure 5.36.

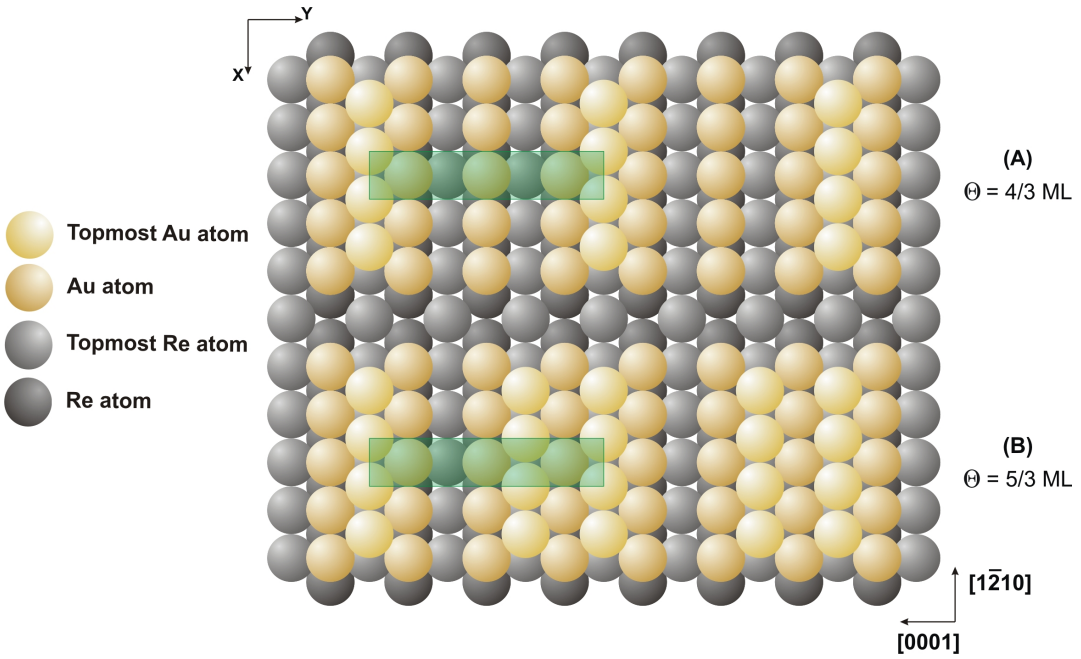

Figure 5.36: Ball models representing the two possible Au(1×3) structural models.

The determination of the Au(1×1) structure and thereby a Stranski-Krastanov growth mode of Au atoms on this Re surface is an important result, in that it will save both time and effort in the theoretical investigation of Au phases with higher periodicities. In fact, it is senseless to test possible Au adsorption sites other than the long-bridge for the first monolayer and the 4-fold hollow for the topmost one (same as model (e) in Figure 5.7 on page 69). Building a (1×3)-symmetry with an estimated coverage of $\Theta_{Au} \sim 1.33\,ML = 0.66\,BL$ doesn't leave much space to other structures than the two possibilities (A) and (B) illustrated in Figure 5.36.

Two reference calculations have been prepared for the Au(1×3) structure. Given that the phase shifts are more dependent on the chemical nature of the system than on the geometry, and that it is more important that the chemical sites correctly be specified in the reference calculation, it was unnecessary to re-calculate the phase shifts for the (1×3) structure, and accordingly, those already calculated for the (1×1) phase were used. The inner potential was taken as $V_0 = (11.8 + 5i)\,eV$, whose real part was again considered as a fit parameter.

In the case where the superlattice has a periodicity different from that of the bulk, two types of layers must be considered, toplayers with a 3-fold periodicity (1×3) and underlayers with bulk periodicity (1×1). A schematic view of models (A) and (B) is shown in Figure 5.37. Each one of them consists of a 4 sublayer slab (2 Au +2 Re layers) separated from the Re bulk by a distance d_{bulk}. This quantity was also subject to variation.

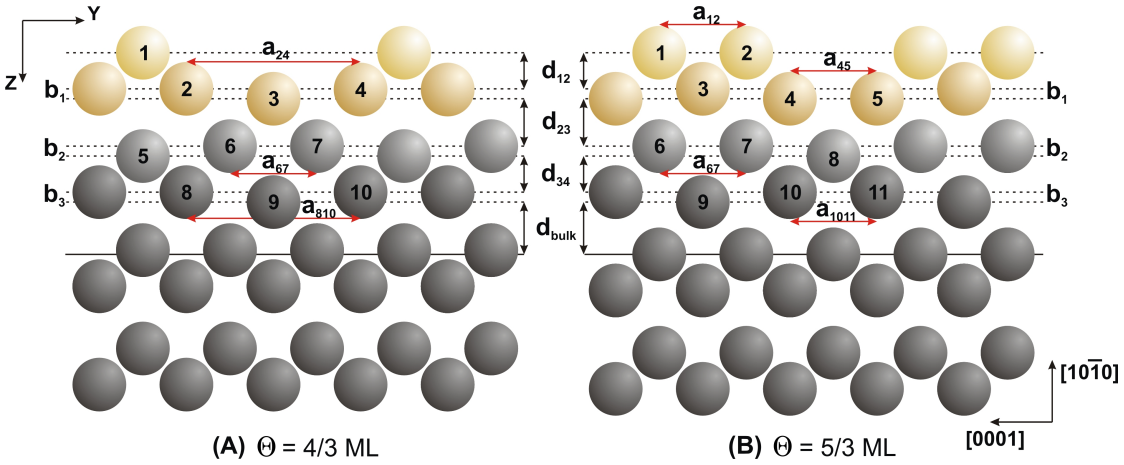

Figure 5.37: Schematic view of the varied distances in the Au(1×3) structures.
Distances d_{ij} and b_i were all simultaneously varied with thermal vibrational amplitudes for each structure, see Table 5.16 on page 122.

This slab contains 10 inequivalent atoms for structure (A) and 11 such atoms for (B), this means that the location of any of these atoms is reproduced 13.368 Å, *i.e.* three unit meshes, further in the y direction. The optimised distances from the Au (1×1) phase were, for consistency, taken as initial values for both reference structures (A) and (B).

The reference calculation, performed for 12 diffracted beams (8 integer + 4 fractional-orders), yielded an R_P-factor of 0.47 and 0.45 for structures (A) and (B), respectively. A thorough optimisation of both structures was, unlike as for the (1×1) phase, necessary. It was performed by submitting thermal vibrations and geometrical displacements to a simultaneous variation, namely, the optimisation of a set of 20 and 22 independent parameters, respectively. Another constraint in comparison to the (1×1)-symmetry was that additionally to the vertical displacement z, atomic displacements in the y direction had now to be considered.

The optimisation of both structures led to $R_P = 0.31$ and 0.21 for structures (A) and (B), respectively. The total energy range is $1748\,eV$, which yields a statistical error, $var(R_P) = 0.03$. Structure (A) can therefore in principle be ruled out.

In Figure 5.38, where calculated LEED-I,V spectra are plotted for structures (A) and (B), three major discrepancies between theory and experiment are to be noticed. At $E = 50\,eV$ in the (0,1) beam, between $180\,eV$ and $200\,eV$ in the (1,3) beam, and between $90\,eV$ and $140\,eV$ in the fractional-order beam (0,4/3). Additionally to the R_P value, these three locations represent a strong argument against structure (A). Indeed, it was by no means possible to improve the fit quality in these regions, whereas the curves for structure (B) show a much better agreement with the experimental ones.

Thermal vibrational amplitude v_i[Å]		Reference structure	Best fit value $\Theta = 4/3\,ML$	Best fit value $\Theta = 5/3\,ML$
Au-layer (#1)	$v(Au_1)$	0.18	0.02	0.15
	$v(Au_2)$	0.18	–	0.15
Au-layer (#2)	$v(Au_3)$	0.12	0.06	0.07
	$v(Au_4)$	0.12	0.14	0.12
	$v(Au_5)$	0.12	0.06	0.12
Re-layer (#3)	$v(Re_6)$	0.07	0.12	0.08
	$v(Re_7)$	0.07	0.09	0.08
	$v(Re_8)$	0.07	0.09	0.05
Re-layer (#4)	$v(Re_9)$	0.06	0.01	0.06
	$v(Re_{10})$	0.06	0.04	0.06
	$v(Re_{11})$	0.06	0.01	0.06
Inner potential (V_{0r})		$11.80\,eV$	$12.20\,eV$	$12.80\,eV$
R_P-factor		0.47/0.45	0.31	0.21

Table 5.15: Thermal vibrational amplitudes compared for the tested Au(1×3) models. Note that in Figure 5.39 the number of atoms is limited to 10 for structure (A). That is why there is no $v(Au_2)$ in this case.

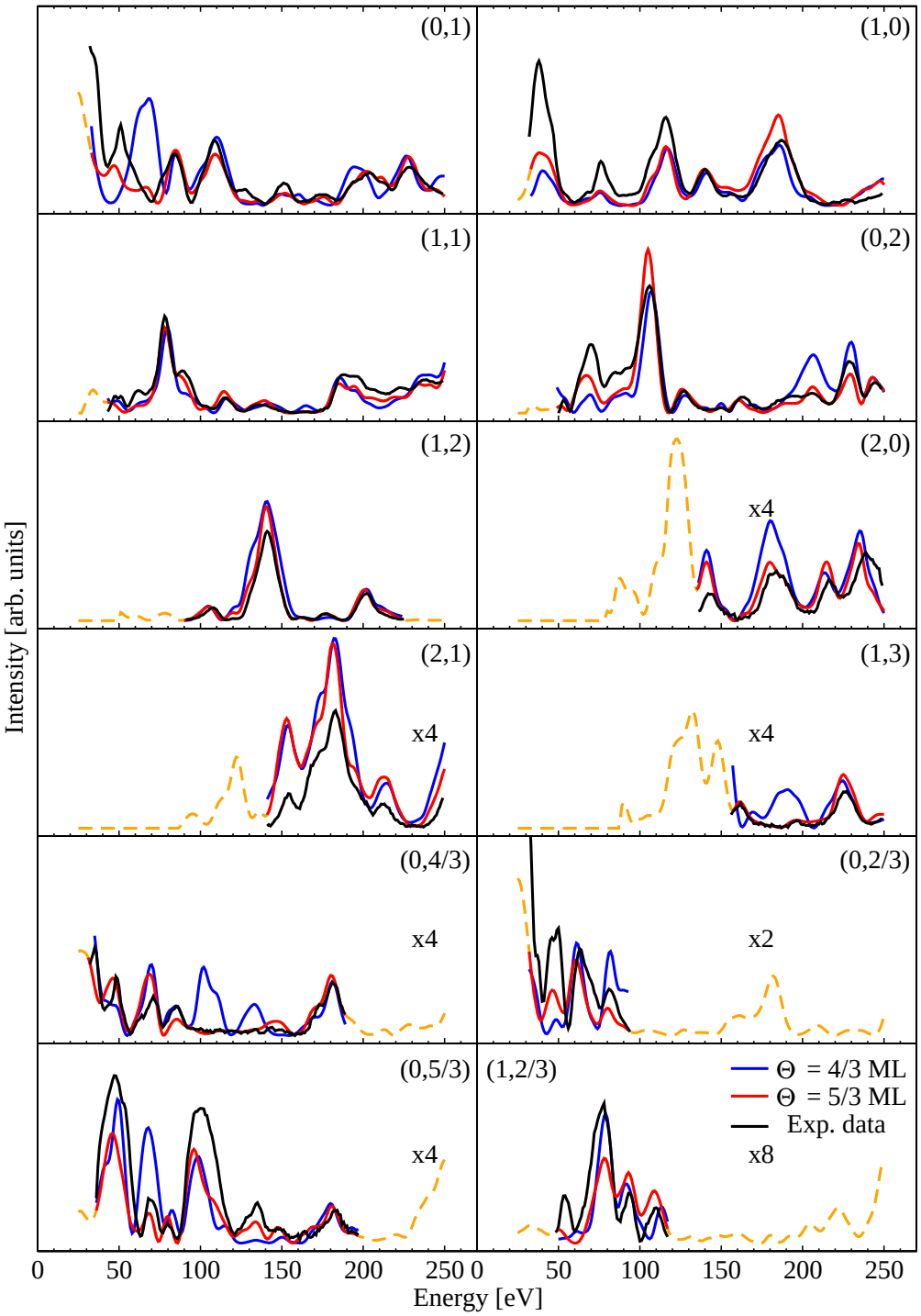

Figure 5.38: LEED-I,V curves for models (A) and (B) with $\frac{4}{3}$ and $\frac{5}{3}$ ML coverages. The extended calculation for structure (B) with $\Theta = \frac{5}{3}ML$ is plotted in orange dashes.

Distance	Reference value	Best fit value for (B)
Vertical displacements [Å]		
d_{12}	0.83	0.73
b_1	0.00	0.03
d_{23}	1.73	1.72
b_2	0.00	0.02
d_{34}	0.76	0.73
b_3	0.00	0.02
d_{bulk}	1.53	1.50
Horizontal displacements [Å]		
$a_{1,2}$	4.456	4.636
$a_{4,5}$	4.456	4.116
$a_{6,7}$	4.456	4.356
$a_{10,11}$	4.456	4.436

Table 5.16: Optimised geometrical displacements for the Au(1×3) structure (B).

The optimised thermal vibrational amplitudes for both structures are summarised in Table 5.15. These optimised thermal vibrations result from the minimisation of the Pendry *R*-factor simultaneously with the geometrical displacements. The υ_i values are a solid indicator for the credibility of the optimised structures and can thus help ruling out the incorrect ones. Nevertheless, the "best fit" values are to be more taken as a plausible estimation rather than an accurate value. We estimate that a variation of up to ± 0.02 Å per atom and per iteration doesn't affect the fit. Here, too, another argument stands against structure (A). That is the very low thermal vibrational amplitude, $\nu(\mathrm{Au}^{(1)})$= 0.02 Å, characterising the topmost Au atom.

The Debye temperature for the topmost Au layer can directly be deduced from the van Hove interpolation in the appendix (Figure 9.6 on page 148), and has a value $\Theta_D = 185(\pm 15)\,K$. Au atoms in the layer below are inequivalent, the Debye temperature characterising atom $\mathrm{Au}^{(3)}$ is $\Theta_D = 425(\pm 60)\,K$, whereas it has a value $\Theta_D = 240(\pm 20)\,K$ for atoms $\mathrm{Au}^{(4,5)}$. This difference can be explained by the fact that the trough created by the missing row in structure (B), Figure 5.37, leaves atoms $\mathrm{Au}^{(4,5)}$ with a lower coordination[20] in comparison to that of atom $\mathrm{Au}^{(3)}$. In Table 5.16 we show that the shortest

[20]In structure (B) in Figure 5.37, the atom $\mathrm{Au}^{(3)}$ is surrounded by 6 atoms from a two-dimensional

interlayer distance $Au^{(1,2)} - A^{(3)} = 0.73(\pm 0.02)$ Å, while atoms $Au^{(4,5)}$ are by 0.03 Å deeper than $Au^{(3)}$. On the other hand, the distance between atoms $Au^{(1)}$ and $Au^{(2)}$ in the y direction, $a_{1,2} = 4.636$ Å, is by 4% larger than the pseudomorphic unit mesh, which gives account of a repulsive interaction between the two Au atoms in the ridge. This is accompanied by a flattening of the Au topmost rows, which is illustrated by a difference of 10% in the Au-Au interlayer distance between the (1×3) and the (1×1) phase. The flattening of the topmost Au rows (atoms $Au^{(1,2)}$) acts as a driving force that brings trough atoms $Au^{(4,5)}$ closer to each other. This manifests itself by the calculated distance, $a_{4,5} = 4.12(\pm 0.02)$ Å, which is by 7.6% smaller than the pseudomorphic value.

The topmost Re layer also exhibits a lower thermal vibrational amplitude for atom $Re^{(8)}$ in comparison with that of atoms $Re^{(6,7)}$. This can be interpreted as a direct consequence to the relaxation sustained by atoms $Au^{(4,5)}$ in the z direction ($d(Au^{(4,5)}$-$Re^{(8)}) = d(Au^{(3)}$-$Re^{(6,7)})+0.03$ Å. The Debye temperature associated with $Re^{(8)}$ is around $680(\pm 100)\,K$, while for atoms $Re^{(6,7)}$ it fluctuates around $380(\pm 40)\,K$. The fourth Re layer is characterised by a homogeneous vibrational amplitude, which corresponds to $\Theta_D \sim 520(\pm 98)\,K$. Additionally, atom $Re^{(9)}$ is located by 0.02 Å deeper than atoms $Re^{(10,11)}$. All these displacements are illustrated by a rough schematisation, *cf.* Figure 5.39.

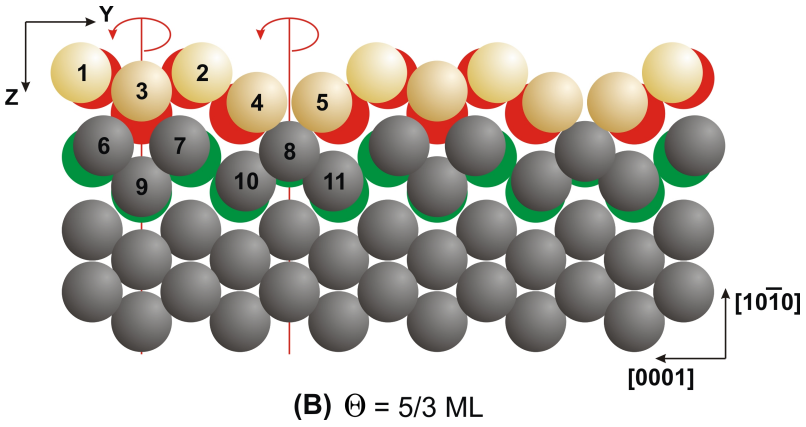

Figure 5.39: Side view of Au and Re atomic displacements in Au(1×3) structure (B). The pseudomorphic positions are indicated by red and green discs.

Concerning the lateral displacements, we note that atoms $Re^{(6,7)}$, in the third layer, undergo a slight compression of about 2.2%, whereas atoms $Re^{(10,11)}$ hardly leave their

perspective, while each of atoms $Au^{(4,5)}$ are surrounded by 5 atoms.

pseudomorphic location and are only by 0.4% closer to each other.

In terms of atomic distances, in the two Au layers, we find $Au^{(1,2)} - Au^{(3)} = 2.80\,(\pm 0.02)\,\text{Å}$ and $Au^{(1')} - Au^{(5)} = Au^{(2)} - Au^{(4)} = 2.66(\pm 0.02)\,\text{Å}$[21]. We recall that in the Au(1×1) phase, the distance $Au^{(1)} - Au^{(2)} = 2.75(\pm 0.02)\,\text{Å}$. In the layer underneath, we find distances $Au^{(3)} - Re^{(6,7)} = 2.79(\pm 0.02)\,\text{Å}$ and $Au^{(4,5)} - Re^{(8)} = 2.70(\pm 0.02)\,\text{Å}$. The distances in the Re layers are also affected in that $Re^{(6,7)} - Re^{(9)} = 2.69(\pm 0.02)\,\text{Å}$ and $Re^{(8)} - Re^{(10,11)} = 2.71(\pm 0.02)\,\text{Å}$. The distance to the bulk is found to be $d_{bulk} = 1.50(\pm 0.02)\,\text{Å}$ with atom $\text{Re}^{(9)}$, the deepest one, as a reference, the buckling in the fourth Re layer increases d_{bulk} to $1.52(\pm 0.02)\,\text{Å}$.

The Au(1×4) Phase

Upon increasing the Au coverage beyond $\Theta = \frac{5}{3}\,ML$, the (1×3) fractional-order LEED spots become elongated in [0001] direction, gradually shift, and eventually split until they reach the quarter positions and form a well-developed (1×4) structure, see Figure 5.40. While they coexist, (1×4) domains grow at the expense of the (1×3) domains and the diffraction pattern can be considered a linear superposition of domains with various lengths, a situation described *e.g.* by Ertl and Küppers [16].

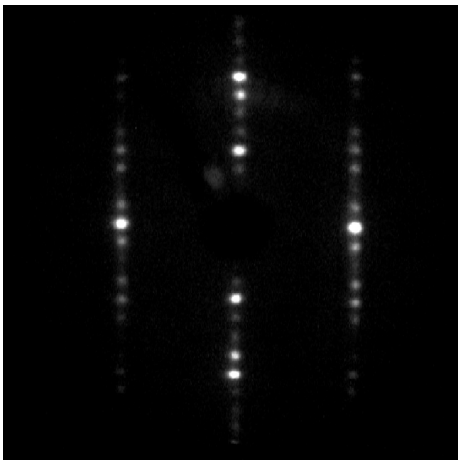

Figure 5.40: Au/Re(10$\bar{1}$0) (1×4) LEED pattern.
Measured at an room temperature with an electron energy of $E_e = 79\,eV$ [33].

In the beginning of section 5.4.2.2 we discussed structure models of the (1×3) phase and pointed out that the real-space structure could be described by a model with

[21] $\text{Au}^{(1')}$ is the atom equivalent to $\text{Au}^{(1)}$, and is located above and at the right of $\text{Au}^{(5)}$ in Figure 5.39.

$\Theta_{Au} = \frac{4}{3} ML$ or by a model with $\Theta_{Au} = \frac{5}{3} ML$. Both the R_P-factors (0.31 and 0.21, respectively) and the thermal vibrational amplitudes were in favour of the latter model (with the (1×1)-like Au bilayers interrupted only by a single missing row). It is therefore reasonable to transfer the "single missing-row" principle also to the Au(1×4) phase. The consequence of this is that the minimum coverage for the (1×4) phase should exceed $\Theta_{Au} = \frac{5}{3} ML$, confirmed for the (1×3) structure.

In order to verify this assumption and to corroborate the hypothesis of a "single missing-row" in the Au(1×n) structures an additional experimental I,V data set for the Au(1×4) phase has been considered. Unfortunately, due to the limited visibility of the fractional-order spots, only a rather small electron energy range of $10-100\,eV$ was accessible. Regardless of this restriction, the theoretical I,V calculations for the two possible models, with $\Theta = \frac{6}{4} ML$ (double missing rows in $[12\bar{1}0]$ direction) and $\Theta = \frac{7}{4} ML$ (single missing row) were performed, see Figure 5.41.

The optimisation of the Au(1×4) phase by means of TensErLEED yielded a total Pendry R-factor, $R_P = 0.44$, for structure (A), with a *local* coverage $\Theta = \frac{6}{4} = 1.5 ML$. More precisely, the R_P-factor for integer spots was $R_{integ} = 0.27$ and $R_{frac} = 0.59$ for the fractional-order ones, whereas for the structure model (B), $\Theta = \frac{7}{4} = 1.75 ML$, convergence is reached for $R_P = 0.40$ ($R_{integ} = 0.24$ and $R_{frac} = 0.55$).

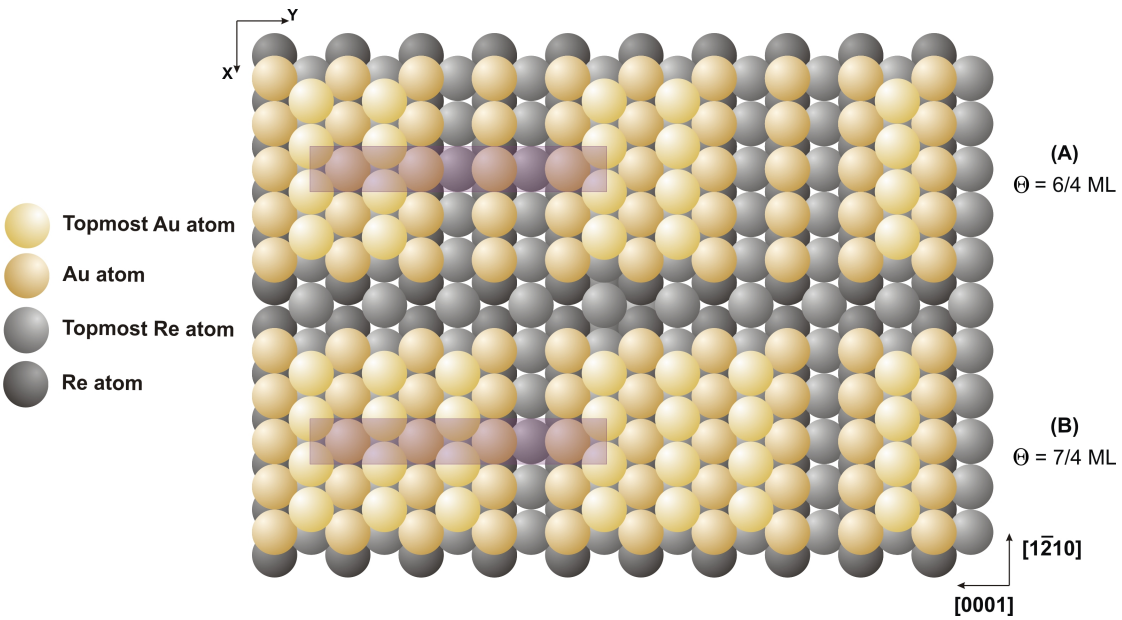

Figure 5.41: Ball models representing the two possible Au(1×4) structures.

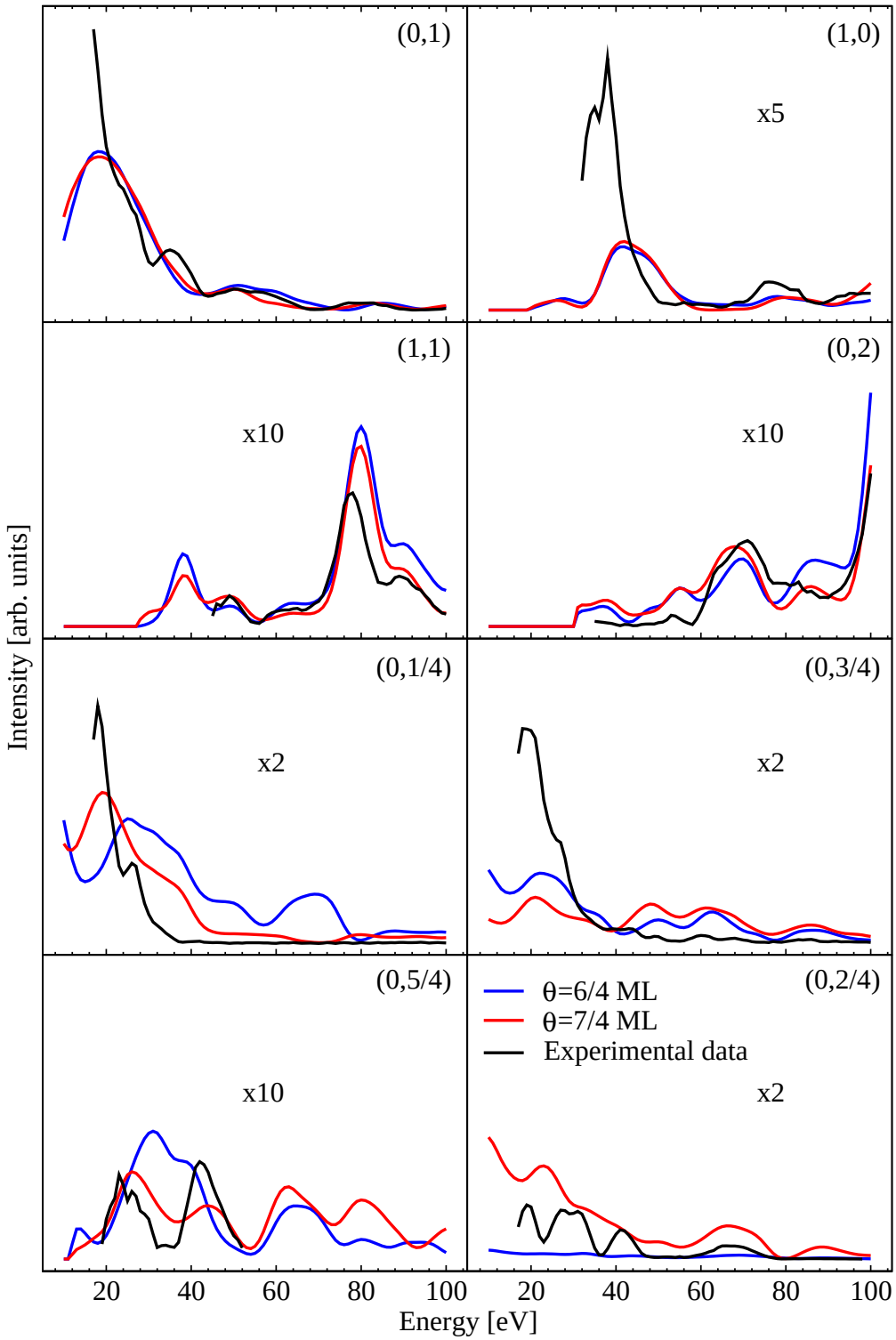

Figure 5.42: LEED-I,V curves for models (A) and (B) with coverages $\frac{6}{4}$ and $\frac{7}{4}ML$.

At this point, it is difficult to settle the matter for structure (B) given that our data set only has a width $\triangle E = 559\,eV$, which makes the statistical error, $var(R_P) = 0.40\sqrt{\frac{40}{559}} = 0.1$. This may be considered somewhat too large to rule out structure (A) with a value of 0.44. This can also be seen from Figure 5.42, where it is obvious that the fairly limited quality of the data prevents the obtention of R_P-factors as low and conclusive as those found, for instance, for the (1×1) and the (1×3) phases. Still, we rely on the visualisation of the spectra, which shows an almost inexistent intensity in the (0,2/4) beam concerning model (A). Moreover, structure (A) exhibits two distinct peak discrepancies in the region between 50 and 80 eV in beam (0,1/4). This gives a slight but relevant advantage to the (1×4) structure (A) with a single missing row as expected for the logical phase sequence: (1×3)→(1×4) with a *local* coverage $\Theta = \frac{7}{4}ML$.

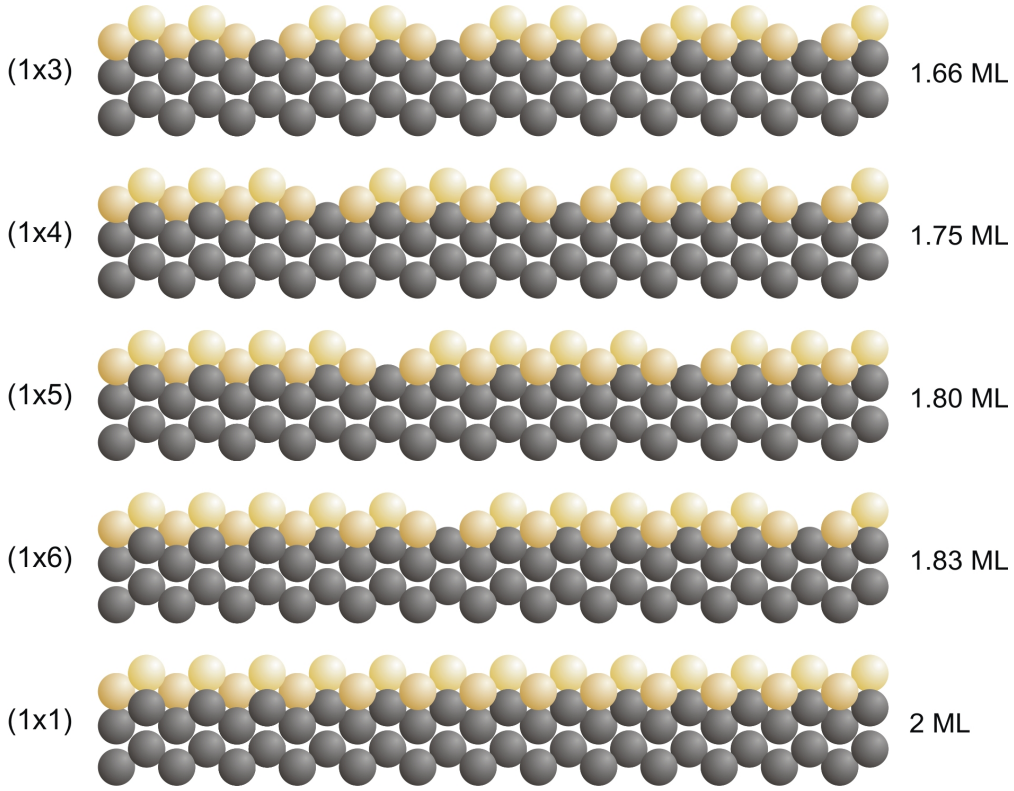

Figure 5.43: Growth sequence of Au on the Re(10$\bar{1}$0) surface .

We admit that the structural parameters for the Au(1×4) phase could only be calculated coarsely due to the scarcity of data points. Nevertheless, our calculations can certainly serve as a starting point for further experimental investigations on this system

and might even help understand coverage-dependent structural developments of similar systems. The structural parameters used for the reference calculations on the Au(1×4) phase are presented in Tables on page 102 and 5.11 on page 103, because the same values as for the Ag(1×4) phase were used.

In a previous experimental investigation of the system Au/Re(10$\bar{1}$0) the double "missing-row" model was applied to the (1×3) and (1×4) phases with *local* coverages of $\Theta^{(1\times3)} = \frac{4}{3}$ and $\Theta^{(1\times4)} = \frac{6}{4}$, respectively [34]. The LEED analysis of the respective I,V curves provided in the present work led, however, to somewhat higher *local* coverages of $\frac{5}{3} = 1.66\,ML$ and $\frac{7}{4} = 1.75\,ML$. Hence, at higher coverages gold phases with increasing n (5 and 6) would then correspond to *local* coverages of $\frac{9}{5}$ and $\frac{11}{6}\,ML$ until the (1×1) bilayer is reached at $2\,ML$. This can be illustrated by the expression $\Theta^{(1\times n)}(n) = \frac{(2n-1)}{n}$, for $n \geqslant 3$, and in Figure 5.43, where the Au growth is shown as a sequence of single missing-rows structures, in which, with increasing coverage, the distance between the single missing-rows is increasing.

Note that thus, the present work proves the original coverage assumptions based merely upon deposition times and constant deposition rates, *i.e.* $\Theta^{(1\times3)} = \frac{4}{3}\,ML$ and $\Theta^{(1\times4)} = \frac{6}{4}\,ML$, to be erroneous: The real space structures for the Au(1×3) and (1×4) phases are found to be in both cases structure (B), see Figures 5.36 on page 118 and 5.41 on page 125.

Chapter 6

Conclusions

The investigation of the (1×1) LEED structures of Cu, Ag, and Au on the Re(10$\bar{1}$0) surface revealed that the three metals follow the morphology determined by the Re substrate, *i.e.* the Re crystal directs the adsorbate growth. Nevertheless, the three deposited metals exhibit differences due to their atomic size. Only the relatively small Cu, with a negative lattice misfit, grows seemingly strain-free in bilayered islands, without forming any long-range ordered superstructures. The investigation of experimental I,V curves for Cu at higher coverages, $1\,BL < \Theta_{Cu} \leq 2.5\,BL$, showed that Cu continues to grow bilayer-wise, thereby retaining the Re hcp morphology. Atomic distances could be determined for up to $4\,ML$ of Cu with decreasing accuracy. The corresponding (1×1) LEED pattern was in fact observed even for Θ_{Cu} exceeding $8\,ML$, but accompanied by a pronounced increase in the diffuse scattering background [38]. Ag and Au, on the other hand, appear to compensate the strain due to their positive lattice misfit by the formation of commensurate missing-row superstructures. Still, these two elements clearly differ from each other, and even though the Ag radius is slightly bigger than that of Au, this does not suffice to explain the observed dissimilarities: Au forms domains, whereby strain is relieved by the adjustment of the distance between missing rows according to the amount of deposited material. Therefore, the local coverage changes with the global one, giving rise to the observed series of (1×n) superstructures. This hints to the formation of larger scale domains opposing to smaller Ag (and Cu) $2D$ islands. In contrast to this, Ag adapts to changes in the global coverage by adjusting the ratios between its two (1×4) domains with different, but constant, local coverages and uncovered Re patches. This strategy seems to be less successful at higher coverages, causing Ag to grow not as homogeneously and fill higher layers before the first bilayer is completed. In the case of Au films, a very low R_P-factor was obtained for the bilayer, pointing

out that it is closed before higher layers are populated. Therefore, only Cu and Au show a real Stranski-Krastanov growth behaviour, whereas Ag tends more towards the so-called simultaneous-multilayer (SM) growth mode. Additional future TPD measurements for Au/Re($10\bar{1}0$) should clarifiy this aspect. Furthermore, Ag is the only one of the three metals to exhibit a temperature-driven order-order phase transition. The sub-bilayer (1×4) phase reversibly turns upon heating into a c(2×2) phase, that only exists at elevated temperatures.

The formation of two-dimensional islands due to fairly strong attractive mutual interactions between the atoms in each of the three metallic films, leads to major difficulties in the unequivocal determination of surface coverages based merely upon LEED superstructures, because of the discrepancies between the *global* and the *local* coverages. In the case of the Ag(1×4) phase, this aspect is further complicated, as the LEED pattern observed in a broad coverage range does not originate from a single homogeneous layer, but from the combination of two coexisting island domain structures with (1×4) periodicity alongside remaining uncovered Re patches. This means that, interestingly, the (1×4) phases formed by both Ag and Au are similar but physically not identical! Again, this nuance can not be related to differences in their atomic diameters, but only to the differences in their electronic structures. In this respect, further experimental investigations of these systems by, *e.g.,* electron spectroscopies (angle-resolved ultraviolet photoelectron spectroscopy (ARUPS), near edge X-ray absorptiom fine-structure (NEXAFS) measurements, etc.) or X-ray diffraction are desirable. One example of this kind is provided by the field emission study of silver on rhenium by Al-Rawi and Jones [1]. More insight could, of course, be gathered by quantum-chemical calculations of metal-on-metal systems using, *e.g.*, density functional theory. Unfortunately, studies of this kind are so far relatively scarce.

The experimental research work of C. Pauls and V. Scherf has provided insight as to how the growth and phase formation of metallic films on a chemically active transition metal surface like Re can be affected by coadsorption of reactive gases such as carbon monoxide. In his thesis work [33] Pauls has shown that the Au(1×3) phase formed on the Re($10\bar{1}0$) surface can undergo a compression to a (1×4) or even a (1×5) phase by the $2D$ spreading pressure exerted by coadsorbing CO. Likewise, Scherf [44] could not rule out that the phase transition (1×4)$\leftrightarrow$c(2×2) might be driven by CO coadsorption and desorption. CO exposure to the Re($10\bar{1}0$) surface at $500\,K$ exclusively yields the dissociated species C and O, as was deduced from the respective high-temperature desorption states (with desorption energies ranging from$185\,kJ/mol$ to $210\,kJ/mol$) exhib-

iting second-order reaction kinetics, and the formation of a sharp (1×2) LEED pattern with maximum brightness at $\Theta_{CO} = 0.25\,ML$ ($\Theta_C + \Theta_O = 0.5\,ML$) [35]. This supports the idea that strongly bound chemisorbed C and O atoms compete with Ag as they do with Au for adsorption sites on the Re surface (in the case of Cu, no influence of CO was observed). In this respect, the occurrence of the CO-induced (1×2) LEED superstructure is an important experimental observation, and its structural analysis is highly desirable. Therefore, in addition to the theoretical work on the metal/Re systems, LEED-I,V curves for the CO(1×2) phase have been measured for 21 different integer- and fractional-order beams in the energy range $40-370\,eV$, see Appendix on page 142. Unfortunately, it was not yet possible to elucidate the real-space structure, even though a large number of reference models were tested. Therefore, these data remain as a challenging task for a future TensErLEED analysis.

Chapter 7

Summary

This thesis deals with the computational surface determination of various long-range ordered phases formed by thin films of copper, silver, and gold adsorbed on the rhenium-$(10\bar{1}0)$ surface. It is based upon LEED-I,V curves for these phases that were recorded in the course of detailed experimental investigations of the respective films carried out in our group (using techniques such as LEED, MEED, and TPD). In order to solve the intricate puzzle of surface structural analysis, the electron elastic scattering behaviour of the investigated coinage metal phases was calculated using the Erlangen TensErLEED program package. Thereby first a set of theoretical LEED-I,V curves is derived for a guessed reference structure. Subsequently its structural input parameters are varied in a trial-and-error procedure until optimal agreement between experiment and theory is attained. The (1×1) phases formed by the deposited metals were tackled first to establish an absolute coverage calibration and to elucidate the respective growth modes on the Re$(10\bar{1}0)$ surface. In all three cases the (1×1) structure is developed best at a coverage $\Theta_{Cu,Ag,Au} = 2\,ML = 1\,BL$. Extension of the investigation to experimental I,V curves for higher Cu coverages revealed that this element continues to grow bilayer-wise, thereby retaining the Re hcp morphology.

Ag, in contrast to Cu and Au, happens not to grow as homogeneously, and the TPD data suggest that Ag films exhibit the so-called simultaneous-multilayer (SM) growth mode. The following analysis of the sub-bilayer coverage range shows that the three systems exhibit considerable differences. While Cu, having a negative lattice misfit compared to Re, shows no long-range ordered superstructures, Ag and Au with a similar positive misfit form a couple of such phases. Ag features both a (1×4) phase, stable at ambient temperatures, that upon heating transforms into a c(2×2) phase that only exists at elevated temperatures. The structure corresponding to the Ag(1×4) phase could not

be unambiguously resolved. The TensErLEED computations rigorously performed for the two most plausible structures with *global* coverages, $\Theta^{(1\times4)} = 1.25\,ML$ and $1.75\,ML$, did not significantly differ in the Pendry *R*-factor. Yet, the determination of the c(2×2) phase, occurring at a temperature of $700\,K$, was more successful: The best coincidence between theory and experiment was found for an elongated filled honeycomb-like structure. This structure has the additional advantage that it requires relatively little atomic rearrangement for the transformation into the low-temperature (1×4) phase. The *local* coverage $\Theta^{c(2\times2)} = 1.5\,ML$ of the c(2×2) structure defines the *global* coverage limits within which the reversible phase transition c(2×2)↔(1×4) takes place. From this, we could deduce that the (1×4) phase consists of a combination of domains with the two possible structures, consistent with previous STM observations.

A third scenario is provided by Au. In the experiments, with increasing coverage a series of (1×n) LEED superstructures with n= $\{3,4,5,6\}$ is observed independent of the temperature. The series ends with the aforementioned (1×1) phase at the bilayer coverage. The Au(1×n) structure sequence could be elucidated fully by a thorough analysis of just the (1×3) phase. This structure consists of a pseudomorphous Au bilayer in which every third row of the topmost layer is replaced by a missing-row. The higher (1×n) structures are then formed by omitting every n^{th} row. In this way, the system is able to compensate the elastic strain caused by the lattice misfit between Au and Re.

All in all, the structural analyses carried out in the present thesis work have successfully provided answers to various open questions that arose from previous work performed in our group on the adsorption and growth of Cu, Ag, and Au films on Re and Ru surfaces alike.

Chapter 8

Zusammenfassung

Die hier vorgelegte Doktorarbeit beschäftigt sich in der Hauptsache mit der quantitativen Strukturbestimmung von ferngeordneten Kupfer-, Silber- und Goldfilmen, die während der Adsorption dieser Metalle auf einer Rhenium$(10\bar{1}0)$-Oberfläche gebildet werden. Im Zuge der experimentellen Arbeiten an diesen Systemen innerhalb unserer Arbeitsgruppe (hauptsächlich mittels LEED, MEED und TPD) wurden auch sogenannte LEED-I,V-Kurven aufgezeichnet, welche die Oberflächenstrukturinformation beinhalten. Um aus der Menge der möglichen Oberflächenstrukturen die tatsächliche herauszufinden, wurde im Rahmen dynamischer Elektronenstreurechnungen das Streuverhalten der untersuchten Phasen mit Hilfe des Erlangener TensErLEED-Programmpaketes berechnet. Jede anfängliche Referenzstrukturannahme führt dabei zu einem Satz von charakteristischen LEED-I,V-Kurven. Daraufhin werden durch eine Suchroutine die Struktureingangsparameter so lange systematisch variiert, bis die bestmögliche Übereinstimmung zwischen experimentellen und berechneten LEED-I,V-Kurven erreicht ist. Zunächst wurden in dieser Weise die (1×1)-Phasen aller drei Metalle behandelt. Dies ermöglichte es, einerseits eine Kalibrierung der quantitativen Oberflächenbedeckungsgrade und anderseits Informationen über die Art des Filmwachstums zu erhalten. In allen drei Fällen sind die (1×1)-Phasen dann am besten ausgebildet, wenn eine Bedeckung $\Theta_{Cu,Ag,Au} = 2\,ML = 1\,BL$ (Monolagen, Bilage) erreicht ist. Die genaue Analyse von I,V-Daten bei höheren Bedeckungsgraden zeigt, daß Cu weiter in Bilagen aufwächst und dabei zunächst die Re-hcp-Struktur beibehält.

Im Gegensatz zu Cu und Au wachsen Ag-Filme deutlich weniger homogen auf, sondern unterliegen dem sogenannten simultanen Multilagenwachstum. Im Bereich unterhalb der geschlossenen ersten Bilage weisen die drei betrachteten Metallfilme erhebliche strukturelle Unterschiede auf. Das im Vergleich mit Re kleinere Cu bildet keiner-

lei Überstrukturphasen. Dagegen beobachtet man beim größeren Ag zwei geordnete LEED-Strukturen, eine (1×4)- und – bei höheren Temperaturen – eine c(2×2)-Phase, die beim Heizen aus der (1×4)-Struktur entsteht. Die Ag-(1×4)-Phase läßt sich nicht eindeutig durch eine einzelne Struktur erklären. Die TensErLEED-Rechnungen für die beiden plausibelsten Oberflächenstrukturen, mit den *globalen* Bedeckungsgraden von $\Theta^{(1\times4)} = 1.25\,ML$ bzw. $1.75\,ML$, unterschieden sich im Hinblick auf den Pendry-*R*-Faktor – ein Maß für die Güte der Übereinstimmung zwischen Experiment und Theorie – nicht signifikant. Eindeutig war hingegen die Strukturbestimmung der c(2×2)-Phase, die bei $700\,K$ auftritt. Es wurde eine dem Re-Substrat gemäß in einer Richtung gestauchte, gefüllte Honigwaben-Atomanordnung gefunden. Der Vorteil dieser Struktur ist, daß verhältnismäßig wenige Diffusionsschritte erforderlich sind, um daraus eine der beiden möglichen (1×4)-Phasen zu bilden und umgekehrt. Der *lokale* Bedeckungsgrad der c(2×2)-Phase von $\Theta^{c(2\times2)} = 1.5\,ML$ definiert gleichzeitig den Bereich der *globalen* Bedeckungsgrade, innerhalb dessen der reversible Phasenübergang c(2×2)↔(1×4) auftritt. Daraus ergibt sich, daß die (1×4)-Phase eine Kombination von Domänen mit den zwei möglichen Strukturen ist. Dies ist in Übereinstimmung mit vorhergehenden STM-Untersuchungen.

Ein drittes Szenario zeigen die Au-Filme, die – unabhängig von der Temperatur – im Subbilagenbereich mit steigender Bedeckung eine Reihe von (1×n)-Strukturen mit n= 3, 4, 5, und 6 bilden. Sobald die Bilage geschlossen ist, findet man dann die bereits erwähnte pseudomorphe (1×1)-Phase. Mit Hilfe der hier durchgeführten LEED-Rechnungen konnte die Strukturesequenz der (1×n)-Phasen insoweit aufgeklärt werden, als das Bauprinzip der zuerst auftretenden (1×3)-Phase berechnet und dann auf die (1×4)-, (1×5)- und (1×6)-Phasen übertragen wurde. Die (1×n)-Strukturen sind so aufgebaut, daß ausgehend von der Bilage jede n-te Reihe in der oberen Atomlage ausgelassen wird. Auf diese Weise können elastische Spannungen, die eine Folge der positiven Gitterfehlanpassung des Au sind, ausgeglichen werden.

Insgesamt haben die Strukturanalysen der hier vorgelegten Arbeit erfolgreich zur Beantwortung einer Reihe von offenen Fragen im Zusammenhang mit der Adsorption und dem Wachstum von Cu-, Ag- und Au-Filmen auf der Re(10$\bar{1}$0)-Oberfläche beigetragen.

Bibliography

[1] O.Z. Al-Rawi and J.P. Jones. A Field Emission Study of Silver on Rhenium. *Surface Science*, 124:220–240, 1983.

[2] A. Barbieri and M.A. van Hove. Private Communication (http://electron.lbl.gov/leedpack/).

[3] E. Bauer. Epitaxy of Metals on Metals. *Applications of Surface Science*, 11/12:479–494, 1982.

[4] E. Bauer. *The Chemical Physics of Solid Surfaces and Heterogeneous Catalysis*, volume 3. D.A. King and D.P. Woodruff, 1984.

[5] E. Bauer. Low Energy Electron Microscopy. *Reports on Progress in Physics*, 57, 1994.

[6] G. Binnig and H. Rohrer. Scanning Tunneling Microscopy. *Surface Science*, 126:236–244, 1982.

[7] V. Blum and K. Heinz. Fast LEED Intensity Calculations for Surface Crystallography Using tensor LEED. *Computer Physics Communications*, 134:392–425, 2001.

[8] H. Brune. Strain Relief at Hexagonal-Close-Packed Interfaces. *Surface Science Reports*, 31:121, 1998.

[9] C.T. Campbell. Metal Radii in Surface Science. *Surface Science*, 167:L186–L186, 1986.

[10] S.P. Chen. Anomalous Relaxations of (0001) and $(10\bar{1}0)$ Surfaces in hcp Metals. *Surface Science Letters*, 264:L162–L168, 1992.

[11] K. Christmann. *Introduction to Surface Physical Chemistry*. Springer, 1991.

[12] H.L. Davis and D.M. Zehner. Structure of the Clean Re(10$\bar{1}$0) Surface. *Journal of Vacuum Science and Technology*, 17:190–193, 1980.

[13] C.J. Davisson and L.H. Germer. Diffraction of Electrons by a Crystal of Nickel. *Physical Review*, 30:705–740, 1927.

[14] J.J. de Miguel, A. Cebollada, J.M. Gallego, S. Ferrer, R. Miranda, C.M. Schneider, P. Bressler, J. Garbe, K. Bethke, and J. Kirschner. Characterization of the Growth Processes and Magnetic Properties of Thin Ferromagnetic Cobalt Films on Cu(100). *Surface Science*, 211-212:732–739, 1989.

[15] R. Döll, L. Hammer, K. Heinz, K. Bedürftig, U. Muschiol, K. Christmann, A.P. Seitsonen, H. Bludau, and H. Over. Anomalous Hydrogen Adsorption Sites Found for the c(2x2)-3H Phases Formed on the Re(10$\bar{1}$0) and Re(10$\bar{1}$0) Surfaces. *Journal of Chemical Physics*, 108:8671–8679, 1998.

[16] G. Ertl and J. Küppers. *Low Energy Electrons and Surface Chemistry*. VCH, 1985.

[17] K.D. Gronwald and M. Henzler. Epitaxy of Si(111) as Studied with a New High Resolving LEED System. *Surface Science*, 117:180–187, 1982.

[18] J.J. Harris, B.A. Joyce, and P.J. Dobson. Oscillations in the Surface Structure of Sn-Doped GaAs during Growth by MBE. *Surface Science*, 103:L90–L96, 1981.

[19] M. Henzler. Studies of Surface Imperfections. *Applied Surface Science*, 11/12:450, 1982.

[20] A.F. Holleman and E. Wiberg. *Lehrbuch der Anorganischen Chemie*. 101^{th} edition, 1995.

[21] K.G. Huang and D. Gibbs. Phase Behavior of the Au(111) Surface: Discommensurations and Kinks. *Physical Review Letters*, 65:3313, 1990.

[22] F. Jona, D. Westphal, A. Goldmann, and P.M. Marcus. A Low-Energy Electron Diffraction Intensity Analysis of Cu(001)c(2x2)-Cl. *Journal of Physics C: Solid State Physics*, 16:3001–3010, 1983.

[23] G. Kleinle, W. Moritz, D.L. Adams, and G. Ertl. A Novel Procedure for Fast Surface Structural Analysis Based on LEED Intensity Data. *Surface Science Letters*, 219:L637–L645, 1989.

[24] D.C. Köningsberger and R. Prins. *X-ray Absorption: Principles, Applications and Techniques of EXAFS, SEXAFS and XANES*. 1988.

[25] M. Kottcke and K. Heinz. A New Approach to Automated Structure Optimization in LEED Intensity Analysis. *Surface Science*, 376:352, 1997.

[26] K.O. Legg, F. Jona, D.M. Jepsen, and P.M. Marcus. Determination of the c(2x2) Structure of Sulfur on Fe(001) by Low-Energy Electron Diffraction. *Surface Science*, 64:85–95, 1977.

[27] P. Lenz-Solomun and K. Christmann. The Growth of Silver on a Ruthenium($10\bar{1}0$) Surface. *Surface Science*, 345:41–52, 1996.

[28] L. Liu, T. Takahashi, and W. A. Bassett. Effect of Pressure and Temperature on the Lattice Parameters of Rhenium. *Journal of Physics and Chemistry of Solids*, 31:1345–1351, 1970.

[29] U. Löffler, K. Heinz R. Döll, and J.B. Pendry. Investigation of surface atom vibrations by tensor LEED. *Surface Science*, 301:346–352, 1994.

[30] L.F. Mattheiss. Energy Bands for Solid Argon. *Physical Review*, 331:A1399–A1402, 1964.

[31] J.H. Neave, B.A. Joyce, P.J. Dobson, and N. Norton. Reflection High-Energy Electron Diffraction Oscillations from Vicinal Surfaces. *Applied Physics A*, 31:1–8, 1983.

[32] M. Parschau, D. Schlatterbeck, and K. Christmann. Nucleation and Growth of Silver Films on a Rhenium(0001) Surface: A Combined STM and LEED Study. *Surface Science*, 440:231–251, 1997.

[33] C. Pauls. *Zweidimensionale Kompression von ultradünnen Goldfilmen durch Koadsorption von Kohlenmonoxid auf der Rhenium($10\bar{1}0$)-Oberfläche*. PhD thesis, Freie Universität Berlin, 2011.

[34] C. Pauls and K. Christmann. Growth and Structure of Gold Films on a Re(10$\bar{1}$0) Surface. *Journal of Physics: Condensed Matter*, 21:1–12, 2009.

[35] C. Pauls, D. Przyrembel, and K. Christmann. Dissociation of Carbon Monoxide on the Rhenium(10$\bar{1}$0) Surface. *Journal of Physical Chemistry B*, 108:14749–14758, 2004.

[36] J.B. Pendry. *Low Energy Electron Diffraction*. Academic Press, 1974.

[37] J.B. Pendry. Reliability Factors for LEED Calculations. *Journal of Physics C: Solid State Physics*, 13:937–44, 1980.

[38] D. Przyrembel. Private Communication.

[39] D. Przyrembel. *Wechselwirkungen von Kupfer mit einer Rhenium(10$\bar{1}$0)-Oberfläche*. Diploma thesis, Freie Universität Berlin, 2010.

[40] E. Purushotham and N. Gopi Krishna. Mean Square Amplitudes of Vibration and Associated Debye Temperatures of Rhenium, Osmium and Thallium. *Physica B: Condensed Matter*, 405:3308–3311, 2010.

[41] M.W. Roberts and C.S. McKee. *Chemistry of the Metal Gas Interface*. Clarendon Press, 1978.

[42] P.J. Rous and J.B. Pendry. Tensor LEED I: A Technique for High Speed Surface Structure Determination by Low-Energy Electron Diffraction. TLEED1. *Computer Physics Communications*, 54:137, 1989.

[43] P.J. Rous, J.B. Pendry, D.K. Saldin, K. Heinz, K. Müller, and N. Bickel. Interface Structure of Ultrathin CoSi2 Films Epitaxially Grown on Si(111). *Physical Review Letters*, 57, 1986.

[44] V. Scherf. *Adsorption von Silber an einer Re(10$\bar{1}$0)-Oberfläche*. PhD thesis, Freie Universität Berlin, 2012.

[45] D. Schlatterbeck, M. Parschau, and K. Christmann. Silver Films Grown on a Rhenium(0001) Surface: a Combined TDS, XPS, and $\Delta\Phi$ Study. *Surface Science*, 418:240–255, 1998.

[46] C.M. Schneider, P. Bressler, P. Schuster, J. Kirschner, J.J. de Miguel, and R. Miranda. Epitaxy and Magnetic Properties of fcc Cobalt Films on Cu(lO0). *Vacuum*, 41:503–505, 1990.

[47] J.C. Slater. Wave Functions in a Periodic Potential. *Physical Review*, 51:846–851, 1937.

[48] G.A. Somorjai. *Chemistry in Two Dimensions: Surfaces*. Cornell University Press, 1981.

[49] J. Thomassen, B. Feldmann, and M. Wuttig. Growth, Structure, and Morphology of Ultrathin Iron Films on Cu(100). *Surface Science*, 264:406–418, 1992.

[50] W.R. Tyson and W.A. Miller. Surface Free Energies of Solid Metals - Estimation from Liquid Surface Tension Measurements. *Surface Science*, 62:267–276, 1977.

[51] D. v. Gemünden and H. Stamm. *"AUTOLEED Programm-Dokumentation, V. 1.20/1.30/ 1.35"*. Inst. f. Angewandte Physik der Universität Erlangen-Nürnberg, Erlangen, 1989.

[52] J.H. van der Merwe. Analytical Selection of Ideal Epitaxial Configurations and Some Speculations on the Occurrence of Epitaxy. *Philosophical Magazine A*, 45:127–143, 1982.

[53] M.A. van Hove, W. Moritz, H. Over, P.J. Rous, A. Wander, A. Barbieri, N. Materer, U. Starke, and G.A. Somorjai. Automated determination of complex surface structures by LEED. *Surface Science Reports*, pages 19–191, 1993.

[54] M.A. van Hove and S.Y. Tong. *Surface Crystallography by LEED*. Springer, 1979.

[55] M.A. van Hove, S.Y. Tong, and M.H. Elconin. Surface Structure Refinements of 2H-MoS_2, 2H-$NbSe_2$ and W(l00)p(2x1)-O via New Reliability Factors for Surface Crystallography. *Surface Science*, 64:85–95, 1977.

[56] M.A. van Hove, W.H. Weinberg, and C.M. Chan. *Low Energy Electron Diffraction*. Springer, 1986.

[57] A. Vollmer. *Wachstum und Struktur von dünnen Silber- und Goldfilmen auf einer Rhenium($10\bar{1}0$)-Oberfläche*. PhD thesis, Freie Universität Berlin, 1999.

[58] R. Wagner. *Edelmetalle auf Rhenium-Oberflächen*. PhD thesis, Freie Universität Berlin, 2002.

[59] R. Wagner, D. Schlatterbeck, and K. Christmann. The Interaction of Copper with a Rhenium(0001) Surface: Structure, Energetics, and Growth Modes. *Surface Science*, 440:231–251, 1999.

[60] A. Weingart. *Morphologie und Wachstum von dünnen Kupfer- und Goldfilmen auf einer Rhenium(0001)-Oberfläche*. PhD thesis, Freie Universität Berlin, 2003.

[61] P. Wissmann. *Thin Metal Films and Gas Chemisorption*, volume 32. Elsevier, 1987.

[62] E.A. Wood. Vocabulary of Surface Crystallography. *Journal of Applied Physics*, 35:1306–1312, 1964.

[63] H. Wormeester, M.E. Kiene, E. Hüger, and E. Bauer. Growth of hcp Cu on W(100). *Surface Science*, 377-379:988–991, 1997.

[64] M. Wuttig, C.C. Knight, T. Flores, and Y. Gauthier. LEED Structure Determination of Two Ordered Alloys: Cu(100)-c(2x2)Mn and Ni(100)-c(2x2)Mn. *Surface Science*, 292:189–195, 1993.

[65] E. Zannazzi and F. Jona. Atomic arrangement in the c(2x2) structure of Cl on Ag(100). *Physical Review B*, 14:432–440, 1976.

[66] E. Zannazzi and F. Jona. Reliability Factor for Surface Structure Determinations by Low-Energy Electron Diffraction. *Surface Science*, 62:61–80, 1977.

Chapter 9

Appendix

Carbon Monoxide on Rhenium($10\bar{1}0$)

Molecular and dissociative adsorption of CO on the Re($10\bar{1}0$) surface occur at low and high temperatures, respectively [35]. Dissociated CO shows two LEED superstructures: a lower coverage c(2×4) phase and a higher coverage (1×2) phase.

The c(2×4) is only faintly visible, that is why only I,V spectra for the (1×2) phase could be measured. The experiment shows that the c(2×4) phase has half the coverage of the (1×2): $\Theta_{c(2\times4)} = \frac{1}{2}\Theta_{(1\times2)}$.

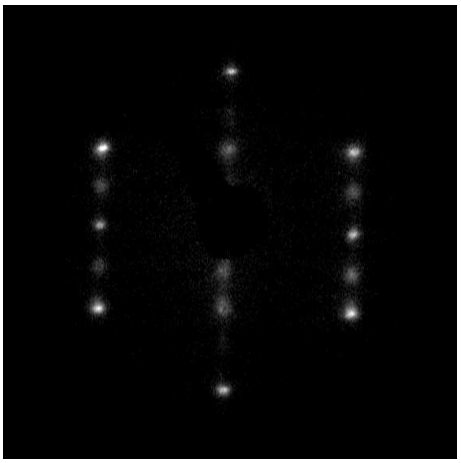

Figure 9.1: CO(1×2) LEED pattern at $T = 135\,K$.

The thermal desorption of the molecular α-states is complete at $500\,K$ and that of the dissociative β-states doesn't begin below $550\,K$, therefore the preparation of the (1×2)

structure was done *at* $500\,K$.

The experimental procedure consists in the following steps:

- Oxidative cleaning at $T = 1200\,K$, followed by flash-heating up to $1800\,K$ until a well-defined high-contrast LEED (1×1) pattern of clean Re is observed.
- Cooling the sample down to $130\,K$ with liquid nitrogen.
- Flash-heating the sample up to $1200\,K$ to remove all the CO adsorbed during cooling.
- Adsorbing CO at $200\,K$, offering a dosis of $4\,L$.
- Heating up to $500\,K$ to desorb all molecular CO and dissociate the remaining CO.
- Offering $1\,L$ of CO at $500\,K$ to ensure the surface is completely filled with dissociated CO. The surface was held at $500\,K$ for $5\,min$.

This leads to a well-ordered (1×2) phase with high contrast. The LEED-I,V curves were measured at low temperature (N_2 cooling). The residual gas pressure in the chamber during measurements was: $\mathrm{p} = 2.0\times10^{-10}\,mbar$.

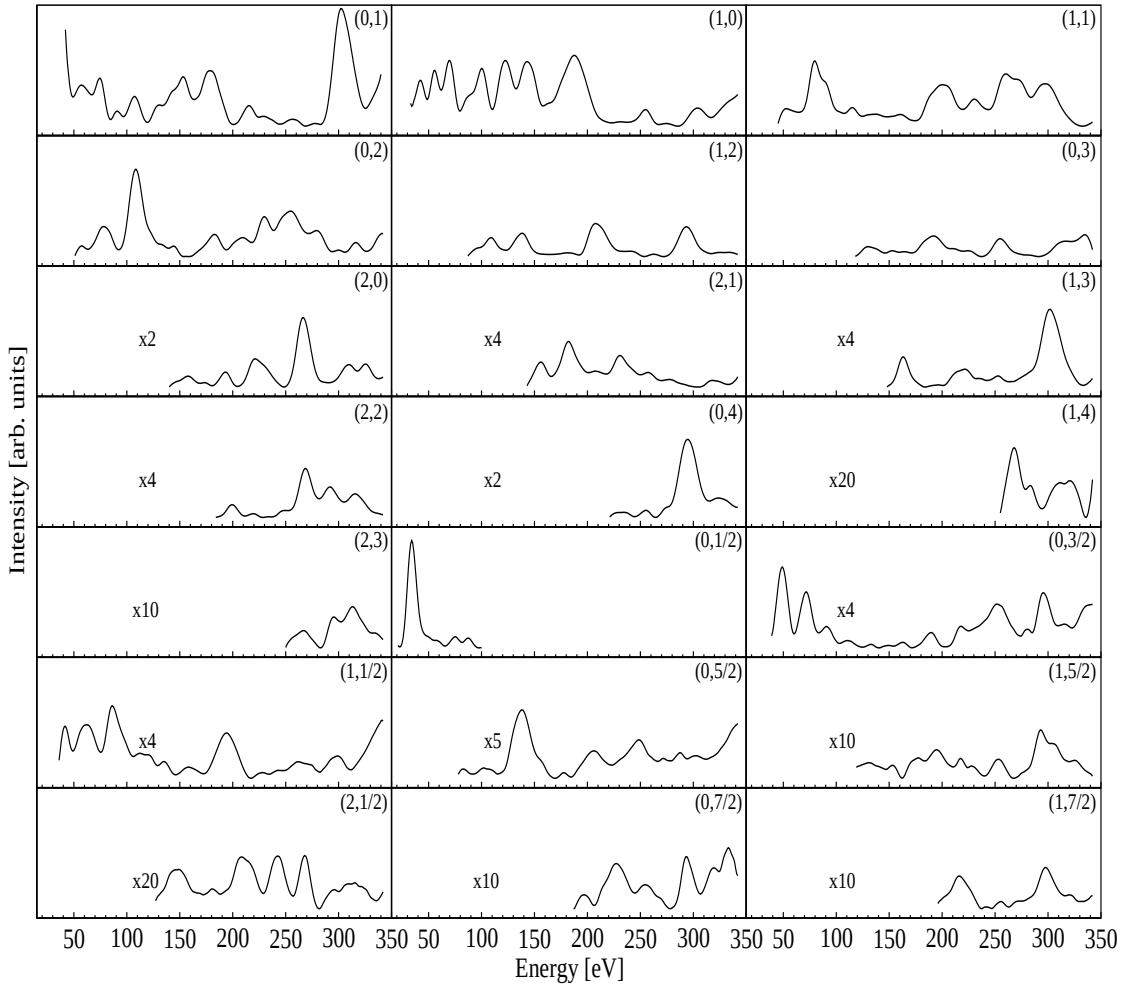

Figure 9.2: Experimental LEED-I,V curves for the CO(1×2) phase.

Thermal Vibrational Displacements

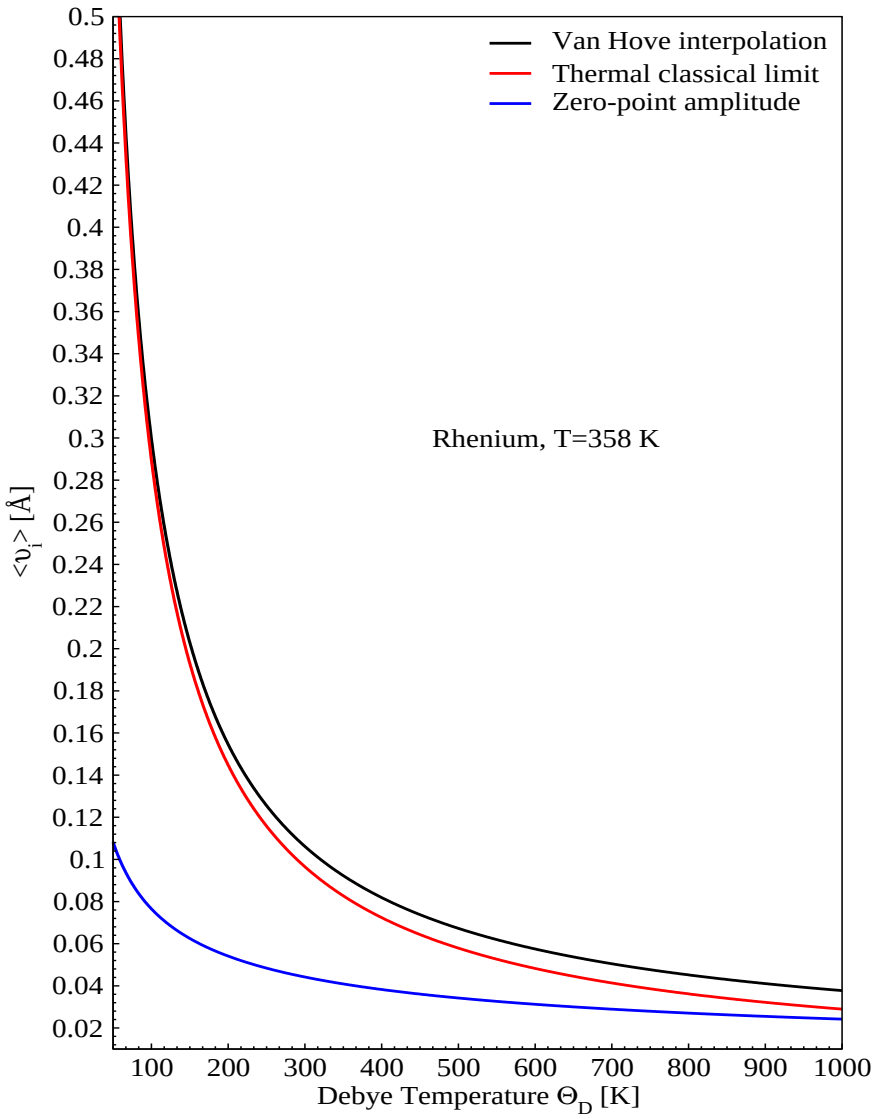

Figure 9.3: RMS displacement of Re atoms as a function of the Debye temperature

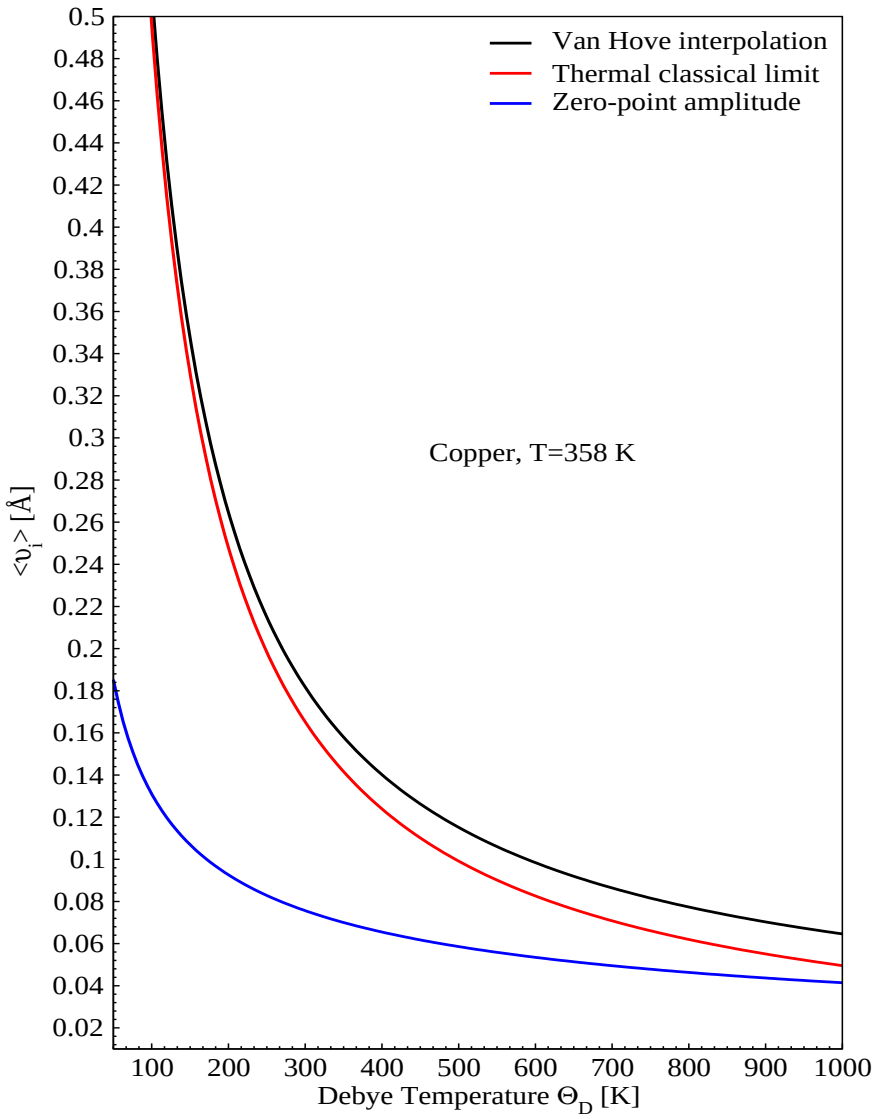

Figure 9.4: RMS displacement of Cu atoms as a function of the Debye temperature

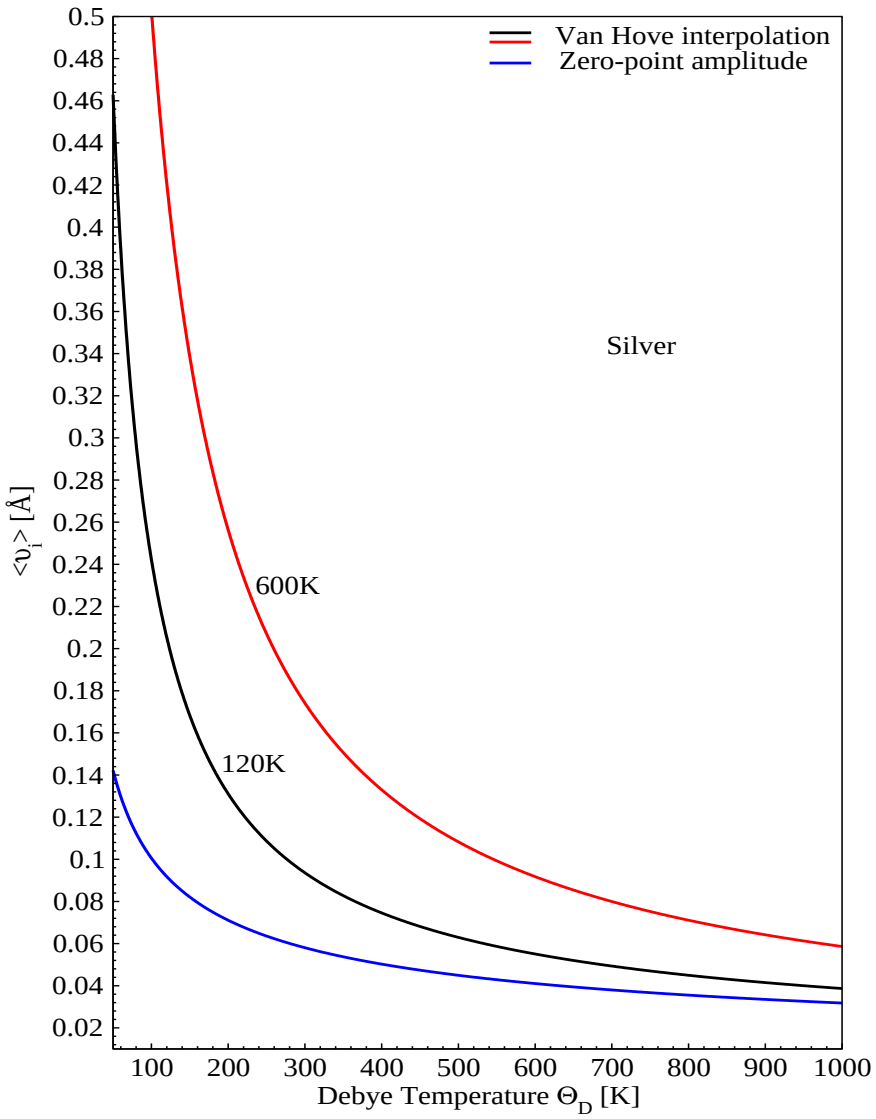

Figure 9.5: RMS displacement of Ag atoms as a function of the Debye temperature

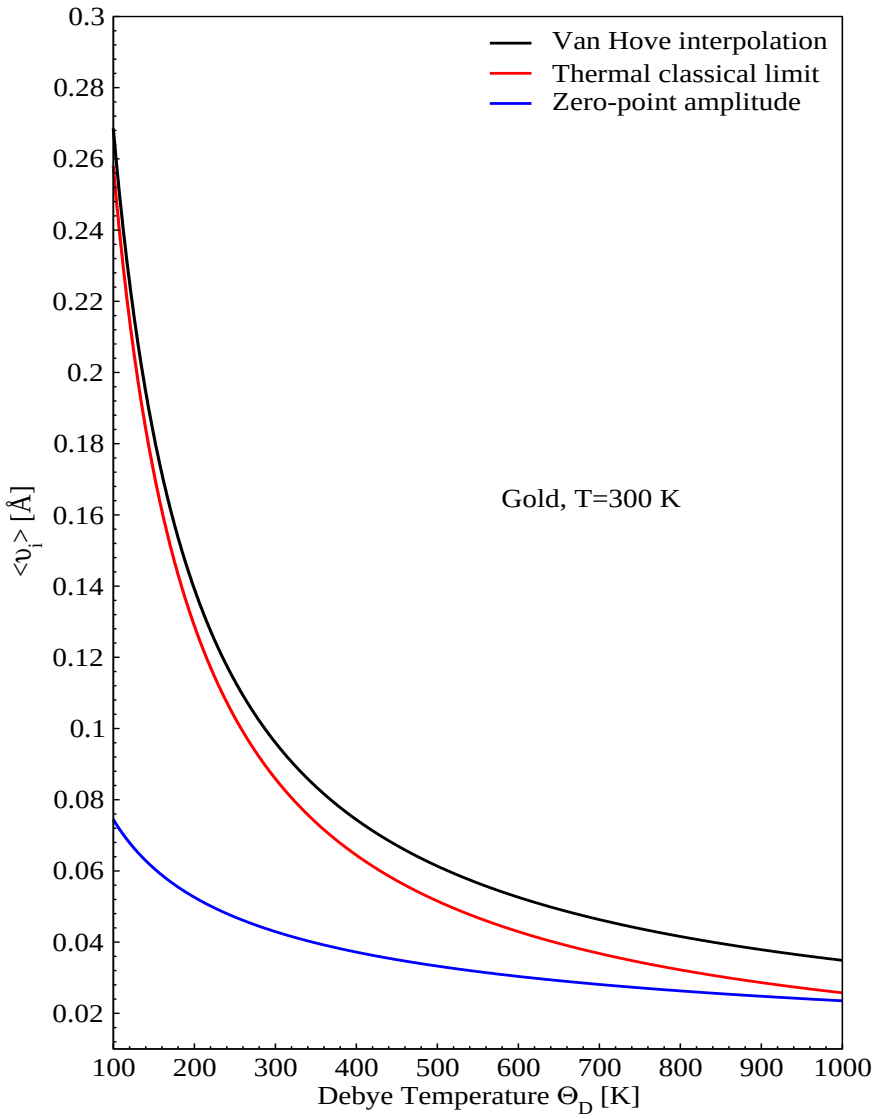

Figure 9.6: RMS displacement of Au atoms as a function of the Debye temperature

Experimental Data

Author	Przyrembel [39]			Pauls [33]		
beam	E_{min}(eV)	E_{max}(eV)	ΔE (eV)	E_{min}(eV)	E_{max}(eV)	ΔE (eV)
(0,1)	50	340	291	50	230	181
(1,0)	50	340	291	50	230	181
(1,1)	50	340	281	50	230	181
(0,2)	50	340	291	50	230	181
(1,2)	90	340	251			
(0,3)	165	340	176			
(2,0)	116	340	225			
(2,1)	140	340	201			
∑ (ΔE)			2007			724

Table 9.1: Experimental energy ranges for the Re(1×1) phase.

Diffraction order (beam)	Minimum energy E_{min}(eV)	Maximum energy E_{max}(eV)	Energy width ΔE (eV)
(0,1)	74	341	268
(1,0)	38	342	305
(1,1)	46	342	297
(0,2)	80	320	241
(1,2)	81	339	259
(0,3)	183	330	148
(2,0)	128	325	198
(2,1)	191	341	151
∑ (ΔE)			1867

Table 9.2: Experimental energy ranges for the Cu(1×1) phase with $\Theta_{Cu} = 2ML$.

Diffraction order (beam)	Minimum energy E_{min}(eV)	Maximum energy E_{max}(eV)	Energy width ΔE (eV)
(0,1)	49	337	289
(1,0)	42	336	295
(1,1)	44	334	291
(0,2)	83	336	254
(1,2)	77	336	260
(0,3)	133	336	204
(2,0)	113	337	225
(2,1)	167	335	169
$\sum$ (ΔE)			1987

Table 9.3: Experimental energy ranges for the Cu(1×1) phase with $\Theta_{Cu} = 3\,ML$.

Diffraction order (beam)	Minimum energy E_{min}(eV)	Maximum energy E_{max}(eV)	Energy width ΔE (eV)
(0,1)	45	341	297
(1,0)	35	340	306
(1,1)	45	340	296
(0,2)	57	342	286
(1,2)	77	340	264
(0,3)	106	342	237
(2,0)	128	342	215
(2,1)	160	340	181
$\sum$ (ΔE)			2082

Table 9.4: Experimental energy ranges for the Cu(1×1) phase with $\Theta_{Cu} = 4\,ML$.

Diffraction order (beam)	Minimum energy E_{min}(eV)	Maximum energy E_{max}(eV)	Energy width ΔE (eV)
(0,1)	52	336	285
(1,0)	44	313	270
(1,1)	45	335	291
(0,2)	81	340	260
(1,2)	83	336	254
(0,3)	111	334	224
(2,0)	147	335	189
(2,1)	197	339	143
$\sum$ (ΔE)			1916

Table 9.5: Experimental energy ranges for the Cu(1×1) phase with $\Theta_{Cu} = 5\,ML$.

Diffraction order (beam)	Minimum energy E_{min}(eV)	Maximum energy E_{max}(eV)	Energy width ΔE (eV)
(0,1)	30	311	282
(1,0)	47	311	265
(1,1)	46	311	266
(0,2)	46	272	227
(0,3)	118	288	171
(2,0)	165	311	147
(2,1)	136	311	176
(3,1)	145	311	167
$\sum$ (ΔE)			1701

Table 9.6: Experimental energy ranges for the Ag(1×1) phase.

Diffraction order (beam)	Minimum energy E_{min}(eV)	Maximum energy E_{max}(eV)	Energy width ΔE (eV)
(0,1)	76	198	123
(1,0)	70	316	247
(1,1)	52	318	267
(0,2)	59	352	294
(1,2)	90	352	267
(0,3)	121	258	138
(2,0)	144	295	152
(2,1)	141	352	212
(0,4)	203	352	150
(0,3/4)	57	158	102
(0,7/4)	47	307	261
(1,3/4)	47	299	253
$\sum$ (ΔE)			2466

Table 9.7: Experimental energy ranges for the Ag(1×4) phase.

Diffraction order (beam)	Minimum energy E_{min}(eV)	Maximum energy E_{max}(eV)	Energy width ΔE (eV)
(0,1)	90	317	228
(1,0)	50	352	303
(1,1)	60	280	221
(0,2)	62	269	208
(1,2)	147	311	165
(2,0)	256	355	100
(0,4)	261	352	92
(1/2,1/2)	33	107	75
(1/2,3/2)	56	243	188
$\sum$ (ΔE)			1580

Table 9.8: Experimental energy ranges for the Ag-c(2×2) phase.

Diffraction order (beam)	Minimum energy E_{min}(eV)	Maximum energy E_{max}(eV)	Energy width ΔE (eV)
(0,1)	32	249	218
(1,0)	32	249	218
(1,1)	43	249	207
(0,2)	50	249	200
(1,2)	91	225	135
(2,0)	136	249	114
(2,1)	141	249	109
(1,3)	156	249	94
(0,4/3)	32	189	158
(0,2/3)	32	94	63
(0,5/3)	36	197	162
(1,2/3)	48	117	70
$\sum$ (ΔE)			1748

Table 9.9: Experimental energy ranges for the Au(1×3) phase.

Diffraction order (beam)	Minimum energy E_{min}(eV)	Maximum energy E_{max}(eV)	Energy width ΔE (eV)
(0,1)	17	100	84
(1,0)	32	100	69
(1,1)	45	100	56
(0,2)	35	100	66
(0,1/4)	17	100	84
(0,3/4)	17	100	84
(0,5/4)	19	52	34
(0,2/4)	17	98	82
$\sum$ (ΔE)			559

Table 9.10: Experimental energy ranges for the Au(1×4) phase.

Diffraction order (beam)	Minimum energy E_{min}(eV)	Maximum energy E_{max}(eV)	Energy width ΔE (eV)
(0,1)	42	340	299
(1,0)	33	342	310
(1,1)	45	342	298
(0,2)	51	342	292
(1,2)	87	342	256
(0,3)	118	342	225
(2,0)	140	342	203
(2,1)	143	342	200
(1,3)	148	342	195
(2,2)	184	342	159
(0,4)	221	342	122
(1,4)	255	342	88
(2,3)	250	342	93
(0,1/2)	21	100	80
(0,3/2)	39	342	304
(1,1/2)	36	342	307
(0,5/2)	78	342	256
(1,5/2)	119	342	224
(2,1/2)	127	342	216
(0,7/2)	187	342	156
(1,7/2)	196	342	147
$\sum$ (ΔE)			4430

Table 9.11: Experimental energy ranges for the CO(1×2) phase.

List of Figures

List of Tables